

Anonymous Referee #2

Received and published: 7 November 2018

Referee #2: This is a seminal work providing in depth analysis of the new algorithms used by AERONET/CIMEL aerosol network.

Author Response: The Authors thank you for spending time in reviewing the manuscript and providing constructive comments to further improve the manuscript.

Referee #2: Here are some comments that hopefully improve the already high standards article.

Referee #2: L68 PHOTONS (PHOTométrie pour le Traitement Opérationnel de Normalisation Satellitaire) and (RIMA) Red Ibérica de medida Fotométrica de Aerosoles.

Author Response: Referee #1 had a similar comment and the changes are listed below.

Author Changes (in bold):

Standardization of Sun photometer instrumentation, calibration, and freely available data dissemination of AOD and related aerosol databases highlights the success of the federated AERONET. For more than 25 years, the AERONET federation has expanded due to the investments and efforts of NASA (Goddard Space Flight Center, GSFC) (Holben et al. 1998), University of Lille (PHOTométrie pour le Traitement Opérationnel de Normalisation Satellitaire (PHOTONS)) (Goloub et al., 2007), University of Valladolid (Red Ibérica de medida Fotométrica de Aerosoles (RIMA)) (Toledano et al., 2011), other subnetworks (e.g., AEROCAN (Bokoye et al., 2001), AeroSpan (Mitchell et al., 2017), AeroSibnet (Sakerin et al., 2005), CARSNET (Che et al., 2015)), and collaborators at agencies, institutes, universities, and individual scientists worldwide.

Referee #2: L134-135 This is true only if $V(\lambda)$ error is independent of air mass. E.g. not true if theoretically signal non linearity errors are involved. Have the instruments been tested for non linearity issues?

Author Response: The statement has been clarified for generalization as this applies to Equation 2.

Author Changes (in bold):

*For the Cimel Sun photometer, the voltage signal is expressed as integer digital counts or digital number (DN). The error in the $\tau(\lambda)_{Total}$ is **generally** dependent on the optical air mass (m) by $\delta\tau$ proportional to m^{-1} and hence the AOD computation error will **tend** be maximum at $m=1$ (Hamonou et al., 1999). **Cimel***

instrument repeatability is tested during calibration procedures by comparing voltage ratios between the field instrument and reference instrument to be less than $\pm 1\%$ (Holben et al., 1998).

Referee #2: L160 what is the impact in AOD due to the pressure uncertainty?

Author Response: The AOD uncertainty due to pressure uncertainty ($\pm 2\text{hPa}$) is expected to be less than 0.002 for the UV and insignificant for visible and near-infrared..

Referee #2: A table summarizing the uncertainty budget that is related to all factors included in section 2 for V2 and V3 pointing out in which aspects the V2 uncertainty has been improved based on the new V3 QA/QC procedures presented here, would give more value to the whole manuscript.

Author Response: Similar answer to Referee #1's question. Eck et al. 1999 stated estimated one sigma uncertainty to be for reference and field instruments. The AOD uncertainty estimates did not change at any significant digits spectrally for Version 3 since it is dominated by calibration uncertainty. The total estimated AOD uncertainty does not change since the Rayleigh optical depth uncertainty for Version 2 and 3 is now considered insignificant with use of station pressure and the inclusion of the NO₂ optical depth uncertainty from 340nm to 500nm.

Referee #2: L59-63 It would be informative to mention other less dense existing surface based networks e.g. SKYNET, GAW-PFR.

Author Response: Thank you. We have included additional citations as suggested.

Author Changes (in bold):

*Ground-based Sun photometry, a passive remote sensing technique, is robust in measuring collimated direct sunlight routinely during the daytime in mainly cloud-free conditions (Shaw 1983; Holben et al., 1998; **Takamura and Nakajima 2004, Smirnov et al., 2009; Kazadzis et al., 2018**). While these surface-based measurements are only point measurements, the federated AERONET provides measurements of columnar AOD and aerosol characteristics over an expansive and diverse geographic area of the Earth's surface at high temporal resolution.*

Referee #2: L173-174 what happens with these (A and B) calculations due to the change of the 935nm filter over time?

Author Response: The filter degradation is monitored for all channels during the calibration process. If a filter is degraded, then it is replaced. As a result, the temporal variation in the change of the 935nm filter is considered insignificant.

Referee #2: L199 & 205 can O3 and NO2 climatology be found somewhere on the AERONET web page?

Author Response: The optical depth associated with the O3 and NO2 for specific wavelengths can be downloaded using the AERONET download tool product option “Aerosol Optical Depth” or “Total Optical Depth” at https://aeronet.gsfc.nasa.gov/cgi-bin/webtool_aod_v3. The file also includes the “climatological” values used for O3 and NO2 in Dobson units. The “Total Optical Depth” file will also contain the spectral optical depths of all components.

Referee #2: L206-214 Interesting results on this aspect can be found in Arola and Koskela, 2004

Author Response: Thank you for bringing the attention to this study. We have included in the text as shown below.

Author Changes (in bold):

*Tropospheric NO2 is highly variable spatially due to various source emissions and stratospheric NO2 concentrations are more stable spatially than the tropospheric NO2 **and can bias the calculation of AOD if neglected (Arola and Koskela 2004; Boersma et al., 2004)**. Therefore, regions with high tropospheric NO2 emission will tend to have greater proclivity for deviating from climatological means. Further, NO2 can vary significantly on the diurnal scale (Boersma et al., 2008).*

Arola, A. and Koskela T.: On the sources of bias in aerosol optical depth retrieval in the UV range, J. Geophys. Res., 109, D08209, <https://doi.org/10.1029/2003JD004375>, 2004.

Referee #2: L245-253 it would be interesting to report a summary of the results found for the temperature dependence on AOD based on the characterization of almost all instruments, as mentioned. Is this temperature dependence more or less similar for all instruments/ Are all instruments characterized for temperature dependence?

Author Response: The temperature coefficient is applied to the digital number before the calculation of the AOD. All calibrated instruments have been temperature characterized. However, the temperature response depends on the sensor head optics including the detector and filters. Some instruments have had some or all filters replaced prior to the temperature characterization activity started in 2007. As a result, those instruments may not have the full characterization for historical data and rely on defaults computed based on the filter manufacturer. Figure 18 shows the average difference in AOD between Version 2 and Version 3 as a function of temperature for all instruments. Clarification in regards to the temperature correction (that is, digital number per degree C rather than AOD per degree C) has been added to the text.

Author Changes (in bold):

*Beginning in 2010, the temperature sensitivity was characterized for almost all wavelengths uniquely for each Cimel instrument. The temperature effect on signal (i.e., **digital number per °C**) is a function of the combined sensitivity of the detector and the filter material itself.*

Referee #2: L310 it has to be explained why this formula is used. Is it purely empirical?

Author Response: The amplifier do not affect the mid–visible wavelengths; however, the amplifier in can cause very large values in the UV. As a result, a conservative threshold of two times the sum of the mid–visible wavelength AOD and the sum of the UV wavelengths is empirically determined to be adequate to identify amplifier issues. The sums are used to prevent removal of aerosol data with large spectral dependence.

Referee #2: L409 I think (whichever is greater) is not correct and is not needed. It is sufficient: less than 3 or less than 10%.

Author Response: If the total number of measurements for the day is 10, we cannot have one measurement remaining based on less than three condition, but this measurement would stay if we keep only less than 10% condition. Alternatively, if we have 100 measurements, we will allow 10 points to remain but not nine. Therefore, “whichever is greater” is needed in this case. We have made the change below to clarify “less than 10%” below.

*Author Changes (in bold): If the number of remaining measurements after all screening steps in Sect. 3.2 are performed is less than three measurements or **less than** 10% of the potential measurements (whichever is greater), then the algorithm will remove the remaining measurements.*

Referee #2: Cloud screening algorithms: A common issue is the AOD rejection from the cloud algorithms for dust related high and with high temporal variability, AOD cases. As accurate and also complete dust aerosol series is extremely important for aerosol radiative forcing global studies; are there any aspects of this new algorithm that are applied in such cases?

*Author Response: As you have noted, cloud screening procedures can inadvertently identify dust as clouds. The revised criteria for the AOD triplet variability (AOD Max minus AOD Min) exceeds 0.01 or 0.015*AOD (whichever is greater) still can potentially limit the number of dust measurements passing the algorithm if strong aerosol inhomogeneity occurs within the one minute triplet. Also, the cloud screening algorithm utilizes a new smoothness approach based on the rate of change of 0.01 apparent AOD in one minute (please see Section 3.1). While the new smoothness approach tends to preserve more data than Version 2, the Version 3 smoothness procedure could be affected by extreme changes in AOD due to anomalous aerosol plumes (e.g., biomass burning or desert dust plumes) where a strong gradient exists.*

Referee #2: Could the authors include an example or an assessment of such cases? (such as the very nice examples they already have for other cases)

Author Response: The AERONET site IER–Cinzana (Mali) (13.28° N, 5.93° W) is already presented in Figure 27. This site located very near the south Saharan Desert boundary and frequently experiences dust events and tropical convection cirrus outflow. Figure 27 shows the Angstrom Exponent is typically between 0.2 and 0.5 indicating predominantly large particles associated with dust aerosols. The algorithm versions can be compared for AOD and Number of Days in panels a and c. In most months, Version 3 has lower AOD and fewer number of days than Version 2 suggesting the possibility of removal of cloud contamination or extreme dust events. Checking some specific periods of high AOD days removed in Version 3 and remaining in Version 2, the Version 3 algorithm properly removed data when cloud contamination was a high likelihood even in the potential presence of dust as on the following dates: 1 June 2010, 7 August 2010, 25 October 2011, and 3 June 2012. Figures 1 and 2 below provide an example of the case on 3 June 2012.

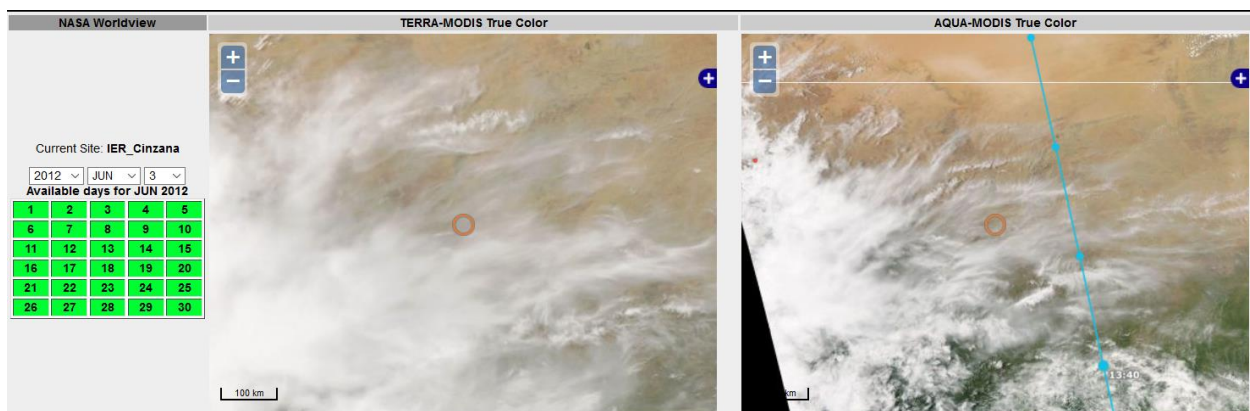


Figure 1 IER-Cinzana affected by cirrus clouds on 3 June 2012. These data were available in Version 2 Level 2.0 but are now removed in Version 3 Level 1.5 by the quality control algorithm. Terra image was collected 10:35 UTC and the Aqua image was collected at 13:40 UTC. The data were provided by NASA Worldview via the AERONET Data Synergy tool (https://aeronet.gsfc.nasa.gov/cgi-bin/bamgomas_interactive)

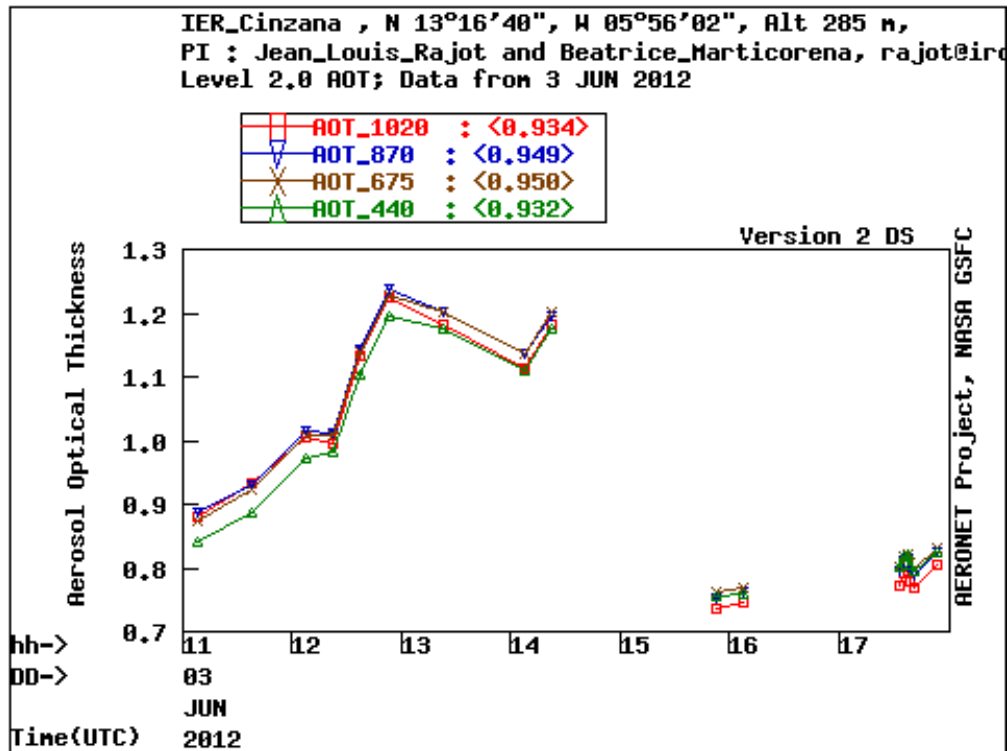


Figure 2 IER-Cinzana site on 3 June 2012 has high optical depth for Version 2 Level 2.0 but these data are affected by optically thin cirrus clouds which are removed by the Version 3 Level 1.5 quality control algorithm.

Referee #2: Very high AOD events could impact the sun-photometer's AOD retrieval based on the diffuse / forward scattered light entering the field of view of the instrument resulting an underestimation of the calculated AOD. Are there any control/corrective measures for such cases?

Author Response: Section 3.1.2 provides explanation in detail the correction procedure regarding light entering the field of view of the instrument.

Referee #2: It is unclear to me why figure 20 cases (in XX') axis differ for the two figures. Aren't we talking about the same data only analyzed for different air masses? If not it can be clarified.

Author Response: Thank you for your comment. Yes, the axis should be the same. The Figure 20 has been modified as shown below.

Author Changes:

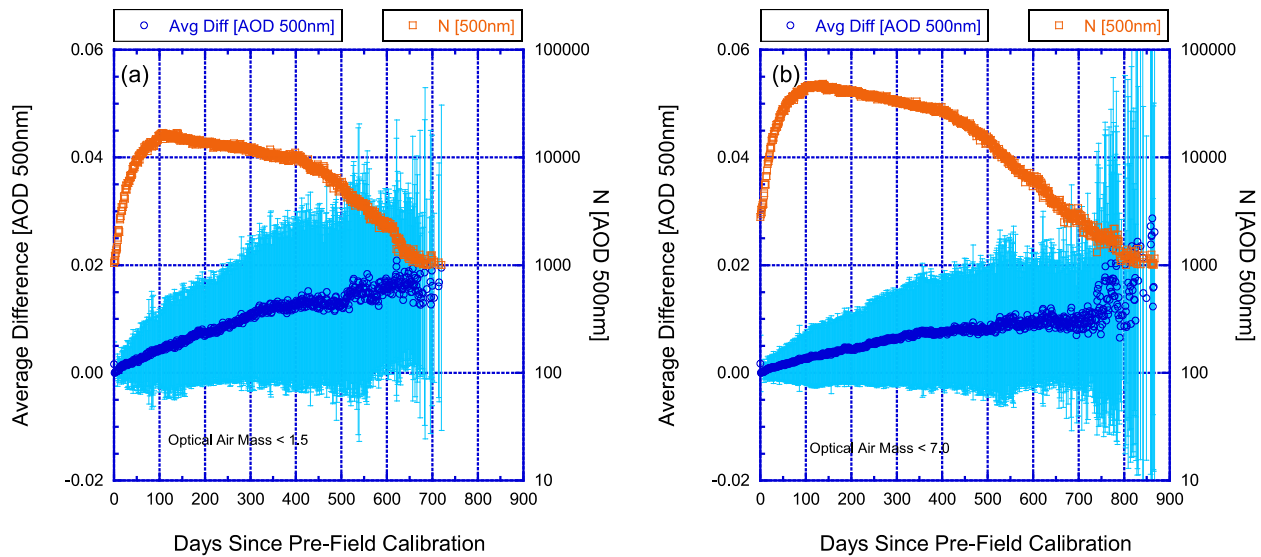


Figure 20. Using data qualified as Version 3 Level 2.0 aerosol optical depth (AOD) 500nm average difference comparing measurements only with the pre-field calibration applied versus instruments with both the pre-field and post-field calibrations applied from 1993–2018. The AOD average differences are provided for the optical air mass $1.0 \leq m < 7.0$ range in panel (a) and $1.0 \leq m < 1.5$ range in panel (b). Vertical bars represent the standard deviation for each day bin. The secondary y-axis in logarithmic scale represents the number of measurements of AOD 500nm for each day bin.

Referee #2: There is a number of publications pointing out small but systematic differences in wv retrievals from AERONET and the ones from other instruments/methods (GPS, microwave radiometers) is V3 results lead to better results for such comparisons?

Author Response: The precipitable water (PW) is currently provided with the AOD product. The uncertainty for PW is expected to be within 10%. The uncertainty in PW does not cause a significant change in the uncertainty of AOD. The extrapolation of AOD to the 935nm channel may be improved in a few circumstances due to improved temperature characterization of the instrument.

Referee #2: From the point of view of the AERONET user. There are a lot of issues presented here that contribute to the better interpretation of case studies, climatologies related with AERONET/AOD data. For such cases (lets say for example an analysis of a high AOD affected area with frequent dust events that is unknown how many of them have been captured and how many of them have been rejected by the cloud algorithm) the AERONET user could have two options:

- a. To cite this paper speculating that part of his/her results could be related with various QA/QC definitions presented here.
- b. To actually use and/or modify accordingly such QA/QC algorithms in order to have more solid conclusions.

Author Response: The Level 1.0 data will have all of the data that may or may not have been rejected at the Level 1.5 stage and these data are readily available from the AERONET web site: <https://aeronet.gsfc.nasa.gov>.

Referee #2: So the question is: will these algorithms be available to the AERONET users?

Author Response: The methods of the algorithm are provided in this paper. Currently, the algorithm code is currently not available for public release; however, AERONET users are encouraged to contact the authors for pertinent modifications to the algorithm to include in future versions or adapting the algorithm for their applications.

Referee #2: Again, this is a very high quality paper and the authors have done a terrific job in terms of analysis, interpretation and presentation of sun-photometric quality control and assurance procedures for AOD and WV retrievals.

1 **Advancements in the Aerosol Robotic Network (AERONET)**
2 **Version 3 Database – Automated Near Real-Time Quality**
3 **Control Algorithm with Improved Cloud Screening for Sun**
4 **Photometer Aerosol Optical Depth (AOD) Measurements**

5 David M. Giles^{1,2}, Alexander Sinyuk^{1,2}, Mikhail **SG**. Sorokin^{1,2}, Joel S. Schafer^{1,2}, Alexander
6 Smirnov^{1,2}, Ilya Slutsker^{1,2}, Thomas F. Eck^{2,3}, Brent N. Holben², Jasper Lewis^{2,4}, James Campbell⁵,
7 Ellsworth J. Welton², Sergey Korkin^{2,3}, and Alexei Lyapustin²

8 ¹Science Systems and Applications Inc. (SSAI), Lanham, MD 20706, USA

9 ²NASA Goddard Space Flight Center (GSFC), Greenbelt, MD 20771, USA

10 ³Universities Space Research Association (USRA), Columbia, MD 21046, USA

11 ⁴Joint Center for Earth Systems Technology, University of Maryland, Baltimore County, Baltimore, MD 21250,
12 USA

13 ⁵Marine Meteorology Division, Naval Research Laboratory (NRL), Monterey, CA 93943, USA

14

15 **Correspondence:** David M. Giles (David.M.Giles@nasa.gov)

16

17 **Abstract.** The Aerosol Robotic Network (AERONET) provides highly accurate, ground-truth measurements of the
18 aerosol optical depth (AOD) using Cimel Electronique Sun/Sky radiometers for more than 25 years. In Version 2
19 (V2) of the AERONET database, the near real-time AOD was semi-automatically quality controlled utilizing mainly
20 cloud screening methodology, while additional AOD data contaminated by clouds or affected by instrument
21 anomalies were removed manually before attaining quality assured status (Level 2.0). The large growth in the
22 number of AERONET sites over the past 25 years resulted in significant burden to manually quality control millions
23 of measurements in a consistent manner. The AERONET Version 3 (V3) algorithm provides fully automatic cloud
24 screening and instrument anomaly quality controls. All of these new algorithm updates apply to near real-time data
25 as well as post-field deployment processed data, and AERONET reprocessed the database in 2018. A full algorithm
26 redevelopment provided the opportunity to improve data inputs and corrections such as unique filter specific
27 temperature characterizations for all visible and near-infrared wavelengths, updated gaseous and water vapor
28 absorption coefficients, and ancillary data sets. The Level 2.0 AOD quality assured data set is now available within
29 a month after post-field calibration, reducing the lag time from up to several months. Near real-time estimated
30 uncertainty is determined using data qualified as V3 Level 2.0 AOD and considering the difference between the
31 AOD computed with the pre-field calibration and AOD computed with pre-field and post-field calibration. This
32 assessment provides a near real-time uncertainty estimate where average differences of AOD suggest a +0.02 bias
33 and one sigma uncertainty of 0.02, spectrally, but the bias and uncertainty can be significantly larger for specific
34 instrument deployments. Long-term monthly averages analyzed for the entire V3 and V2 databases produced
35 average differences (V3-V2) of +0.002 with a ± 0.02 standard deviation, yet monthly averages calculated using
36 time-matched observations in both databases were analyzed to compute an average difference of -0.002 with a
37 ± 0.004 standard deviation. The high statistical agreement in multi-year monthly averaged AOD validates the
38 advanced automatic data quality control algorithms and suggests that migrating research to the V3 database will
39 corroborate most V2 research conclusions and likely lead to more accurate results in some cases.

40 1 Introduction

41 Space-based, airborne, and surface-based Earth observing platforms can remotely retrieve or measure aerosol
42 abundance. Each method has its own assumptions and dependencies in which the aerosol total column abundance
43 quantified by aerosol optical depth (AOD) introduces uncertainty in the retrieval or measurement. At the forefront,
44 ground based Sun photometry has been considered the ground truth in the measurement of AOD given minimal
45 assumptions, reliable calibration, and weak dependency on trace gases at carefully selected wavelength bands thus
46 resulting in highly accurate data (Holben et al., 1998). Meanwhile, AOD inferred from other observing platforms
47 such as satellite retrievals provide quantitative AOD but with significantly higher uncertainty (Remer et al., 2005; Li
48 et al., 2009; Levy et al., 2010; Sayer et al., 2013). Further, in situ measurements lack the ability to provide a reliable
49 columnar AOD due to the requirement of measuring aerosols vertically in each layer while not perturbing or
50 modifying the particle properties during the measurement (Redemann et al., 2003; Andrews et al., 2017). Light
51 Detection and Ranging (LIDAR) is fundamental in the determination of the vertical aerosol extinction distribution
52 (Welton et al., 2000; Omar et al., 2013). Quantification of columnar AOD from ground-based LIDAR, for example,
53 may be less reliable due to low signal to noise ratio during the daylight hours at high altitudes and below the overlap
54 region in which the aerosols very near the surface are poorly observed by LIDAR. Satellite retrieval issues include
55 determining the AOD for very high aerosol loading episodes, cloud adjacency effects, land/water mask depiction,
56 surface reflectance, highly varying topography, and aerosol type assumptions (Levy et al., 2010; Levy et al., 2013;
57 Omar et al., 2013). With each of these measurement platforms, uncertainties exist with AOD; however, these
58 concerns are minimized with AOD measurements from surface based Sun photometry such as from the federated
59 Aerosol Robotic Network (AERONET). Ground-based Sun photometry, a passive remote sensing technique, is
60 robust in measuring collimated direct sunlight routinely during the daytime in mainly cloud-free conditions (Shaw
61 1983; Holben et al., 1998; [Takamura and Nakajima 2004](#), [Smirnov et al., 2009](#); [Kazadzis et al., 2018](#)). While these
62 surface-based measurements are only point measurements, the federated AERONET provides measurements of
63 columnar AOD and aerosol characteristics over an expansive and diverse geographic area of the Earth's surface at
64 high temporal resolution.

65
66 Standardization of Sun photometer instrumentation, calibration, and freely available data dissemination of AOD and
67 related aerosol databases highlights the success of the federated AERONET. For more than 25 years, the
68 AERONET federation has expanded due to the investments and efforts of NASA ([Goddard Space Flight Center](#),
69 [GSFC](#)) ([Holben et al. 1998](#)), University of Lille ([PHOTométrie pour le Traitement Opérationnel de Normalisation](#)
70 [Satellitaire \(PHOTONSPHOTONS\)/ACTRIS](#)) ([Goloub et al., 2007](#)), and University of Valladolid ([Red Ibérica de](#)
71 [medida Fotométrica de Aerosoles \(RIMA\)/ACTRIS](#)) ([Toledano et al., 2011](#)), and other subnetworks (e.g.,
72 [AEROCAN](#)) ([Bokoye et al., 2001](#)), [AeroSpan](#)) ([Mitchell et al., 2017](#)), [AeroSibnet](#)) ([Sakerin et al., 2005](#)), [CARSNET](#)
73 ([Che et al., 2015](#)), and collaborators at agencies, institutes, universities, and individual scientists worldwide.
74 Conceived in the late 1980s, AERONET's primary objective was to provide an aerosol database for validation of
75 Earth Observing System (EOS) satellite retrievals of AOD and atmospheric correction ([Kaufman and Tanré, 1996](#)).
76 In addition to columnar direct Sun AOD, sky radiances were used to infer aerosol characteristics initially from

77 Nakajima et al. (1996) (SkyRad.PAK) and later by the Dubovik and King (2000) inversion algorithm to obtain
78 products such as aerosol volume size distribution, complex index of refraction, single scattering albedo, and phase
79 functions.

80
81 AERONET is a network of autonomously operated Cimel Electronique Sun/sky photometers used to measure Sun
82 collimated direct beam irradiance and directional sky radiance and provide scientific quality column integrated
83 aerosol properties of AOD and aerosol microphysical and radiative properties (Holben et al., 1998;
84 <https://aeronet.gsfc.nasa.gov>). The development and growth of the program relies on imposing standardization of
85 instrumentation, measurement protocols, calibration, data distribution and processing algorithms derived from the
86 best scientific knowledge available. This instrument network design has led to a growth from two instruments in
87 1993 to over 600 in 2018. During that time, improvements were made to the Cimel instruments to provide weather-
88 hardy, robust measurements in a variety of extreme conditions. While the basic optical technology has evolved
89 progressively from analog to digital processing over the past 25 years, the most recent Sun/sky/lunar CE318 Model
90 T instruments provide a number of new capabilities in measurement protocols, integrity, and customizability
91 ([Barreto et al., 2016](#)).

92
93 All of the slightly varying models of the Cimel instruments can have measurement anomalies affecting direct Sun
94 measurements which include measurements in the presence of clouds, various obstructions in the instrument's field
95 of view, or systematic instrumental issues such as electrical connections, high dark currents, and clock shifts to
96 name a few. Some of these issues depend on instrument model and, for more than a decade, these anomalies have
97 been removed semi-automatically utilizing the cloud screening method developed by Smirnov et al. (2000) and
98 further quality controlled by an analyst to remove additional cloud contaminated data and instrument artifacts from
99 the database. Chew et al. (2011) identified up to 0.03 AOD bias at Singapore due to optically thin cirrus clouds for
100 Version 2 Level 2.0 data. Coincidentally, Huang et al. (2011) examined how cirrus clouds could contaminate AOD
101 measurements up to 25% (on average) of the data in April at Phimai, Thailand, in the Version 2 Level 2.0 data set.
102 The number of AERONET sites has increased to more than 600 sites in the network as of 2018 and the labor
103 intensive effort of quality controlling hundreds of thousands of measurements manually had resulted in a significant
104 delay of quality assured data (Level 2.0) in the AERONET Version 2 database.

105
106 With these issues at hand, the cloud screening quality control procedure was reassessed as well as all other aspects
107 of the AERONET processing algorithm including instrument temperature characterization, ancillary data set
108 updates, and further quality control automation. Utilizing these improvements, the Version 3 Level 2.0 quality
109 controlled dataset requires only the pre-field and post-field calibrations to be applied to the data so these data can
110 now be released within a month of the final post-field instrument calibration instead being of delayed up to several
111 months. As encouraged by the AERONET community, automatic quality controls in Version 3 are now also applied
112 to near real-time Level 1.5 AOD products allowing for improved data quality necessary for numerous applications

113 such as numerical weather prediction, atmospheric transport models, satellite evaluation, data synergism, and air
114 quality.

115
116 The AERONET Version 3 processing algorithm marks a significant improvement in the quality controls of the Sun
117 photometer AOD measurements particularly in near real-time. The revised AERONET algorithm is introduced by
118 first reviewing the calculations made to compute the AOD plus changes in the input data sets and the resulting
119 calculation of optical depth components. Next, the preprocessing steps and data prescreening are discussed for the
120 Version 3 quality control algorithm. Cloud screening and instrument quality control algorithm changes are
121 discussed with reference to Smirnov et al. (2000), and the solar aureole cirrus cloud screening quality control is
122 introduced for the first time. The automation of instrument anomaly quality controls and additional cloud screening
123 is described in the subsequent sections. Lastly, the AERONET Version 2 and Version 3 database results are
124 analyzed for the entire data set as well as for selected sites.

125 2 Aerosol Optical Depth Computation

126 Sun photometry is a passive remote sensing measurement technique in which mainly collimated light generally not
127 scattered or absorbed by the atmosphere illuminates a photodiode detector and this light energy is converted to a
128 digital signal. The digital signal (V) measured by the instrument is proportional to the solar irradiance. The relative
129 solar calibration is derived from the Langley method (Ångström 1970; Shaw et al., 1973) utilizing the digital counts
130 from the instrument versus the optical air mass to obtain the calibration coefficient (V_o) by choosing the intercept
131 where optical air mass is zero at the top of the atmosphere (Shaw, 1983). The relative extraterrestrial solar
132 irradiance is proportional to V_o . As shown by Holben et al. (1998) and for completeness in this discussion, the Beer-
133 Lambert-Bouguer law converted to instrument digital counts is shown in Eq. (1)(+):

$$134 \quad V(\lambda) = V_o(\lambda) * d^2 * \exp[-\tau(\lambda)_{Total} * m], \quad (1)$$

135 where $V(\lambda)$ is the measured spectral voltage of the instrument dependent on the wavelength (λ), $V_o(\lambda)$ is the relative
136 extraterrestrial spectral calibration coefficient dependent on λ , d is the ratio of the average to the actual Earth-Sun
137 distance (Michalsky, 1988; USNO, 2018), $\tau(\lambda)_{Total}$ is the total optical depth, and m is the optical air mass, which is
138 strongly dependent on the secant of the solar zenith angle (Kasten and Young, 1989). For the Cimel Sun
139 photometer, the voltage signal is expressed as integer digital counts or digital number (DN). The error in the $\tau(\lambda)_{Total}$
140 is generally dependent on the optical air mass (m) by $\delta\tau$ proportional to m^{-1} and hence the AOD computation error
141 will tend be maximum at $m=1$ (Hamonou et al., 1999). Cimel instrument repeatability is tested during calibration
142 procedures by comparing voltage ratios between the field instrument and reference instrument to be less than $\pm 1\%$
143 (Holben et al., 1998). The absolute uncertainty in the AOD measurement can be described as Eq. (2)(-), with
144 calibration uncertainty of V_o being the overwhelmingly dominant error source:

145

$$\delta\tau = \frac{1}{m} * \left(\frac{\delta V}{V} + \frac{\delta V_o}{V_o} + \tau * \delta m \right) \cong \frac{1}{m} * \frac{\delta V_o}{V_o} \quad (2)$$

146
147 The spectral aerosol optical depth (AOD; $\tau(\lambda)_{Aerosol}$) should be computed from the cloud-free spectral total optical
148 depth ($\tau(\lambda)_{Total}$) and the subtraction of the contributions of Rayleigh scattering optical depth and spectrally dependent
149 atmospheric trace gases as shown in Eq. (3)(3).
150

$$\tau(\lambda)_{Aerosol} = \tau(\lambda)_{Total} - \tau(\lambda)_{Rayleigh} - \tau(\lambda)_{H_2O} - \tau(\lambda)_{O_3} - \tau(\lambda)_{NO_2} - \tau(\lambda)_{CO_2} - \tau(\lambda)_{CH_4} \quad (3)$$

151
152 The Rayleigh optical depth ($\tau_{Rayleigh}$) is calculated based on the assumptions defined in Holben et al. (1998), optical
153 air mass (Kasten and Young 1989), and formula by Bodhaine et al. (1999), except correcting the result based on the
154 NCEP derived station pressure. The ozone (O_3) optical depth (τ_{O_3}) is dependent on the O_3 absorption coefficient
155 (a_{O_3}) for the specific wavelength, the geographic and temporally dependent multi-year monthly climatological Total
156 Ozone Mapping Spectrometer (TOMS) O_3 concentration (C_{O_3}), and the O_3 optical air mass (m_{O_3}) (Komhyr et al.,
157 1989) using the following formulation: $\tau_{O_3} = a_{O_3} * C_{O_3} * m_{O_3}/m$. Similarly, nitrogen dioxide (NO_2) optical depth
158 (τ_{NO_2}) is computed using absorption coefficient (a_{NO_2}) and geographic and temporally dependent multi-year monthly
159 climatological Ozone Monitoring Instrument (OMI) NO_2 concentration (C_{NO_2}) assuming NO_2 scale height is equal to
160 aerosol: $\tau_{NO_2} = a_{NO_2} * C_{NO_2}$. The water vapor optical depth (τ_{H_2O}) is calculated based filter dependent (e.g., 1020nm
161 and 1640nm) A and B coefficients (discussed further below) and precipitable water in cm (u) using the following
162 linear formulation: $\tau_{H_2O} = A + Bu$. The carbon dioxide (CO_2) optical depth (τ_{CO_2}) and methane (τ_{CH_4}) use station
163 elevation dependent formulations: $\tau_{CO_2} = 0.0087 * P/P_0$ and $\tau_{CH_4} = 0.0047 * P/P_0$, assuming the U.S. standard
164 atmosphere (1976) and absorption constants derived from HITRAN. Further descriptions of these calculations are
165 provided below.
166
167

168 Table 1~~Table 4~~ provides a list of the spectral corrections used in the calculation of AOD and precipitable water from
169 935nm. The nominal standard aerosol wavelengths are 340nm, 380nm, 440nm, 500nm, 675nm, 870nm, 1020nm,
170 and 1640nm. For wavelengths shorter than and equal to 1020nm, these channels are measured using a Silicon
171 photodiode detector with a spectral range from 320nm to 1100nm. If the Cimel instrument has an InGaAs detector
172 with a 900nm to 1700nm spectral range, then the 1640nm wavelength is measured along with a redundant 1020nm
173 measurement used to compare instrument optical characteristics between detectors, lenses, and collimator tubes.
174 The Cimel SEAPRISM instrument models, which are deployed on ocean or lake platforms as part of the
175 AERONET-Ocean Color component to retrieve normalized water leaving radiances at 8–12 additional visible band
176 wavelengths for ocean and lake remote sensing studies, are similarly corrected for atmospheric effects (Zibordi et
177 al., 2010).
178

179 Rayleigh optical depth calculations require the use of the station pressure (Bodhaine et al., 1999) as well as the
 180 optical air mass (Kasten and Young 1989). To determine AERONET site station pressure (P_s), the NCEP/NCAR
 181 reanalysis mean sea level pressure and geopotential heights at standard levels (1000hPa, 925hPa, 850hPa, 700hPa,
 182 and 600hPa) are fitted by a quadratic function in logarithmic space to infer the station pressure at the corresponding
 183 interpolated geopotential height. The NCEP/NCAR reanalysis data are available routinely at six hourly temporal
 184 resolution and 2.5 degrees spatial resolution (Kalnay et al., 1996). Errors in the station pressure are generally less
 185 than 2hPa when the station elevation is accurate and the weather conditions are benign (i.e., atmospheric pressure
 186 tends to be stable), since aerosol measurements are typically performed in mainly cloud-free conditions.

187
 188 The 935nm wavelength is used to determine the water vapor optical depth contribution, which is consequently
 189 subtracted from the longer aerosol wavelengths (i.e., 709nm SEAPRISM, 1020nm, and 1640nm). The AOD at
 190 935nm is extrapolated based on the Ångstrom exponent (AE) computed from the linear regression of the AOD and
 191 wavelengths in logarithmic space within the range of 440–870nm excluding channels affected by water vapor
 192 absorption (Eck et al., 1999). To extract the precipitable water (PW) in cm from the 935nm measurements, the
 193 Rayleigh optical depth and the AOD components need to be subtracted from the total optical depth at 935nm. As a
 194 result, the dimensionless column water vapor abundance (u) is obtained using the following equations:

$$T_W = \ln[T_{935nm[Measured]}] - \ln[T_{935nm[Extrapolated]}] \quad (4)$$

$$-\ln[T_W] = \ln[V_{o\ 935nm} * d^{-2}] - \ln[V_{935nm}] - m * (\tau_{935nm\ AOD} + \tau_{935nm\ Rayleigh}) \quad (5)$$

$$\ln\left[\frac{T_W}{C}\right] = -A * (m_W * u)^B \quad (6)$$

$$u = \frac{\left[\frac{\ln T_W}{-A}\right]^{1/B}}{m_W} \quad (7)$$

196
 197 where T_W is the water vapor transmission and constants A and B are absorption constants unique to the particular
 198 935nm filter, C is an absorption constant assumed to be equal to one (Ingold et al., 2000), d and m are defined in Eq.
 199 (1), m_W is the water vapor optical air mass (Kasten et al., 1965), and u is the total column water vapor abundance
 200 (Schmid et al., 2001; Smirnov et al., 2004). The total column water vapor abundance (u) is converted to total
 201 column water content or PW by using the normalization factor ($u_o=10\text{ kg/m}^2$) and dividing it by the mean value of
 202 water density ($\rho_o=1000\text{ kg/m}^3$) to obtain water column height units of cm (Bruegge et al., 1992; Ingold et al., 2000).

203
 204 In the calculation of the filter dependent A and B constants, the water vapor absorption optical thickness is
 205 determined by the integration of water vapor extinction coefficient over height from the bottom to the top of the
 206 atmosphere. This calculation requires the following inputs to determine the extinction at each height: HITRAN

207 spectral lines with assumed US1976 model standard atmosphere temperature and pressure profiles; the absorption
 208 continuum look-up table from the Atmospheric and Environmental Research (AER) Radiative Transfer Working
 209 Group (Clough et al., 1989; Mlawer et al., 2012); and Total Internal Partition Sums that define the shape and
 210 position of lines dependent on temperature (Gamache et al., 2017). Nine defined total column water vapor amounts
 211 (0.5 cm, 1.0 cm, 1.5 cm, 2.0 cm, 2.5 cm, 3.0 cm, 4.0 cm, 5.0 cm, and 6.5 cm) are used to generate water vapor
 212 absorption optical depth lookup tables. From these lookup tables, transmittances are calculated based on the
 213 bandpass and averaged spectral solar irradiance for the quiet Sun obtained from the University of Colorado
 214 LASP/NRL2 model (Coddington et al., 2016) to generate filter-specific A and B coefficients. The one sigma
 215 uncertainty in the calculation of PW in cm is expected to be less than 10% compared to GPS precipitable water
 216 retrievals (Halthore et al., 1997; Bokoye et al., 2003; Sapucci et al., 2007; Alexandrov et al., 2009; Prasad et al.
 217 2009; Bock et al., 2013; Van Malderen et al., 2014; Pérez-Ramírez et al., 2014; Campenelli et al., 2018). The
 218 spectral water vapor optical thickness ($\tau_{H_2O}(\lambda)$) is determined by computing the average of all A and B constants
 219 from the suite of filters affected by water vapor absorption (i.e., 709nm SEAPRISM, 935nm, 1020nm, and 1640nm)
 220 in the AERONET database. The $\tau_{H_2O}(\lambda)$ is also dependent on the dimensionless total column water vapor abundance
 221 (Michalsky et al., 1995; Schmid et al., 1996):

$$\tau_{H_2O}(\lambda) = \bar{A}(\lambda) + \bar{B}(\lambda) * u \quad (8)$$

223
 224 The contribution of ozone (O_3) optical depth is determined utilizing the total column ~~Total Ozone Mapping~~
 225 ~~Spectrometer (TOMS)~~TOMS monthly average climatology (1978–2004) of O_3 concentration at $1.00^\circ \times 1.25^\circ$ spatial
 226 resolution, the O_3 optical air mass using O_3 scale height adjustment by latitude (Komhyr et al., 1989), and the O_3
 227 absorption coefficient (Burrows et al., 1999). The OMI O_3 data set is not used here due to instrument sampling
 228 anomalies (McPeters et al., 2015). While the TOMS O_3 data set is extensive and generally characterizes the
 229 distribution of O_3 , recent changes in concentration could introduce some minor uncertainty in AOD. Similarly, the
 230 nitrogen dioxide (NO_2) optical depth is calculated using the total column OMI monthly average climatology (2004–
 231 2013) of NO_2 concentration at $0.25^\circ \times 0.25^\circ$ spatial resolution and the NO_2 absorption coefficient (Burrows et al.,
 232 1998). Tropospheric NO_2 is highly variable spatially due to various source emissions and stratospheric NO_2
 233 concentrations are more stable spatially than the tropospheric NO_2 ~~and can bias the calculation of AOD if neglected~~
 234 (Arola and Koskela 2004; Boersma et al., 2004). Therefore, regions with high tropospheric NO_2 emission will tend
 235 to have greater proclivity for deviating from climatological means. Further, NO_2 can vary significantly on the
 236 diurnal scale (Boersma et al., 2008). Improved satellite observations, models, or collocation with surface-based
 237 PANDORA instruments measuring temporal total column O_3 and NO_2 may assist in reducing the uncertainty and
 238 determination of the total column NO_2 optical depth contribution in later versions of the algorithm (Herman et al.,
 239 2009; Tzortziou et al. 2012). Concentrations for carbon dioxide (CO_2) and methane (CH_4) are assumed constant and
 240 optical depths are computed based on the HITRAN-derived absorption coefficients of 0.0087 and 0.0047 for the
 241 1640nm filter, respectively, and adjusted to the station elevation.

243 The calibration of the AOD measurements is traced to a Langley measurement performed by a reference instrument
244 ([Shaw 1983; Holben et al., 1998](#)). The reference instruments obtain a calibration based on the Langley method
245 morning only analyses based on typically 4 to 20 days of data performed at a mountaintop calibration sites. The
246 primary mountaintop calibration sites in AERONET are located at Mauna Loa Observatory (19.536° N, 155.576°
247 W, 3402 m) on the island of Hawaii and Izana Observatory (28.309° N, 16.499° W, 2401 m) on the island of
248 Tenerife in the Canary Islands (Toledano et al., 2018). These reference instruments are routinely monitored for
249 stability and typically recalibrated every three to eight months. Reference instruments rotate between mountaintop
250 calibration sites and inter-calibration facilities at NASA GSFC (38.993° N, 76.839° W, 87 m) in Maryland,
251 Carpentras (44.083° N, 5.058° E, 107 m) in France, and Valladolid (41.664° N, 4.706° W, 705 m) in Spain, where
252 reference instruments operate simultaneously with field instruments to obtain pre-field and post-field deployment
253 calibrations. For periods when the AOD is low ($\tau_{440nm} < 0.2$), optical air mass is low ($m < 2$), and aerosol loading is
254 stable, the reference Cimel calibration may be transferred to field instruments (Holben et al., 1998). [Eck et al. 1999](#)
255 [estimates the reference instrument calibration uncertainty impact on AOD varies from 0.0025 to 0.0055 with the](#)
256 [maximum representing uncertainty only in the UV channels \(340nm and 380nm\). In Version 3, the field instrument](#)
257 [AOD uncertainty is still estimated to be from 0.01 to 0.02 with the maximum representing the uncertainty only in](#)
258 [the UV channels \(340nm and 380nm\).](#)

259
260 The Version 2 processing used default temperature corrections based on three sensor head temperature (T_S) ranges
261 ($T_S < 21^\circ\text{C}$, $21^\circ\text{C} \leq T_S \leq 32^\circ\text{C}$, and $T_S > 32^\circ\text{C}$) using a constant nominal temperature sensitivity only for the 1020nm filter
262 direct Sun measurements. In Version 3, measurement temperature sensitivity has been updated for all wavelengths
263 $\geq 400\text{nm}$ and all measurement types (i.e., direct solar, sky, water, and lunar viewing measurements). Beginning in
264 2010, the temperature sensitivity was characterized for almost all wavelengths uniquely for each Cimel instrument.

265 The temperature effect on signal (i.e., digital number per $^\circ\text{C}$) is a function of the combined sensitivity of the detector
266 and the filter material itself. If any Cimel data relying on a filter was in use prior to 2010 and the filter was not
267 temperature characterized, then the default values for the filter and manufacturer type are applied, if established.
268 Filters in the ultraviolet (i.e., 340nm and 380nm) are not measured for temperature dependence because of low
269 integrating sphere radiance output at these wavelengths. Due to temperature dependence of the field instrument and
270 the reference instrument, the Sun and sky calibration transfer needs to be adjusted by computing the ratio of the
271 Cimel temperature coefficients for each wavelength and for the temperature observed at the time of the calibration.
272 In addition, when the AOD is computed for field instruments, the sensor head temperature is measured for each
273 direct Sun measurement so these data can be adjusted to the temperature response of the instrument optics (i.e.,
274 combined effect of the detector and filters) and electronics.

275
276 The temperature response is measured at the AERONET calibration facilities using an integrating sphere and a
277 temperature chamber where the temperature is varied from -40°C to $+50^\circ\text{C}$. The wavelength dependent
278 temperature coefficient is typically determined from the slope of ordinary least squares regression fit of the digital
279 voltage counts versus the sensor head temperature reading. For this relationship, the second order polynomial fit is

280 computed for 1020nm, while other filters use either a linear or second order polynomial fit (depending on the larger
281 correlation coefficient). For Cimel Model 4 and some Model 5 instruments with two Silicon photodiode detectors,
282 the digital counts for solar aureole and sky instrument gains are used to determine temperature coefficients for each
283 detector (Holben et al., 1998; <https://aeronet.gsfc.nasa.gov>). Some Model 5 and all Model T instruments perform
284 the direct Sun and sky measurements on the same detector (Silicon or InGaAs) and typically utilize the solar aureole
285 gain digital counts (Barreto et al., 2016; <https://aeronet.gsfc.nasa.gov>).

286
287 According to Holben et al. (1998), all instruments generally perform measurements sequentially from longer
288 wavelength to the shortest wavelength filters on a rotating filter wheel inside the sensor head, which positions each
289 filter in front of the photodiode detector and behind the sensor head lenses and collimator tube. The robotically
290 controlled sensor head points automatically at the Sun based on the time and geolocation of the instrument. The
291 laboratory tuned 4-quadrant detector provides nearly perfect solar and lunar tracking to one motor step or $\sim 0.1^\circ$
292 immediately following the geographic pointing. A dual tube external collimator with internal baffles attached to the
293 top of the sensor head reduces stray light effects into the sensor head 1.2° field of view optical train.

294
295 The instrument performs measurements of the Sun using measurement triplets, that is, performing the series of
296 measurements of all filters at time hh:m0:00 (time notation for hours, minutes, seconds), where for duration of about
297 eight seconds, and then repeating these measurements at hh:m0:30 and hh:m1:00. The resulting one-minute
298 averaged measurement sequence is defined as a triplet measurement and the maximum to minimum range of these
299 measurements is termed the triplet variability. The triplet measurement advantageously allows for separation of
300 homogeneously dispersed aerosols versus highly temporally variable clouds. The triplet measurements are
301 performed either every 15 minutes for older Model 4 instruments or every three minutes for newer Model 5 and
302 Model T instruments increasing the temporal availability of the AOD measurements in the AERONET database.

303 **3 Automatic Quality Controls of Sun Photometrically Measured Aerosol Optical Depth**

304 The AERONET database has provided three distinct levels for data quality: Level 1.0, Level 1.5, and Level 2.0. In
305 Version 2, Level 1.0 was defined as prescreened data, Level 1.5 represented near real-time automatically cloud-
306 cleared data, and Level 2.0 signified automatically cloud-cleared, manually quality controlled data set with pre and
307 post-field calibrations applied. In Version 3, the definitions have been modified substantially for Level 1.5 and
308 Level 2.0. Version 3 Level 1.5 now represents near real-time automatic cloud screening and automatic instrument
309 anomaly quality controls and Level 2.0 additionally applies pre-field and post-field calibrations. The Version 3 fully
310 automated cloud screening and quality control checks eliminate the need for manual quality control and cloud
311 screening by an analyst and increases the timeliness of quality assured data. Note that in all cases each subsequent
312 data quality level requires the previous data level to be available as input (e.g., Level 1.5 requires Level 1.0 and
313 Level 2.0 requires Level 1.5). The following sections will describe these new definitions and automatic quality
314 controls in detail and the impact these new quality assurance measures have on the AERONET database.

315

316 **3.1 Preprocessing Steps and Prescreening**

317 Most preprocessing data quality criteria operate on voltage (V, expressed as the integer digital number (DN)) or
318 sensor head temperature (T_s). The impact of these conditions may immediately remove data from Level 1.0
319 consideration or later only impact Level 1.5 and Level 2.0 AOD. Each quality control section describes the
320 reasoning for the screening at the specified data quality level. Digital count anomalies typically result from
321 anomalous electronic issues such as very low or high battery voltages, malfunctioning amplifiers, or loose
322 connections of internal control box components. These digital count anomalies mostly affect older ~~instruments~~
323 ~~(Cimel Models 4 (CE318-1) and Model 5 (CE318N)) instruments (Holben et al., 1998;~~
324 ~~<https://aeronet.gsfc.nasa.gov>), while several of these connection issues have been mitigated in the newest~~
325 ~~instruments (Cimel Model T (CE318-T)) instruments (Barreto et al., 2016).~~

326 **3.1.1 Electronic Instability**

327 Cimel Model 4 instruments use a 16-bit analog/digital (A/D) converter in the processing unit in which the analog
328 signal from the sensor head detector to the control box is subject to electronic noise. Cimel Model 5 instruments use
329 a 16-bit A/D converter inside the sensor head and the instrument invokes electronic chopping to reduce electronic
330 noise. Cimel Model T instruments utilize an increased quantization from 16 bits to 24 bits, which significantly
331 reduces noise effects. Cimel Model 5 and Model T instruments internally adjust for the dark current (V_D) with each
332 measurement and no separate record is logged. Cimel Model 4 instruments perform V_D measurements after each
333 sky scan (approximately hourly) for each spectrally dependent instrument gain parameter (i.e., Sun, aureole, and
334 sky). Large V_D values generally represent significant instrument electronic instability. Quality controls applied to the
335 V_D will remove the entire day for Model 4 instrument data from all of the quality levels for either of the following
336 conditions: 1) a single dark current measurement is greater than 100 counts for greater than N-1 wavelengths, where
337 N is the total number of wavelengths or 2) more than three dark current measurements are greater than 100 counts
338 for three or more wavelengths.

339
340 Amplifiers in the Cimel Model 4 instruments can produce unphysical increases in the digital counts or decreases in
341 the AOD for the 340nm and 380nm wavelengths at large optical air mass (Fig. 14). These instability issues are
342 evaluated simply using a relative threshold with respect to the available visible wavelength AOD measurements. If
343 the τ_{380} is greater than $0.5 * \tau_{340}$ and $(\tau_{440} + \tau_{500 \text{ or } 675} < \tau_{380} + \tau_{340} - 2.0)$, then the triplet measurements for 340nm and
344 380nm are removed from the database for Level 1.5 and subsequent levels. These quality controls are limited to
345 Model 4 instruments that were not manufactured after 2001; however, the early AERONET database (1993–2005)
346 contains much of these data. New Cimel Model T instruments are replacing Model 4 instruments but over 40 Model
347 4 instruments remain active in 2018.

348
349 The instrument may rarely malfunction by producing constant digital voltages for triplet measurements and the
350 result of keeping these data in the database leads to unphysical variations in the AOD. A frequency analysis is
351 performed to determine if any digital number (DN) values occur more than 10 times in a day. If more than 50% of

Formatted: Font:

352 the DNs are from the same triplet measurement, then this measurement is identified as an anomalous measurement.
353 If more than 50% of the triplet measurements in the day are considered anomalous, then the entire day will be
354 removed from Levels 1.5 and 2.0.

355 3.1.2 Radiometer Sensitivity Evaluation

356 The Cimel 4-quadrant solar near infrared detector requires enough sensitivity to track the Sun and a DN threshold of
357 100 in the near infrared is needed to have sufficient signal. Near infrared wavelengths (e.g., 1020nm) typically have
358 a higher measured solar DN(V) due to higher atmospheric transmission in the presence of fine mode dominated
359 aerosols even in very high aerosol loading conditions. When the DN ($V_{870\text{nm}}$ or $V_{1020\text{nm}}$) is less than 100 counts for
360 any measurement of the solar triplet, then the entire solar triplet AOD will be removed for all wavelengths from
361 Level 1.0 and subsequent levels due to potential solar tracking accuracy issues.

362
363 Version 2 data processing assessed the instrument electronic and diffuse light sensitivity by defining a digital
364 number (DN) of 10 to remove solar AOD triplet measurements. Electronic issues impact Cimel Model 4
365 instruments in the UV and short visible wavelengths due to high DN(V_D). Scattered diffuse light into the collimated
366 field of view can affect all instruments and produce unusual AOD changes with optical air mass especially when the
367 aerosol loading is high and optical air mass is large. The signal to noise ratio of the Cimel instrument requires setting
368 a minimum threshold for the determination of the solar measured DN(V) to limit the effect of diffuse radiance in the
369 instrument field of view (Sinyuk et al., 2012). When a dark current DN(V_D) (e.g., ~50–100) is nearly equal to or
370 larger than the measured solar DN(V) (e.g., ~25–50) will result in V and τ decreasing with increasing optical air
371 mass. All wavelengths are evaluated to determine if the measured solar DN(V) (subtracted from the closest
372 temporal dark current DN(V_D) for Model 4 instruments only) is less than $\text{DN}(V_O)/1500$, then the identified
373 wavelength will be removed from all AOD levels. A threshold of 1500 is calculated from a DN of 15000, a typical
374 average DN(V_O) for Cimel Models 4 and 5, normalized to a minimum signal DN of 10. The maximum product of
375 AOD times optical air mass ($\tau_m = \tau * m$) of approximately 7.3 is computed by the natural logarithm of 1500 (i.e., \ln
376 (15000/10)) for Cimel Model T instruments. For non-Model T instruments, the 100 DN threshold for 870nm and
377 1020nm limits the τ_m to approximately 5.0 (i.e., \ln (15000/100)) for only those two wavelengths. The τ_m maximum
378 threshold applies to all channels; however, the signal count can decrease significantly with optical air mass and
379 depend on the wavelength dependence of V_O . For values exceeding the τ_m maximum threshold, the diffuse radiation
380 increases the signal and, as a result, unfiltered AODs show a decrease in magnitude as optical air mass increases for
381 high AOD even when DN(V_D) equals zero. A measured solar DN(V) lower than the ratio $\text{DN}(V_O)/1500$ threshold
382 will result in the removal of the solar triplet AOD for the specific wavelength (Fig. 22).

383 3.1.3 Digital ~~Voltage-Number~~ Triplet Variance

384 As mentioned in Sect. 2, the Cimel instrument performs a direct Sun triplet measurement at regular intervals
385 throughout the day. A variance threshold is applied based on the root mean square (RMS) differences of the triplet
386 measurements relative to the mean of these three values. If the $(\text{RMS}/\text{mean}) * 100\%$ of the digital number triplet

Formatted: Font:

387 values is greater than 16%, then these data are not qualified as Level 1.0 AOD (Eck et al., 2014). The digital
388 number temporal variance threshold is sensitive to clouds with large spatial-temporal variance in cloud optical depth
389 and optically thick clouds such as cumulus clouds as well as issues due to poor tracking of the instrument.

390 3.1.4 Sensor Head Temperature Anomaly Identification

391 Each Cimel instrument has a fixed resistance (Model 4) or band gap (Models 5 and T) temperature sensor inside the
392 optical head within 0.5 cm of the detector, filter wheel, and optical train assembly. As discussed in Sect. 2, the
393 instrument optics and digital counts can have dependence to the sensor head temperature (T_S) which is saved with
394 each measurement triplet. Sensor head temperatures may be erroneous due to instrument electronic instability or
395 communication issues. These potentially unphysical values of T_S are evaluated by a number of algorithm steps such
396 as checks for 1) constant T_S values, 32) unphysical extreme high or low T_S , 43) potentially physical yet anomalously
397 low T_S with respect to the NCEP/NCAR reanalysis ambient temperatures, and 54) unphysical T_S decreases (dips) or
398 increases (dipsspikes). When the algorithm removes a T_S reading or the T_S measurement is missing, an assessment
399 is made on the instrument temperature response based on $\pm 15^\circ\text{C}$ of the NCEP/NCAR reanalysis temperature for the
400 date and location to determine whether the temperature characterization coefficient for a specific wavelength would
401 result in a change of AOD by more than 0.02. If this condition is met for a specific wavelength, then data associated
402 with this wavelength-specific triplet measurement will be removed at Level 1.5 and subsequent levels while
403 preserving other less temperature dependent spectral triplet measurements.

404 3.1.5 Eclipse Circumstance Screening

405 During episodic solar or lunar eclipses, AOD will increase to the maximum obscuration of the eclipse at a particular
406 location on the Earth's surface. The AOD increases due to the reduction of the irradiance due to and the celestial
407 body (Moon or Earth) obscuring the calibrated light source (Sun or Moon). While any one point on Earth
408 infrequently experiences an eclipse, when an eclipse episode does occur, the eclipse can affect many locations
409 nearly simultaneously making manual removal tedious at sites distributed globally. To automate the removal of
410 eclipse episodes, the NASA solar and lunar eclipse databases are queried for eclipse circumstances based on
411 geographic position of the site to produce a table of eclipse episodes starting from 1992. The eclipse tool utilizes
412 established Besselian elements based on the Five Millennium Canon of Solar Eclipses: -1999 to +3000 (Espenak
413 and Meeus 2006) to quantify the geometric and temporal position of the celestial bodies (Sun, Earth, and Moon),
414 determine the type of eclipse (e.g., partial, annular, total), and predict times of the various stages of the solar or lunar
415 eclipse. For the Version 3 database, the eclipse site-specific tables are used to discretely remove triplet
416 measurements affected by any stage of the eclipse circumstance. For example, during a solar eclipse, solar triplets
417 will be removed between the partial eclipse first contact to the partial eclipse last contact regardless of the eclipse
418 obscuration or magnitude for Level 1.5 data and subsequent levels (Fig. 33). The partial eclipse first contact is
419 defined as the time at which the penumbral shadow is visible at a point on the Earth's surface and the partial eclipse
420 last contact is defined as the time at which the penumbral shadow is no longer visible a point on the Earth's surface.
421 Efforts to retain AOD during solar eclipse episodes have been attempted by the authors in which up to 95% of the

Formatted: Font:

422 AOD can be corrected based on adjusting calibration coefficients by the eclipse obscuration. However, spectral
423 calibration coefficients also need to be adjusted to account for the solar atmosphere spectral irradiance, which
424 becomes more dominant during the solar eclipse episode and is a topic of further investigation.

425 **3.1.6 Very High AOD Retention**

426 Cloud screening procedures in the next section may inadvertently remove aerosol in very high aerosol loading cases
427 due to biomass burning smoke and urban pollution as discussed by Smirnov et al. (2000). For Version 3, each triplet
428 reaching Level 1.0 is evaluated for possible retention in the event that a specific Level 1.5 cloud screening procedure
429 removes the triplet. When the AOD measurement for 870nm is >0.5 and AOD 1020nm >0.0 , these conditions will
430 potentially qualify the triplet for very high AOD retention. Further analysis is performed on those qualified triplets
431 to remove the effect of heavily cloud-contaminated data using the AE for the wavelength ranges of 675–1020nm or
432 870–1020nm (Eck et al., 1999). If the $AE_{675-1020nm} > 1.2$ (or $AE_{870-1020nm} > 1.3$, if AOD_{675nm} is not available), and the
433 AE for the same range is less than 3.0, then the triplet qualifies for very high AOD retention and the triplet can be
434 retained at Level 1.5 even if the measurement does not pass Level 1.5 cloud screening quality control steps in Sect.
435 3.2.

436 **3.1.7 Total Potential Daily Measurements**

437 Cloud screening methods in Sect. 3.2 may incompletely remove all cloud-contaminated points and leave data
438 fragments. To mitigate this issue, a methodology was developed based on the total number of potential
439 measurements in the day and calculated AE values. The total number of potential measurements in the day is
440 defined as the number of triplet measurements plus the number of ~~humidity status reports (i.e., wet sensor~~
441 ~~activations)~~. If the number of remaining measurements after all screening steps in Sect. 3.2 are performed is less
442 than three measurements or ~~less than~~ 10% of the potential measurements (whichever is greater), then the algorithm
443 will remove the remaining measurements. This condition is repeated after each cloud screening step in Sect. 3.2 and
444 will only be activated when the very high AOD restoration is not triggered (see Sect. 3.1.6) or when the $AE_{440-870nm}$
445 is less than 1.0 for a triplet measurement indicating large particles such as clouds may contaminate the remaining
446 measurements.

447 **3.1.8 Optical Air Mass Range**

448 The basic Cimel Sun photometer Sun and sky measurement protocols were specified to NASA requirements in
449 ~~Hoblen-Holben~~ et al. (1992, 1998, and 2006), and have only been slightly modified since that time for improved
450 measurement capability of the Model 5 and Model T instruments (Barreto et al., 2016). All instruments
451 systematically perform direct Sun measurements between the optical air mass (m) of 7.0 in the morning and m of 7.0
452 in the evening. In Version 2 and earlier databases, AERONET data processing limited the Level 1.5 and Level 2.0
453 AOD computation from m of 5.0 in the morning to m of 5.0 in the evening. The m limitation may avoid potential
454 error in the computation of the optical air mass at large solar zenith angles (Russell et al., 1993) and possible
455 increased cloud contamination (Smirnov et al., 2000). For Version 2 and 3 processing, the Kasten and Young 1989

456 formulation was used to account for very small differences in the optical air mass calculations at high solar zenith
 457 angles. Noting that the AOD error ($\delta\tau/m$) has a minimum at large m (conversely a maximum at solar noon), the
 458 maximum m of 5.0 was extended to m of 7.0 in Version 3 processing. The larger optical air mass range leads to an
 459 increase in the number of solar measurements occurring in the early morning and the early evening contributing to
 460 additional AOD measurements used for input for almucantar and hybrid inversions plus an increase in AOD
 461 measurements at high latitude sites when solar zenith angles may be large even at solar noon. The impact on the
 462 cloud screening performance appears to be minimal for measurements closer to the horizon. The fidelity of the
 463 Version 3 cloud screening (see Sect. 3.2) AODs supports the extended optical air mass range for Level 2.0.

464 3.2 Level 1.5 AOD Cloud Screening Quality Controls

465 As discussed in Sect. 3.1, several preprocessed criteria and parameters are necessary to quality control the AOD data
 466 quality in near real-time (NRT). Cloud screening procedures proposed by Smirnov et al. (2000) were designated to
 467 remove or reduce cloud contaminated AOD measurements. However, these procedures also had the effect of
 468 surreptitiously removing occasionally other non-cloud anomalies such as repeated AOD diurnal dependence when
 469 AOD had a large maximum at midday and minimum at high optical air masses due to environmental impacts on the
 470 optical characteristics of the instrument (e.g., moisture on the sensor head lens or spider webs in the collimator
 471 tube). While these cloud screening methods have been implemented for about 25 years, the state of knowledge has
 472 progressed over this period and thus necessitates review and modification of cloud screening quality control
 473 procedures (Kaufman et al. 2005, Chew et al., 2011; Huang et al., 2011). The calculation of the AOD at Level 1.0
 474 essentially represents the following in Eq. (9)(9):

$$475 \tau_{app\ Total} = \frac{1}{\Gamma_{anomaly}} \left(\tau_{aerosol} + \frac{\tau_{cirrus}}{C_{cirrus}} + \tau_{liquid\ cloud} + \tau_{eclipse} \right) \quad (9)$$

476 where $\tau_{app\ Total}$ is the apparent total optical depth, which at this point in the data processing, may be affected by the
 477 contributions of liquid cloud droplets ($\tau_{liquid\ cloud}$), cirrus amplification factor (C_{cirrus}) applied to the cirrus crystal
 478 optical depth (τ_{cirrus}) due to strong forward scattering into the field of view of the instrument, solar or lunar eclipses
 479 ($\tau_{eclipse}$), and instrument anomalies ($\Gamma_{anomaly}$ adjustment factor). Given cloud free conditions and perfect instrument
 480 operation, the additional non-aerosol τ components would be zero and C_{cirrus} and $\Gamma_{anomaly}$ would be one. However,
 481 the Cimel Sun photometer always attempts to measure the Sun if it can be tracked regardless of the total optical
 482 depth magnitude.

483
 484
 485 Clouds are a major factor in the effort to quality control remotely sensed aerosol data (Smirnov et al. 2000; Martins
 486 et al. 2002; Kaufman et al., 2005; Chew et al., 2011; Kahn and Gaitley 2015). A significant portion of the liquid
 487 cloud contribution is removed by the prescreening prior to Level 1.0 as discussed in Sect. 3.1.3. The $\tau_{app\ Total}$ should
 488 be adjusted based on a multiplier dependent on the cirrus crystal size ($\tau_{correct} = C_{cirrus} * \tau_{app\ Total}$) according to Kinne et
 489 al. (1999). While this cirrus coefficient (C_{cirrus}) is not specifically modelled by Kinne et al. (1999) for the Cimel
 490 instrument field of view half angle of 0.6° , this multiplier is likely to be close to one for small cirrus crystals (e.g.,

491 $r_{\text{eff}}=6\mu\text{m}-16\mu\text{m}$), but near two for larger cirrus crystal sizes (e.g., $r_{\text{eff}}=25\mu\text{m}-177\mu\text{m}$). These adjustment factors
492 would result in the reduction of the $\tau_{\text{app Total}}$ due to forward scattering in the presence of cirrus. On the other hand,
493 liquid water cloud droplets would significantly increase the $\tau_{\text{app Total}}$ in a manner similar to large dust particles.

494
495 Cimel instruments also may have internal and external anomalous conditions that modify the optical characteristics
496 or response of the instrument resulting in amplification or dampening impacts (f_{anomaly}) of varying magnitudes on
497 the computation of the $\tau_{\text{app Total}}$. These anomaly adjustments can be difficult to quantify and can have strong
498 dependence on optical air mass (m) or the sensor head temperature (T_s). As a result, the following sections will
499 describe the mechanisms in which these additional cloud and anomaly components are automatically eliminated or
500 reduced as close to zero as possible to provide a quality assured AOD (τ_{aerosol}) after final calibration is applied (see
501 Sect. 4) across the global AERONET [AOD](#) database.

502 3.2.1 Cloud Screening Quality Controls

503 As Level 1.0 AOD data may have cloud contamination, these data should be considered as potentially cloud
504 contaminated where the triplet measurement represents the apparent AOD ($\tau_{\text{app aerosol}}$) as defined in the previous
505 section. [Table 2](#) provides a summary of the cloud screening quality control changes from Version 2 to
506 Version 3 and these changes are discussed in detail below and Sect. 3.2.2.

507
508 Cimel triplet measurements are performed typically every three minutes (every 15 minutes for older instrument
509 types) and these triplet measurements can detect rapid changes in the $\tau_{\text{app aerosol}}$ by analyzing the maximum to
510 minimum variability (i.e., the $\Delta\tau_{\text{app aerosol}}\{\text{MAX-MIN}\}$). Assuming that spatial and temporal variance of aerosols
511 plus clouds is much greater than aerosols alone, in many cases, $\Delta\tau_{\text{aerosol}}$ would be near zero and $\Delta\tau_{\text{cloud}}$ should be
512 much larger than zero when especially liquid phase cloud droplets exist. For Version 2 and earlier databases,
513 Smirnov et al. (2000) methodology utilized all available wavelengths to perform $\tau_{\text{app aerosol}}$ triplet screening for cloud
514 contamination. Therefore, large triplet variability would indicate the presence of clouds due to large $\Delta\tau_{\text{cloud}}$.
515 Analyses (e.g., Eck et al., 2018) have shown that removing the entire triplet measurement when only one or more of
516 the shorter wavelengths indicates a large variation ($\Delta\tau_{\text{aerosol}}(\lambda)$ much greater than zero) may not be the most robust
517 approach. For example, in cases of highly variable fine mode aerosols such as smoke can produce large triplet
518 variability as a result of the inhomogeneous nature of the aerosol plume especially for shorter wavelengths (e.g.,
519 340nm, 380nm, 440nm) where fine mode dominated aerosol particles can have radii similar to short wavelength
520 measurements.

521
522 Considering these factors, several potential techniques were explored utilizing various wavelength combinations and
523 utilizing the Spectral Deconvolution algorithm (SDA) fine and coarse mode triplet separation (O'Neill et al., 2001,
524 2003). While the SDA algorithm derived triplets for coarse mode AODs relative change tended to show utility in
525 cloud removal, the SDA algorithm itself could not be applied universally to the AERONET database to due
526 anomalous results in which fine and coarse mode AODs can have a negative relationship when the number of

527 available wavelengths or wavelength range is not satisfied. Anomalies in SDA retrievals can occur when the
528 uncertainty in AOD is relatively large near solar noon compared to the magnitude of AOD as is sometimes the case
529 when only the pre-field deployment calibration has been applied. Upon further consideration of the triplet
530 variability technique, analyses indicated that using ~~the-all~~ three longest standard AERONET wavelengths (i.e.,
531 675nm, 870nm, and 1020nm) could be used to remove a triplet measurement when they have high triplet variability
532 that exceeds 0.01 or 0.015*AOD (whichever is greater). The reduction in the threshold of the triplet variability
533 criterion is proportional to the magnitude decrease AOD uncertainty compared to UV wavelengths (0.02) to those of
534 visible and near infrared wavelengths (0.01).

535
536 While Smirnov et al. (2000) did not impose an Ångstrom exponent limitation, Version 3 processing constrains the
537 $AE_{440-870nm}$ of Level 1.5 data to be within -1.0 and $+3.0$. In general, the $AE_{440-870nm}$ values outside this range are
538 unphysical and should not be used due to the inconsistency of the AOD spectral dependence. These inconsistencies
539 typically occur at very low optical depth (<0.05) where the uncertainty of the AOD may be up to 100% of the actual
540 value thus producing AE values that are invalid.

541
542 The AOD time series smoothness uses a number of numerical methods and fits dependent on the application. For an
543 AOD time series, rapid and large increases are usually the result of cloud contamination. In Version 2 and prior
544 versions, a technique proposed by Smirnov et al. (2000) to implement a smoothness methodology similar to
545 Dubovik et al. (1995). In this scheme, the triplet measurements were considered as discrete points and differences in
546 logarithm of $\tau_{app\ aerosol}$ and relative difference in times between those measurements were utilized to calculate the
547 first derivative differences in which an arbitrary parameter D (similar to the norm of the second derivative) is
548 calculated. In Version 2 and earlier versions, when the value of D was greater than 16 for an AOD measurement
549 time sequence for 500 nm or 440nm, then this triplet was removed from the data set. Further, the smoothness
550 procedure was repeated or measurements were rejected for the day if less than three triplets remained for the day as
551 discussed in Smirnov et al. (2000). While the D=16 threshold was empirically derived, the smoothness parameter is
552 somewhat arbitrary in origin and operates in logarithmic coordinates rather than natural ones. For example, the
553 distribution of aerosol measurements in a single day is typically normally distributed rather than logarithmically
554 distributed. Further, the D parameter smoothness procedure was not always successful at removing cloud-
555 contaminated data and this may be related to the fact that the empirically derived D parameter was tuned for 15-
556 minute triplet measurement intervals rather than three-minute intervals now commonly observed in the network.
557 Therefore, an approach adhering to the relative change in the total optical depth with time is feasible and a more
558 straightforward physical quantification of the change in $\tau_{app\ aerosol}$ with time.

559
560 The AOD time series smoothness in Version 3 evaluates the same $\tau_{app\ aerosol}$ 500nm wavelength (or 440nm if 500nm
561 is not available). The Version 3 smoothness method computes the relative rate of change of $\tau_{app\ aerosol}$ per minute and
562 if $\Delta\tau_{app\ aerosol}/\Delta t > 0.01$ per minute, then the larger triplet measurement in the pair is removed and the smoothness
563 procedure will continue to remove triplets until measurement pairs in the day do not surpass the smoothness

564 threshold. The selection of this threshold of 0.01 per minute hinges on the premise that the triplet average does not
565 change rapidly within one minute. The Version 3 smoothness procedure could be affected by extreme changes in
566 AOD due to anomalous aerosol plumes (e.g., biomass burning or desert dust plumes) where ~~no-temporal~~ strong
567 gradient exists.

568
569 After the cirrus cloud screening quality control (to be discussed in the Sect. 3.2.2), triplets are evaluated for spurious
570 or isolated measurements remaining during the day after applying the cloud screening quality control procedures.
571 So-called “standalone points” may be relevant given the ability of the instrument to perform measurements in cloud
572 breaks or gaps. Here, the definition of a standalone triplet is when no triplets are available within 1 hour of the
573 measurement. If the $AE_{440-870nm}$ is greater than 1.0, the algorithm retains the triplet measurement; otherwise, the
574 measurement will be removed from the data set. ~~Finally~~Further, daily averaged data are evaluated for temporal
575 stability using the AOD stability during the day at 500nm (or 440nm) and daily outlier triplets using the 3-sigma
576 check for AOD at 500nm (or 440nm) and $AE_{440-870nm}$ to be within ± 3 standard deviations (Smirnov et al. 2000).
577 Finally, each wavelength is evaluated to be greater than or equal to -0.01 (based on uncertainty of 0.01; Eck et al.,
578 1999). At this point in the quality control algorithm, the remaining triplet measurements are not expected to have a
579 major component of τ_{cloud} or τ_{cirrus} .

580

581 3.2.2 Novel Cirrus Removal Method Utilizing Solar Aureole Curvature

582 Utilizing satellite and surface-based LIDAR, studies have shown the AERONET Version 2 Level 2.0 AOD data are
583 impacted by homogeneous optically thin cirrus clouds with a bias up to 0.03 in AOD (DeVore et al., 2009; Chew et
584 al., 2011; Huang et al., 2011). The optically thin cirrus bias can influence radiative forcing calculations and satellite
585 validation when clouds contaminate the measurement (DeVore et al., 2012). In addressing the shortcoming of
586 Smirnov et al. (2000) and manual checks in which the identification of optically thin cirrus clouds give relatively
587 weak signal in the AOD or AE, the authors leveraged high angular resolution radiance measurements routinely
588 performed in the solar aureole region (3.2° – 6.0° scattering angle range). While cirrus detection may be possible with
589 other scattering angle ranges, Cimel Sun photometer radiance measurements do not presently have high enough
590 angular resolution from 6.0° – 35.0° to reliably and consistency detect cirrus induced atmospheric phenomena (e.g.,
591 solar halos and sun dogs), since these events depend on cirrus crystal shape and orientation and are not always
592 detectable beyond levels of cloud optical depth variability.

593

594 The use of the solar aureole radiance (L_A ; $\mu W/cm^2/sr/nm$) with respect to the scattering angle (φ ; in radians) has
595 been demonstrated using the Sun and Aureole Measurement (SAM) aureolegraph instrument to indicate the
596 presence of large particles such as cirrus crystals (DeVore et al., 2009, 2012; Haapanala et al., 2017). The effect of
597 the surface reflectance is much less than the radiance of the solar aureole so it is ignored; however, this may become
598 important at very large solar zenith angles and bright surfaces such as snow (Eiden 1968). All Cimel instrument
599 models perform solar aureole measurements at the nominal 1020nm wavelength. The Cimel performs solar triplet

600 measurements directly on the solar disk, while solar aureole radiances are measured mainly during the almucantar,
 601 principal plane, and hybrid sky scans. These solar aureole measurements are performed hourly for Models 4 and 5
 602 instruments during sky scan scenarios and for Model T instruments before each solar triplet as well as for the hourly
 603 almucantar and hybrid sky scan measurements.

604
 605 The AERONET measurements of the solar aureole directional radiances (L_A) depend on the absolute calibration of
 606 the integrating sphere. The integrating spheres at the AERONET calibration centers provide an absolute calibration
 607 traceable to a NIST standard lamp hosted at the NASA GSFC calibration facility. The uncertainty in the radiance
 608 calibration is typically less than 3% due to systematic degradation in the lamp levels, changes in integrating sphere
 609 characteristics, and instrument spectral signal response. The solar aureole radiance magnitudes also depend on the
 610 instrument Sun sensitivity gain settings for each wavelength for Cimel Model 4 and 5 instruments, while the Model
 611 T instruments use an internal instrument gain switch applying to all wavelengths (Barreto et al., 2016). The L_A
 612 measurements have calibration and temperature correction applied and are measured by all Cimel instruments at the
 613 440nm, 675nm, 870nm, and 1020nm wavelengths. Due to lower AOD in fine mode aerosol loading situations, less
 614 Rayleigh scattering, and lower calibration uncertainty, the L_A measurements at 1020nm have less noise for
 615 evaluating cirrus cloud presence.

616
 617 Given that the L_A measurements are performed at discrete φ , we calculate the ordinary least squares linear regression
 618 fit on logarithmic scale when more than three scattering angles are available to determine the intercept (a), slope (b),
 619 and the correlation coefficient (R). If R is less than or equal to 0.99, then we do not proceed to check for cirrus
 620 contamination. When R is greater than 0.99, the curvature (k_ϕ) for the first available scattering angle (ϕ_0) in the
 621 3.2° – 6.0° scattering angle range is calculated using the equation of curvature of the signed planar curve, which gives
 622 the rate of turning of the tangent vector in Eq. (10)(40) (Kline 1998):

$$k = \frac{y''}{(1 + y'^2)^{\frac{3}{2}}} \quad (10)a$$

624
 625 The curvature (k) can be formulated by assuming the Power Law function and its derivatives, and, in our
 626 application, using the first scattering angle (ϕ_0) in radians for φ below:

$$y = a * \varphi^b \quad (10)(40)b$$

$$y' = a * b * \varphi^{b-1} \quad (10)(40)c$$

$$y'' = a * b * (b - 1) * \varphi^{b-2} \quad (10)(40)d$$

628
 629 According to the k formulation, the stronger the forward scattering peak, then the smaller the value of curvature
 630 since the second derivative is small and the first derivative is large due to the steepness of the solar aureole
 631 radiances. Further, the overall slope of curvature for all of the scattering angles (3.2° – 6.0°) can be calculated using

632 the assumption that $y^2 \gg 1$ rendering the addition of 1 in the denominator of Eq. (10) insignificant. The slope
 633 of the logarithm of curvature versus logarithm of scattering angle is desired and this slope can be calculated using a
 634 and b from the linear regression above by converting from logarithmic coordinates. Therefore, we derive the Eq.
 635 (11) to determine the slope of curvature dependent only on the slope of the linear regression fit of L_A and ϕ on
 636 logarithmic scale as follows:

$$\ln k = a + (1 - 2b) * \ln \phi \quad (11)$$

638 Here, the slope of curvature (M) is defined as $(1-2b)$. The value of M will typically be positive since b will tend to
 639 be negative due to the dimming of the solar aureole with increasing scattering angle. Alternatively, M can be
 640 calculated numerically for each k and ϕ to obtain similar results. A small value of curvature (k_c) at the smallest
 641 scattering angle available represents the possible existence of large particles producing a forward scattering peak.
 642 The slope of curvature (M) represents the average characterization of the solar aureole shape across the scattering
 643 angle 3.2° – 6.0° range where a large magnitude signifies the potential presence of large particles as curvature
 644 increases with increasing scattering angle across the forward scattering peak.
 645

646 The Micropulse LIDAR Network (MPLNET) is a global network of LIDARs monitoring the vertical distribution of
 647 aerosols and clouds (Welton et al., 2000, 2002; Campbell et al., 2002). To determine the thresholds for these Sun
 648 photometer solar aureole curvature parameters for different surface types and aerosol environments, the MPLNET
 649 LIDAR cloud identification database was used at eight collocated AERONET sites as shown in Table 3.
 650 Multi-year MPLNET LIDAR deployment data were analyzed and matched with AERONET observations when the
 651 solar zenith angle was less than 30° to minimize the spatio-temporal differences of the zenith pointing LIDAR
 652 versus the slantwise pointing of the Sun photometer in which sky condition can be quite different at large solar
 653 zenith angles. The MPLNET cloud base height data product was matched with MERRA reanalysis vertical
 654 temperature profile corresponding to the geopotential height pressure surface. When a cloud top temperature is less
 655 than -37°C , a cloud is designated to be cirrus, while other non-cirrus clouds may contain liquid or mixed phase
 656 particles (Sassen and Campbell, 2001; Campbell et al., 2015; Lewis et al., 2016). The partitioning the AERONET
 657 data set of solar aureole radiances in terms cirrus clouds, non-cirrus clouds, all clouds, and clear (no cloud base
 658 detected) sky condition categories allowed for the empirical determination of potential thresholds for the curvature
 659 parameters. For each site, AERONET curvature parameters (k and M) were computed for almucantar and principal
 660 plane solar aureole (L_A) measurements (i.e., left and right scans separately) and further categorized based on the
 661 coincident LIDAR detected sky condition. These solar aureole radiances have calibration and temperature
 662 characterization applied for the 1020nm channel and these L_A measurements were only quality controlled based on
 663 the correlation threshold of 0.99 discussed above.
 664

665 Figure 4a shows the number distribution of the k at NASA GSFC (38.99° N, 76.84° W) for each of the four
 666 LIDAR sky condition categories. The number of the potential clouds is large for magnitudes of k less than $2.0\text{E}-5$.
 667

668 Similarly, Fig. 44b and Fig. 44c show the number distributions of the M at NASA GSFC for each LIDAR sky
669 condition category. In Fig. 44b, the number of potential clouds generally dominates when the M is greater than 4.3
670 with generally clear or possibly cloudy conditions when M is less than or equal to 4.3. Some overlapping of the
671 categories for M may be related to the differences in the viewing geometry of the sky between the Sun photometer
672 and the LIDAR or inhomogeneous cloud conditions.

673
674 Algorithmically combining the two thresholds of k and M produces a defined distribution of clear versus cloudy sky
675 condition categories. When the threshold of $k < 2.0E-5$ is applied first, then the distribution of mainly cloudy
676 conditions becomes more distinct as shown for NASA GSFC in Fig. 44c. The maximum in the number distribution
677 for cirrus is near $M=4.6$ and the maximum in the number distribution of clear sky condition is at $M=4.3$ (Fig. 44c).
678 At Singapore (1.29° N, 103.78° E), Fig. 55c suggests that the distinction of small aerosol particles and larger cirrus
679 cloud ice crystals allows for adequate separation to identify an observation as cloud contaminated using a threshold
680 of M greater than 4.3. Figure 6a shows the number distribution of the curvature at the first scattering angle
681 for coincident AERONET and MPLNET observations at the SEDE BOKER (30.85° N, 34.78° E). Figure 6c
682 shows the distinction is similarly distributed as GSFC and Singapore to potentially identified cirrus contaminated
683 observations. For Fig. 66a, the clear sky condition category is much higher in number than other sky condition
684 categories; however, the k values less than the first scattering angle threshold of $2E-5$ (shown by the orange vertical
685 line) indicates a significant presence of dust particles rather than cirrus clouds due to forward scattering of dust.
686 Note that as for Fig. 44 and Fig. 55, the x-axis of Fig. 66a is truncated to $1E-4$ but the number distribution continues
687 at values near zero for larger first point curvatures. SEDE BOKER data in Fig. 66c exhibits a significant
688 contribution of clear conditions are preserved indicating that this method does not appear to misidentify dust as
689 cirrus at this mixed dust and urban pollution site.

690
691 When evaluating all of the collocated AERONET/MPLNET sites in Table 3 (Fig. 77), the maximum in the
692 number distribution for cirrus is at $M=4.3$ after the $k < 2.0E-5$ threshold is applied with a relative minimum for the
693 clear conditions for $M > 4.3$. Given this information, an empirical threshold of $M > 4.3$ can be established for
694 maximizing the removal of cirrus clouds and minimizing removal of potentially clear data points. As mentioned
695 previously, the almucantar and principal plane sky scans are performed on an hourly basis. If cirrus clouds are
696 homogeneously distributed in the sky, then this assumption allows for the application of the temporal screening of
697 triplet measurements within 30 minutes of the solar aureole measurement time. As a result, a significant number of
698 cirrus contaminated measurements for $M \leq 4.3$ are likely removed with this procedure given the normally distributed
699 number distribution of cirrus identified solar aureole measurements around $M=4.3$. For the Cimel Model T
700 instruments, sky scan aureole measurements are superseded by a special solar aureole scan (CCS) performed from
701 3.0° to 7.5° scattering angle range at 0.3° increments (left and right) after each triplet solar measurement; therefore,
702 temporal screening for these triplet measurements is applied within two minutes of the CCS scan. Overall, the
703 aureole curvature cirrus cloud screening quality control decreases the probability of a cirrus bias in the AOD data set
704 globally by using this standard procedure. However, the Version 3 Level 1.5 AOD data set may still be influenced

Formatted: Font:

Formatted: Font:

Formatted: Font:

Formatted: Font:

Formatted: Font:

Formatted: Font:

Formatted: Font:

Formatted: Font:

Formatted: Font: Do not check spelling or grammar

Formatted: Font:

Formatted: Font:

Formatted: Font:

705 by optically thin or sub-visible cirrus clouds with ice crystals similar in diameter to coarse mode aerosols such as
706 those found at polar latitudes or when solar aureole measurements are not available due to instrument malfunction or
707 incomplete data transfer.

708
709 [Figure 8](#) shows solar aureole radiances have significant nonlinearity with scattering angle when impacted by
710 cirrus clouds while measurements without cirrus are more linear. The SEDE BOKER site is influenced by desert
711 dust. Dust particles can affect the calculation of the k parameter to be close to the threshold of $2E-5$ even when
712 cirrus clouds are not present (SEDE BOKER case 1); however, the overall slope is more linear for the non-cirrus
713 case compared to the cirrus case (SEDE BOKER case 2). As a result, the M parameter is much lower and the
714 algorithm action would be to preserve the SEDE BOKER Case 1 data and remove data for SEDE BOKER case 2.
715 Note that the k parameter is quite low for SEDE BOKER Case 1 and in general dusty sites may frequently have k
716 less than $2E-5$; therefore, the M curvature parameter is needed to prevent inadvertent removal of aerosol data. For
717 fine mode at GSFC case 1 and Singapore, small values of k and large values of M result in removal of the cirrus-
718 contaminated data. For comparison, the GSFC case 2 shows significant linearity when cirrus clouds are not present.
719 The GSFC case 3 and Trinidad Head case show the variation in these curvature parameters at low optical depths in
720 which only one of the curvature parameters indicates the possibility of cirrus clouds. While these two curvature
721 parameters may be used independently in certain conditions, the current algorithm must employ both curvature
722 parameter thresholds to avoid inadvertently identifying aerosols as clouds in dust and low aerosol loading
723 conditions.

724 3.3 Level 1.5 Quality Controls to Screen Instrument Anomalies

725 While cloud-screening quality controls remove a significant portion of data impacted by cloud contamination and
726 some instrument anomalies, a portion of the remaining AOD data set can be impacted by internal or external
727 instrument anomalies. Most instrument anomalies can be removed utilizing the prescreening steps outlined in the
728 Sect. 3.1, but a number of issues still exist which are more evident after the cloud screening quality controls have
729 been applied to the data set. A data set with some clouds can mask or offset patterns in the AOD spectra that can
730 clearly identify data anomalies dependent on optical air mass. For AERONET instruments, data anomalies either
731 dependent on the optical air mass, the sensor head temperature, or leakage, degradation, or looseness of the optical
732 interference filter. Section 3.1 addresses the quality control procedure with respect to the instrument temperature
733 dependence. Some instrument anomalies dependent on the optical air mass include deviations of the measurement
734 time to the true time (i.e., time shift) and obstruction of light into the silicon or InGaAs detector (e.g., dust, moisture,
735 spider webs). Measurements performed at high latitudes have a slowly varying optical air mass and thus optical air
736 mass pattern recognition is more difficult. The AOD spectra may have optical air mass dependence for out of band
737 leakage or degradation of transmittance due to irregularities in the optical filter composition or the AOD may have
738 significant variability due to a loose filter inside the sensor head.

739

740 The retained spectral AOD measurements passing the quality controls from Sect. 3.1 and Sect. 3.2 are evaluated as
741 input for the quality controls in the present section. The removal of nearly all of the clouds and most instrument
742 anomalies from the previous steps allow for more defined pattern recognition. This section will discuss the pattern
743 recognition techniques utilized for the time shift and AOD diurnal dependence, provide a description of the detector
744 consistency, and AOD spectral dependence quality controls. Further, the AOD diurnal dependence algorithm can be
745 used jointly with the detector consistency and AOD spectral dependence quality controls to remove anomalous data
746 with more certainty. These quality controls can be applied for multiple days to remove data impacted by anomalies
747 for more than one day even when clouds interrupt the day-to-day AOD pattern. The final data set is evaluated for
748 the remaining number of observations in a day and deployment period.

749 3.3.1 Time Shift Screening

750 AERONET data are transferred by satellite Data Collection Platform (DCP), PC, or SIM card data transfer. The
751 older Vitel satellite transmitters provided a handshake between the instrument and transmitter allowing for time
752 adjustment and newer Sutron Satlink transmitters provide a GPS time stamp to each message. While time shift is
753 not an issue for satellite transmissions, the time shift can become more significant for PC data transfer and even
754 some instruments using SIM card data transfer. AERONET has developed a program called cimel_https_connect
755 that can update the processing unit clock of Cimel Model 5 instruments. Older instruments (Model 4) and old non-
756 AERONET data transfer software (e.g., Cimel ASTPwin) do not have the capability to synchronize the Cimel
757 control box with the time-synced AERONET server. Most non-AERONET software requires the PC time to be
758 updated from a timeserver or GPS system to provide accurate clock synchronization. Even some newer Model T
759 instruments transferring data by PC or SIM can have faulty GPS modules in which the clock deviated significantly.
760 Cimel Model T instruments may allow for the PC software (e.g., cimelTS_https_connect) updating the time and
761 overriding the GPS module.

762
763 A Cimel clock that deviates from true time can result in an optical air mass calculation not appropriate for the actual
764 time especially when the optical air mass varies relatively rapidly diurnally. This instrument anomaly can result in
765 significant changes in the AOD, which affects all wavelengths but most greatly shorter wavelengths (e.g., 340nm,
766 380nm, and 440nm) at large optical air mass when it changes rapidly. In general, longer wavelength AODs (675nm,
767 870nm, and 1020nm) have less impact from erroneous optical air mass calculations due to less influence of
768 molecular (Rayleigh) scattering. As a result, AODs from the longer wavelengths tend to be more stable and AODs
769 from the shorter wavelengths will tend to crossover the longer wavelengths only at one end of the day (near sunrise
770 or near sunset). The timing of the wavelength crossover depends on whether the Cimel clock is too fast or too slow
771 with respect to the actual time. For example, if the time is slow (fast) relative to the actual time, the temporally
772 deviated optical air mass magnitude will be larger (smaller) than the actual optical air mass and thus the short
773 wavelength AODs will be lower (higher) and possibly cross the longer wavelength AODs (significantly increase
774 spectral dependence). In general, Cimel clock temporal deviations in AOD data can be identified using the
775 following:

- 776 1. When the shortest available wavelength AOD crosses neighboring UV, visible, and NIR channel
777 AODs near sunset and the short wavelength AOD is decreasing significantly relative a longer stable
778 wavelength (e.g., 870nm) AOD, this condition indicates the Cimel clock is too fast (Fig. 99a).
779 2. When the shortest available wavelength AOD crosses neighboring UV, visible and NIR channel
780 AODs near sunrise and the short wavelength AOD is increasing significantly relative to a longer stable
781 wavelength (e.g., 870nm) AOD, this condition indicates the Cimel clock is too slow (Fig. 99b).

Formatted: Font:

Formatted: Font:

782
783 The AOD differences and trends are used for a specific optical air mass interval (2.5–7.0), where the temporal clock
784 deviation amplifies the error in optical air mass calculations. Individual day screening is limited to mainly cloud
785 free periods with low AOD in areas with significant variation in optical air mass from ~1.0–7.0.

786
787 The time shift algorithm is applied over a multi-day period. The algorithm scans the current day plus 19 days in the
788 past (~3 week period) to determine if three or more days indicate the occurrence of a time shift. If the multi-day
789 time shift criteria of three or more days are met, then data between the current day and the last occurrence of the
790 time shift are removed from the field deployment. Although the Cimel clock could possibly be adjusted
791 periodically, most time shift issues tend to occur at remote sites and this approach will maximize the removal of data
792 over the multi-day period to minimize the negative impact on the data from the clock-shifted anomalies. Moderate
793 to high aerosol loading can partly mask the temporal AOD time shift pattern and these data periods may not be
794 removed completely unless they occur between periods of lower aerosol loading when the clock shift spectral AOD
795 pattern is more defined.

796

797 3.3.2 Detector Consistency Quality Control

798 The instrument external collimator on the sensor head avoids stray light and reduces front lens contamination, while
799 the internal sensor head defines the field of view of the instrument (nominally 1.2°) by the achromatic front lens,
800 filter, and field stop before each detector. The external collimator is composed of two tubes and the aperture design
801 varies slightly by instrument type. The Cimel Model 4 instrument type has two Silicon photodiode detectors in the
802 sensor head to measure the Sun and sky while newer model instruments have one Silicon photodiode and one
803 InGaAs photodiode detector to measure the Sun and sky on both detectors. One of the detectors could be impacted
804 by an obstruction such as a spider web, insect debris, dust, or moisture. For Cimel Model 4 and some Model 5
805 instruments, the sky scan scenario performs two measurements at the 6° azimuth angle for the almucantar and 6°
806 scattering angle for the principal plane at each wavelength over both detectors. For these older instruments, the
807 solar aureole gain is used for the solar Silicon diode detector and the sky gain is used for the sky Silicon diode
808 detector. These redundant measurements can allow for detection of the change in the relative signal but this method
809 is currently more appropriate to use for quality controlling the inversion products due to uncertainty in sky
810 calibration. Newer Model 5 and Model T instruments (with the solar and sky measurements performed on both
811 detectors) do not have the redundant sky measurement; instead, these instruments have a redundant solar

812 measurement at 1020nm in both collimator tubes, where each solar measurement of the triplet is performed within
 813 eight seconds of each other. The AOD 1020nm measurements on Silicon and InGaAs detectors can be compared
 814 directly to determine if an obstruction exists in front of either of the detectors. Applying a similar approach to Giles
 815 et al. (2012), the difference limit ($\Delta\tau_{Limit}$) can be computed using the optical air mass and AOD magnitude dependent
 816 formulation (Eq. (12)(42)):

$$\Delta\tau_{Limit} = \frac{(0.04 + (0.02 * MIN[\tau_{1020nm}]))}{m} \quad (12)$$

817
 818 where $MIN[\tau_{1020nm}]$ is the minimum of the AOD at 1020nm obtained from the redundant AOD 1020nm
 819 measurements on Silicon and InGaAs detectors and m is the optical air mass. The difference limit for an AOD
 820 1020nm minimum of 1.0 will result in the 0.06/m 1020nm difference limit described in Giles et al. (2012). A more
 821 lenient approach is used here based on the AOD magnitude to prevent removal of data for low AOD at 1020nm. At
 822 low AOD, the average field instrument uncertainty (up to 0.01) becomes more significant while the maximum AOD
 823 error occurs at midday and differences due to their temperature dependency can contribute up to 0.02 AOD bias.
 824 Given the relative difference in the AOD 1020nm measurements, the maximum uncertainties in both 1020nm
 825 measurements must be considered. Therefore, the 0.02 threshold is derived from the average uncertainty (up to
 826 0.01) and the 0.04 limit is derived from the maximum midday error in AOD and temperature dependency (up to
 827 0.02). When more than 10% of the total measurements for the day exceed the $\Delta\tau_{Limits}$, data are removed in the
 828 following manner:

- 830 1. If the AOD 1020nm Silicon subtracted by the AOD 1020nm InGaAs detector is greater than $\Delta\tau_{Limits}$, then the
 831 Silicon side has an obstruction and the entire measurement is removed for both Silicon and InGaAs AOD
 832 data.
- 833 2. If AOD 1020nm Silicon subtracted by the AOD 1020nm InGaAs is less than $-\Delta\tau_{Limits}$, then the InGaAs
 834 detector has an obstruction and only the InGaAs AOD for 1020nm and 1640nm measurements are
 835 removed.
- 836 3. If the redundant AOD 1020nm values are nearly the same ($-\Delta\tau_{Limit} \geq \Delta\tau \geq \Delta\tau_{Limit}$), then an obstruction could
 837 possibly exist in the event that a substance (e.g., spider webs, dust, moisture) similarly obstruct both
 838 detectors.

839 For condition (3), this case is further evaluated by the AOD diurnal dependence quality control in the next section.

840 3.3.3 Aerosol Optical Depth Diurnal Dependence

841 The AERONET instrument has spectral calibrations made and typically applied both before and after field
 842 deployment. When the instrument operates in the field, the pre-field spectral calibration applied to the near real-time
 843 data is constant. If the calibration changes significantly during the instrument deployment, the error in the
 844 computation of the AOD increases with decreasing optical air mass where the maximum error occurs when optical
 845 air mass approaches one ($\delta\tau * m$; Hamonou et al., 1999). As a result, an apparent diurnal dependence in the AOD can
 846 occur depending on the magnitude of the deviation from the pre-field calibration. When both the pre-field and post-

847 field calibrations are applied and data still show a diurnal dependence in the AOD, then the deviation in the field
848 measurements is due to a non-linear change in the calibration coefficient since Level 2.0 data utilize a linear
849 interpolation between the pre-field and post-field calibration coefficients.

850
851 Midday maximum (concave pattern) or midday minimum (convex pattern) of AOD diurnal dependence can be
852 observed at any AOD magnitude but are typically more pronounced at lower aerosol loading due to calibration
853 offset (Cachorro et al., 2004) or instrument anomalies. Quality controls developed for the analysis of the AOD
854 diurnal dependence need to consider the impact of clouds and missing data to assess whether to remove these data
855 while minimizing the removal of data exhibiting true diurnal dependence. For example, one cloud-free day may
856 show diurnal dependence, but on another day, the morning or afternoon data may not be available due to missing
857 data during cloudy or rainy periods. The algorithm must have a sufficient number of observations to perform a
858 robust assessment of the AOD diurnal dependence.

859
860 Variation in the number of available measurements in a day due to clouds or instrument issues can limit the
861 application of a single day only approach. As a result, the morning and afternoon periods must have at least five
862 measurements separately and the analysis of the full day must have at least 10 measurements. To analyze the
863 diurnal dependence and reduce the impact of outliers, the GNU Scientific Library robust least squares (RLS) linear
864 regression fit is performed for AOD versus the inverse optical air mass (m^{-1} , where m is approximately the cosine of
865 the solar zenith angle). The slope and correlation coefficient (R) values derived from the linear fit are used as
866 thresholds to determine the magnitude and strength of the diurnal dependence (Table 4Table 4).

867
868 The nominal AERONET 440nm, 675nm, 870nm, and 1020nm wavelengths for the Silicon detector and 1640nm for
869 the InGaAs detector are assessed for diurnal dependence and potential removal of all spectral channels. An example
870 of the AOD diurnal dependence of 1020nm wavelength is shown in Fig. 1010 at the Rio Branco (9.96° S, 67.87° W)
871 AERONET site where the site manager indicated spider webs were obstructing measurements. If data are removed
872 for the InGaAs detector, then only InGaAs detector data are removed, while removal of the Silicon detector data will
873 remove all data including InGaAs detector data, if any. The AOD diurnal dependence is classified as two
874 categories: independent and dependent. If the algorithm meets the strict thresholds for “independent” diurnal
875 dependence, then all channels exhibiting diurnal dependence can remove data for a day, except the 1020nm channel
876 since some old data with temperature defaults may exhibit false diurnal dependence. Otherwise, all of the above
877 channels are used for the “dependent” diurnal dependence quality control. The dependent diurnal quality control
878 relies on more lenient thresholds for the slope and R ; however, the removal of data generally requires that another
879 quality control flag is set such as the detector consistency quality control (Sect. 3.3.2), where an obstruction was
880 identified in front of one of the detectors or at least one additional qualified wavelength meeting the slope and R
881 thresholds. When a qualified wavelength indicates dependent AOD diurnal dependence for Day or both AM and
882 PM and the AM and PM slopes are positive, then the entire day can qualify for independent removal. This

Formatted: Font:

883 methodology allows for a more skilled approach in removing only data affected by instrumental anomalies while
884 minimizing the removal of data coincidentally producing a true diurnal dependence signature.

885
886 The AOD diurnal dependence identification can be complicated by changes in aerosol loading during the day, cloud
887 artifacts, and missing data. A multi-day scan must be performed to maximize the removal of data impacted by
888 instrument anomalies. A multi-day assessment example is provided in Fig. 11 for Rio Branco. Figure 11
889 11a shows that the spectral AOD varies significantly diurnally for the period from 26 August to 5 September 2011,
890 especially for the 870nm and 1020nm near infrared wavelengths. Figure 11 11b shows evaluation of the
891 slope and correlation coefficient (R) for the AOD 1020nm daily variation, which shows 7 of the 10 days exceeding
892 the thresholds (slope > 0.1 and R>0.94) and wavelengths established in Table 4. For these data to qualify for
893 dependent AOD diurnal dependence removal, additional information is needed such as another qualified wavelength
894 with slope and R exceeding the thresholds. For this case, the AOD 870nm daily slope and correlation parameters
895 (not shown) also exceed the thresholds, which lead to the elimination of these data from Levels 1.5 and 2.0. Similar
896 to the time shift screening in Sect. 3.3.1, the AOD diurnal dependence algorithm scans the last 19 days including the
897 current day to determine the first occurrence and last occurrence of the dependent and independent AOD diurnal
898 dependence. When three or more days are identified, data are removed from the first occurrence to the last
899 occurrence of AOD diurnal dependence during the 20-day period. The multi-day screening allows for the
900 elimination of data affected by an obstruction in the instrument field of view even with moderately high aerosol
901 loading in the NIR wavelengths and when days with incomplete number of measurements from the established
902 protocol due to clouds.

903 3.3.4 Reverse Spectral Dependence

904 While the majority of the cloud screening quality controls remove aerosol measurements contaminated by clouds,
905 some spurious points or slowly varying changes in cloud properties may still affect the data set at this point in the
906 algorithm. A new method (Fig. 12) utilizing the Ångström exponent (AE) is applied to the remaining data set for
907 evaluation of cloud contamination. Ångström exponents derived from anomalous AOD measurements due to
908 instrument artifacts may produce a similar signature. The spectral dependence among the wavelengths is now much
909 improved compared to Version 2 by removing temperature dependencies that influenced the calculation of the AE at
910 low AODs reducing the effect of improper spectral dependence due to temperature anomalies.

911
912 The AE is computed utilizing the ordinary least squares fit of the logarithms of AOD and wavelength for the ranges
913 of 440–870nm, 870–1640nm (if 1640nm is available), and the 870–1020nm (for Silicon detectors only) range (Eck
914 et al., 1999). The reverse spectral dependence algorithm in Fig. 12 removes cloud contaminated points utilizing
915 these AE ranges depending on the instrument model.

916 Figure 13 shows the removal of the anomalously high AOD at the Bratts Lake (50.20° N, 104.71° W)
917 AERONET site in southwest Canada. In Fig. 13 13b, all negative and a few positive AE values are identified and the
918 algorithm removes nearly all of the residual cloud contamination in this case. However, the penultimate and final

Formatted: Font:

Formatted: Font:

Formatted: Font:

Formatted: Font: 10 pt, Not Bold

919 measurements in Fig. 13.3c have slightly higher AOD than the previous hour of data, which may be due to marginal
920 contamination by optically thin cirrus clouds. Additional algorithm development is still needed to further enhance
921 the removal cloud contaminated data with small ice crystals while not removing dust aerosols.

922 3.3.5 Aerosol Optical Depth Spectral Dependence

923 The wavelength dependence of AOD typically is strong for fine mode aerosols (e.g., pollution or smoke) and weak
924 for coarse mode aerosols (e.g., dust or sea salt). The AE provides an index of the strength of the spectral
925 dependence related to the estimation of the possible aerosol size (Eck et al., 1999). In general, the $AE_{440-870nm}$ will
926 typically provide values between approximately 0.0 and 3.0. These prospective values indicate no spectral
927 dependence at $AE_{440-870nm}$ of 0.0 and very strong spectral dependence with an $AE_{440-870nm}$ near 3.0 (AE values of 3.0
928 have not been observed in good quality data with sufficiently high AOD). The spectral dependence can be used to
929 evaluate the quality of each channel given that most channels in the measurement suite adhere to the stated AOD
930 uncertainty of 0.01 for wavelengths $\geq 400nm$ and 0.02 for wavelengths $< 400nm$ (Eck et al., 1999). The fit of the
931 AOD with wavelength on logarithmic scale should generally be linear for coarse mode dominated or fine/coarse
932 mode particle mixtures. However, in moderate to high aerosol loading cases (especially when fine mode
933 dominated), a quadratic or cubic assumption is needed to fit the data depending on the wavelength range under
934 evaluation (Eck et al., 1999; O'Neill et al., 2008). The ordinary least squares (OLS) methodology is perturbed by
935 the presence of outliers and therefore skews the fit towards outliers. If the boundary wavelengths are impacted by
936 anomalies, the ordinary least squares can poorly fit other intermediate wavelengths.

937
938 In an effort to reduce the influence of outliers, the GNU Scientific Library (GSL Version 2.2.1 C compilation)
939 robust least squares (RLS) technique is utilized to improve the removal of spectral AOD outliers. In general, the
940 OLS technique is sensitive to the endpoints and to the number of points used in the regression. For example, the
941 outlier detection will have less skill with a few points or anomalous endpoints. The RLS scheme uses an iterative
942 approach with up to 100 passes using the Tukey biweight function and assigning the outliers a lower weight with
943 each pass. The RLS approach allows for the more meticulous removal of wavelengths out of spectral dependence
944 and more importantly preserves mid-visible wavelengths that could be removed incorrectly when utilizing the
945 ordinary least squares method.

946
947 Outlier detection is performed utilizing the uncertainty of the AOD measurement and providing an allowable
948 tolerance in the fit given potential irregular nature of the uncertainty (0.01 to 0.02). For wavelengths $\geq 400nm$ and
949 $< 1600nm$, the allowable AOD difference between the measurements and fit for a candidate wavelength is
950 $(0.02 * AOD) + 0.02$, based on the stated AOD uncertainty for these wavelengths (Holben et al., 1998; Eck et al.,
951 1999). For wavelengths $< 400nm$ and $1640nm$, the allowable AOD difference between the measurements and fit for
952 a candidate wavelength is $(0.02 * AOD) + 0.04$, which is adjusted for greater uncertainty at the UV wavelengths and
953 greater uncertainty in the larger spectral range to fit the 1640nm wavelength.

954

955 The spectral outlier procedure begins by identifying and removing any negative AOD values that are not within the
956 allowable AOD difference from the RLS linear fit. Negative AOD due to slight calibration drift can be observed at
957 very clean locations; otherwise, these negative values may be anomalous. The algorithm will evaluate each
958 wavelength separately and compute the RLS linear fit based on the remaining wavelengths producing the slope,
959 intercept, and R^2 values, where the slope and intercept are used to compute the AOD fit at the wavelength under
960 evaluation. If the algorithm does not identify any wavelengths for removal, then the procedure is complete. If AOD
961 is low ($AOD_{440nm} < 0.1$) and one wavelength AOD exceeds the maximum allowable difference, then the wavelength
962 will be removed due to the linear fit deviation. However, if more than one wavelength has AOD marked for removal
963 for the low AOD condition, then the wavelength with the largest departure from the linear fit to the measurement
964 and largest R^2 will qualify for removal.

965
966 In the case of higher AOD ($AOD_{440nm} \geq 0.1$), the algorithm stores the information from the RLS linear fit and
967 continues to perform a RLS quadratic fit ($400nm \leq \lambda \leq 1020nm$) or a RLS cubic fit ($\lambda = 1640nm$). If the candidate
968 wavelength deviates from the allowable difference in fit to the measurements for the higher order fits, then the
969 wavelength will be removed if it is identified as a wavelength that corresponds to the maximum deviation for the
970 RLS linear fit. [Figure 14](#) provides an example of this condition at the Osaka (34.65° N, 135.59° E)
971 AERONET site. After each wavelength removal regardless of order of the fit, the algorithm repeats until no
972 wavelength removals occur or when less than three wavelengths remain.

973 3.3.6 Large Aerosol Optical Depth Triplet Variability

974 In addition to growth of hygroscopic aerosols near cumulus cloud boundaries and large triplet variability at short
975 wavelengths in highly variable fine mode plumes, a misaligned filter due to improper filter wheel movement or dust
976 on the filter may produce large AOD triplet variability (AOD Max – AOD Min). The cloud screening triplet
977 variability quality control ([Sect. 3.2.1](#)) removes the entire measurement when 675nm, 870nm, and 1020nm AOD
978 triplets [all](#) have large triplet variability exceeding the threshold (0.01 or $0.015 * AOD$, whichever is greater). A
979 situation may exist where one of those wavelengths or shorter wavelengths are impacted by a filter anomaly making
980 it necessary to assess the large AOD triplet variability. If the triplet measurement is identified for high AOD
981 retention ([Sect. 3.1.6](#)), then the following large adjacent triplet quality control is not performed because very high
982 aerosol loading in fine mode events can lead to large triplet variability naturally. Occasionally, if the triplet is very
983 large and exceeds the limit of $0.03 + 0.2 * AOD$, then the wavelength is removed independently of the next longer
984 wavelength.

985
986 To further screen anomalous triplets individually or the entire day, each triplet and wavelength is evaluated using the
987 triplet variability from the shortest wavelength (e.g., 340nm) and the next longer wavelength (e.g., 380nm). The
988 allowable triplet variability limit is computed based on the aerosol loading and the AOD triplet variability of the
989 next longer wavelength: $0.03 + 0.02 * AOD + \text{triplet_variability_of_next_longer_wave}$. If the total number of triplets
990 for a wavelength exceeding the large triplet variability threshold is more than 25%, then the AOD measurements for

991 the wavelength are removed completely for the entire day. ~~Figure 15~~Figure-15 shows the large triplet variability
992 removal at the PEARL (80.05° N, 86.42° W) AERONET site in northern Canada. The triplets at shorter
993 wavelengths may naturally exhibit relatively large triplet variability hence it is necessary to check the shorter
994 wavelength in comparison to the next longer wavelength which typically will be more stable if clouds do not impact
995 the measurements.

996 3.3.7 Remaining Measurements Evaluation

997 After the previous quality control algorithms have been applied, extraneous data points may remain and are
998 identified for possible removal. A number of conditions have been implemented based on the total data removed for
999 the day, number of wavelengths remaining for the day, and number of measurements for a wavelength for a
1000 deployment. These “cleanup” conditions below will remove all wavelengths in a day for any of the following
1001 conditions dependent on the “retain high AOD” from Sect. 3.1.6 and the number of wavelengths in a day:

- 1002 1. If retain high AOD and less than two wavelengths remain in a day
- 1003 2. If retain high AOD and two wavelengths but are not 870nm and 1020nm in a day
- 1004 3. If not retain high AOD and less than three wavelengths remain in a day
- 1005 4. If not retain high AOD and less than half of the wavelengths remain in a day

1006

1007 Each wavelength must be evaluated for remnant data artifacts. If greater than 50% of the total cloud screened AOD
1008 data for a wavelength in a day are removed, then AOD measurements for the candidate wavelength will be removed
1009 for the day. Further, a condition is implemented to remove specific wavelengths for an entire deployment. For
1010 example, if the number of measurements for a wavelength is less than 20% of the total cloud screened data set for a
1011 deployment, then all of the measurements for the specified wavelength will be removed for the deployment. These
1012 removal conditions are necessary to fully quality control the spectral AOD data set and avoid unphysically irregular
1013 and fragmented data sets.

1014 3.4 Algorithm Performance Assessment

1015 Data quality controls applied to the quality controlled Level 1.0 data set are evaluated for removal performance for
1016 each part of the Level 1.0 prescreening and Level 1.5 algorithm. The Level 1.0 prescreening is applied to about 84
1017 million solar triplet measurements from 1993–2018. The radiometric sensitivity screening (see Sect. 3.1.2) for the
1018 DN of 1020nm removes about 36% and the digital voltage triplet variance greater than 0.16 (see Sect. 3.1.3)
1019 removes nearly 11% of the Level 1.0 data. The remaining Level 1.0 prescreening that check for radiometric
1020 sensitivity screening for DN of 870nm, extreme temperatures ($T_S \leq -40^\circ\text{C}$ or $T_S > 100^\circ\text{C}$), and bad measurement
1021 configuration conditions remove approximately 0.5% of the Level 1.0 data. Therefore, nearly half (48%) of the
1022 initial 84 million solar triplet measurements are removed by the Level 1.0 prescreening steps due to the presence of
1023 clouds in the solar measurements that greatly reduce the signal (e.g., stratus clouds) or exhibit significant temporal
1024 variability within the one minute triplet measurement sequence (e.g., cumulus clouds).

1025

1026 The Level 1.5 quality control algorithm is divided into the two main steps for cloud screening and instrument data
1027 anomaly removal. [Figure 16](#)
1028 ~~Figure 16~~ shows the percentage of the Level 1.0 data removed by the Level 1.5 cloud screening quality control.
1029 Over 23% of the removal in the cloud screening algorithm was due to the large triplets at the long wavelengths
1030 (675nm, 870nm and 1020nm). Nearly 5% of the removal of the Level 1.0 data was due to the presence of cirrus
1031 clouds as detected by the solar aureole curvature algorithm and is significant since a cirrus contamination bias is
1032 evident in the AOD in Version 2 Level 2.0 data set. The “Unqualified” category indicates data that are ~~negative~~
1033 ~~AOD~~ ~~not triplets~~ or lack the sufficient channels to participate in the cloud screening part of the algorithm and these
1034 measurements are rejected from Level 1.5. Finally, spectral AOD removed due to too low negative values
1035 (AOD<-0.01) has maximum removal of approximately 0.5% for 380nm and 1% for 340nm of the total Level 1.5
1036 AOD measurements due to 0.02 uncertainty in the UV at very low optical depths, while other AOD wavelengths
1037 have generally much less than 0.5% removal. After all of the data are cloud screened, about 66% of the Level 1.0
1038 data are passed to the second part of the Level 1.5 instrument quality control algorithm for examination of the
1039 instrument anomalies and other spurious clouds and artifacts.

1040
1041 The second stage of the Level 1.5 quality control algorithm utilizes measurements passed from the cloud screening
1042 algorithm. While the cloud screening algorithm rejects the entire measurement in the presence of clouds, the
1043 instrument quality controls can also reject the entire measurement or remove data by wavelength depending on the
1044 anomalous condition. [Figure 17](#)
1045 ~~Figure 17~~ shows the removal of Level 1.5 cloud screened data due to mainly instrument anomalies for each
1046 wavelength. More than 2.5% of the data are removed due to the AOD diurnal dependence screening, about 2% for
1047 the time shift screening, and 1.5% for the AOD 1020nm difference screening. These three instrument quality
1048 control algorithms remove in general the most across all wavelengths. Some removal occurs significantly spectrally
1049 for the InGaAs channel (1640nm). The InGaAs channels can be affected in some instruments more significantly by
1050 water contamination as the InGaAs side of the collimator is facing away from the Sun when in the parked or resting
1051 position. Further, when the algorithm removes all of the Silicon channels, the remaining InGaAs channels are also
1052 removed since no other independent method exists to check the InGaAs channel data quality. The “Remaining”
1053 measurements removal shows that nearly 4% of the cloud screened data are removed from the InGaAs data set. The
1054 AOD spectral dependence removes more than 2% of the 340nm wavelength data, which tends to be the most
1055 unstable wavelength (due to filter degradation), and about 0.5% for all other wavelengths. The temperature
1056 screening removal of missing or anomalous temperatures mostly affects the Silicon 1020nm wavelength with nearly
1057 1% of the cloud-screened data removed due to its large temperature dependence compared to the other wavelengths.

1058 **4 Assessment of the Quality Assurance Data Set**

1059 The aerosol optical depth (AOD) data will be qualified for consideration of Level 2.0 once it passes the Level 1.5
1060 checks. To reach Level 2.0, these data must meet the following conditions:

- 1061 1. Data must have pre-field and post-field calibration applied; or in some cases, the pre-field deployment or
1062 post-field deployment calibration may be made constant for the deployment after evaluation of the best
1063 calibration values.
- 1064 2. Temperature characterization must be applied utilizing the temperature correction for the instrument or
1065 default values for each wavelength.
- 1066 3. Instrument must be designated as the primary instrument for the site.

1067
1068 Once the above conditions are met, these data are considered to reach Level 2.0. These Level 2.0 data are
1069 recommended for publication and use in various atmospheric applications. The automated [quality control](#) algorithm
1070 attempts to preserve aerosol data while removing data artifacts. Some unusual atmospheric conditions (e.g., small
1071 cirrus particles $r < 5\mu\text{m}$) or rare instrument anomalies (e.g., loose filters or partially removed multi-da AOD diurnal
1072 dependence) affecting the AOD may rarely pass through the algorithm and users are advised to consider inspecting
1073 these data carefully when using them for detailed studies. Further, optical air mass dependent anomalies such as the
1074 time shift and AOD diurnal dependence quality controls may allow data to pass when aerosol loading is high or too
1075 few data exist to make an assessment. These quality controls can determine patterns more skillfully at lower aerosol
1076 loading which could result in retaining potentially contaminated high aerosol loading periods when the pattern may
1077 be less defined and does not meet the quality control thresholds.

1078
1079 The subsequent sections discuss the impact of the temperature characterization on the Version 3 Level 2.0 AOD data
1080 to quantify the change in regards to the Version 2 Level 2.0 data set. Further, the assessment of the Version 3 near
1081 real-time product is made to determine the average bias of the AOD based on the applied calibration. Finally, an
1082 analysis is made of the Version 3 Level 2.0 AOD long-term averages for select AERONET sites and these are
1083 compared to the Version 2 Level 2.0 AOD long-term averages.

1084

1085 4.1 Temperature Characterization Evaluation

1086 The accurate measurement of the spectral direct-beam Sun intensity (from which AOD is computed) depends on the
1087 sensor head temperature of the instrument as discussed in Sect. 2. The sensor head temperature can vary
1088 significantly since the optical head canister is heated by the Sun and can be much higher ($>10^\circ\text{C}$) than the ambient
1089 temperature especially near solar noon. The temperature sensitivity of the Silicon detector is more significant for
1090 the 1020nm filter due to the proximity to the edge of the spectral range of the detector in which temperature
1091 dependence becomes more significant. The temperature dependence for all wavelengths may vary due to the
1092 composition and/or manufacturing quality of the filters and/or detectors. Due to technical difficulty, the ultraviolet
1093 wavelength ($\lambda < 400\text{nm}$) filters have not been temperature characterized in Version 3; however, UV filters may have
1094 a temperature dependence. [Figure 18](#) shows the difference in the AOD temperature coefficients for
1095 Version 3 temperature correction applied to Version 3 data and Version 2 temperature correction applied to Version
1096 3 AOD data from 1993–2018. The AOD varies most significantly for the Silicon 1020nm channel with a full range

1097 of ~ 0.02 for sensor head temperatures between -25°C and $+55^{\circ}\text{C}$. Notably, the shorter wavelength channels and the
1098 InGaAs wavelengths (i.e., 1020nm and 1640nm) do not show significant change in AOD less than 40°C . All of the
1099 wavelengths, except the Silicon 1020nm, show an AOD difference decrease from -0.005 to -0.010 for temperatures
1100 greater than 40°C , which may be due to changes in instrument characteristics (e.g., electronic instability in the
1101 instrument) at high temperatures. The decreasing AOD difference with increasing temperature may be related to the
1102 smaller number of observations at high temperatures and contribution by instruments with temperature
1103 characterization measurements that did not reach temperatures greater than 40°C . Temperature characterization has
1104 proven to be small yet necessary adjustment to the AOD computation and this improvement is especially exhibited
1105 in [arctic-polar](#) regions or sites with very low aerosol loading in which the Version 3 AOD spectra have much less
1106 crossover allowing for the computation of more accurate Ångström exponents than in the Version 2 data set.

1107 **4.2 Level 1.5 Near Real-time Aerosol Optical Depth Bias and Uncertainty**

1108 The Version 3 near real-time data set provides improved data quality compared to Version 2 since the algorithm has
1109 improved cloud screening and instrument quality controls applied to the data. The data set can vary in the near real-
1110 time interval from current day up to one month as ancillary data sets are received and processed, hence, these
1111 database changes invoke reprocessing of the AOD throughout the near real-time phase. Once AOD data have been
1112 pre-field and post-field calibrated, then these data may be raised to Level 2.0 as described in Sect. 4. The near real-
1113 time data using only constant pre-field calibration is compared to the quality assured data set that uses both the pre-
1114 field and post-field calibrations applied to the data with the assumption of linear interpolation. [Figure 19](#)~~Figure 19~~
1115 shows the distribution by wavelength for this comparison of the near real-time and quality assured data set for the
1116 entire database of Level 2.0 qualified data excluding calibration site data and deployments using a copied pre-field
1117 or post-field calibration. These results are based on the Version 3 Level 2.0 data set in which the Level 1.5
1118 algorithm scans the entire deployment. The AOD difference histograms were computed for optical air mass ranges
1119 ($1.0 \leq m < 7.0$ and $1.0 \leq m < 1.5$). The optical air mass $1.0 \leq m < 7.0$ range includes all of the data; however, these AOD
1120 difference magnitudes will be constrained by the improved AOD measurements at large optical air mass and
1121 influenced toward Northern hemisphere winter mid-latitude sites when AOD tends to be low. The optical air mass
1122 $1.0 \leq m < 1.5$ range includes data will provide AOD measurements near solar noon and these measurements are
1123 generally less accurate ($\delta\tau \cdot m$) than at larger optical air mass. In addition, optical air mass $1.0 \leq m < 1.5$ range data
1124 include a greater influence of tropical locations and data from the mid-latitude summer when AOD tends to be
1125 moderate to high.

1126
1127 [Figure 19](#)~~Figure 19~~ shows the AOD average differences for the $1.0 \leq m < 7.0$ range indicate a positive bias in which
1128 the AOD for the pre-field only calibration tends to be on average $+0.003$ to $+0.009$ higher than the AOD using the
1129 interpolated calibration. Similarly, AOD average differences for the $1.0 \leq m < 1.5$ range show a positive bias and
1130 similar wavelength variations but up to two times larger differences than for the $1.0 \leq m < 7.0$ range. The largest
1131 average differences and standard deviations are for the UV wavelengths, which have greater uncertainty as
1132 discussed in Sect. 2. The AOD differences for the wavelengths longer than 500nm have about less than half the bias

1133 of the UV wavelengths. The Level 1.5 algorithm performance improves with increased data availability such as a
1134 greater number of wavelength or number of days. When an instrument deployment begins, some of the Level 1.5
1135 algorithm steps such as multi-day removal schemes are not available until several days into the deployment
1136 producing larger differences in the near real-time AOD with respect to the final product. While wavelength
1137 dependent biases of +0.003 to +0.009 for the $1.0 \leq m < 7.0$ range and +0.006 to +0.015 for the $1.0 \leq m < 1.5$ range exist
1138 when only the pre-field calibration is applied, the difference can vary significantly depending on each instrument
1139 deployment necessitating continued post-field calibration and maintenance effort.
1140

1141 When an instrument is deployed in the field, the pre-field calibration is used constantly until the post-field
1142 calibration is assessed and applied to the data using linear interpolation. The difference of pre-field calibration AOD
1143 minus the post-field calibration AOD average difference and standard deviation are computed in day bins for the
1144 number of days since the pre-field calibration. ~~Figure 20~~Figure-20 shows the AOD 500nm average difference for
1145 the optical air mass ranges: $1.0 \leq m < 7.0$ and $1.0 \leq m < 1.5$. Instruments typically operate in the field between 12 and 18
1146 months from the pre-field calibration date; however, the instrument deployment may be delayed and the instrument
1147 may not begin operation for a few months after the pre-field calibration. Thus, the number of AOD measurements
1148 in the days since pre-field calibration bins increase to a maximum at about 100 days. Some instruments may operate
1149 longer in the field to support field campaigns and other scientific priorities. ~~Figure 20~~Figure-20 shows that the AOD
1150 average difference and the standard deviation slowly but steadily increase for each optical air mass range. At about
1151 1.5 years after pre-field calibration (~550 days), the AOD average difference is about +0.010 with a standard
1152 deviation of 0.015 for optical air mass $1.0 \leq m < 7.0$ range and +0.017 with a standard deviation of 0.021 for
1153 $1.0 \leq m < 1.5$. For the UV wavelengths, the average differences and standard deviations tend to increase slightly while
1154 the longer visible and near infrared wavelengths tend to decrease slightly. Therefore, the quality of the Level 1.5
1155 near real-time AOD changes with time with high quality data at the start of the deployment but up to a +0.02 bias
1156 and 0.02 uncertainty for data collected more than 1.5 years since pre-field calibration.
1157

1158 4.3 Multi-year Monthly Comparisons of Version 3 Level 2.0 to Version 2 Level 2.0 Databases

1159 Long-term average differences between the Version 3 and Version 2 Level 2.0 data sets provide insight into the
1160 changes to be expected across most AERONET sites. The analysis of the Version 3 and Version 2 data sets shows
1161 mainly the differences in the AOD, $AE_{440-870nm}$, precipitable water (PW) in cm, and the number of days are clustered
1162 near zero (Fig. 2124). Note that precipitable water data quality depends on the quality of the input wavelengths
1163 (675nm and 870nm) and no further quality control is made on the 935nm wavelength. The increases in the Version 3
1164 Level 2.0 multi-year monthly average AOD are often due to the increased presence of fine mode particles from high
1165 aerosol loading events as well as aerosols in near cloud environments (Eck et al., 2018). The decrease in the multi-
1166 year monthly average AOD is due to the improved removal of clouds in the Version 3 quality control algorithm.
1167 Generally, the results should be very similar between Version 3 and Version 2 in AOD calculation since the
1168 temperature characterizations as well as NO₂ absorption contributions typically have relatively minor contributions.

Formatted: Font:

1169
1170 Other factors affecting the AOD calculation include the adjustment of site coordinates and elevation information for
1171 about 100 AERONET sites utilizing GPS or digital elevation model. A few rare extreme coordinate adjustments of
1172 more than 25 km included Petrolina_SONDA (9.0691° S, 40.3201° W), Ilorin (8.4841° N, 4.6745° E), and
1173 Ouagadougou (12.4241° N, 1.4872° W). A large site coordinate adjustment can complicate satellite matchups for
1174 these few cases but the review of all AERONET sites showed that less than a 5 km distance adjustment and less than
1175 100-meter elevation adjustment was needed for most of these 100 suspected sites.

1176
1177 ~~Figure 22~~Figure 22 shows similar plots to Fig. ~~2121~~ except that the observations used for the multi-year monthly
1178 averages in both data sets the instantaneous observations are time matched, hence, each data set has the same
1179 number of observations and number of days. The time matched long-term average comparison provides insight into
1180 the AOD calculation differences rather than impacts due to cloud screening and instrument quality controls applied
1181 in Level 1.5. ~~Table 5~~Table 5 shows the multi-year monthly overall standard deviation and AOD maximum to
1182 minimum range is significantly reduced compared to the data set without time-matched observations. ~~Figure~~
1183 ~~22~~Figure 22a shows a slight decreasing trend of Version 3 AOD for increasing Version 2 AOD and most of the
1184 larger AOD deviations are for sites in Asia where the impact of the OMI NO2 corrections may be contributing to the
1185 slight shift of up to 0.02 for a few months and sites.

1186
1187 For unmatched or time matched data sets in ~~Table 5~~Table 5, the precipitable water climatology changed on average
1188 insignificantly. The multi-year monthly overall days difference (~~Table 5~~Table 5) for the unmatched precipitable
1189 water data set was near zero and the standard deviation was near 25 days while the maximum of +150 and minimum
1190 of -130 days indicate significant variability due to the differences in quality controls between the algorithms.
1191 Overall, the changes from Version 2 to Version 3 in precipitable water are generally negligible in terms of the
1192 contribution to the calculation of the AOD.

1193
1194 Overall, the multi-year monthly overall average difference between Version 3 and Version 2 for unmatched data is
1195 +0.002 and time matched data is -0.002 indicating remarkable consistency between the long-term average quality
1196 assured data sets. For example, the NASA GSFC AERONET site multi-year monthly average (Fig. ~~2323~~) located
1197 20 km north of Washington, D.C., shows minor variations in the AOD and increase in AE due to removal of cirrus
1198 clouds during the winter months and increasing AOD in the summer months due to the greater abundance of cloud
1199 processed or near cloud aerosols (Eck et al., 2014).

1200
1201 Comparison of $AE_{440-870nm}$ in Fig. ~~2121b~~ and Fig. ~~2222b~~ show significantly lower values for Version 3 than Version
1202 2 Level 2.0 at low optical depth. An analysis of long-term average data at Lulin, Taiwan (23.47° N, 120.87° E)
1203 identified significant reduction of Version 3 AE relative to Version 2 AE at very low AOD due to temperature
1204 characterization that resulted in improved AOD spectral dependence (Fig. ~~2424~~). The Lulin site is a high altitude
1205 mountain station located in south central Taiwan, and this site is affected episodically by trans-boundary aerosol

Formatted: Font:

Formatted: Font:

Formatted: Font:

Formatted: Font:

Formatted: Font:

1206 plumes from East and Southeast Asia (Lin et al., 2013; Wang et al., 2013). In eastern China, multi-year monthly
1207 averages from the XiangHe site (39.75° N, 116.96° E) show a significant Version 3 AOD increase of 0.2, while
1208 maintaining nearly the same AE and increasing the number of days up to near 40% for the multi-year monthly
1209 average in July and August (Fig. 2525). The XiangHe site is located to the east of Beijing and is routinely impacted
1210 by urban pollution and episodically by biomass burning and desert dust events (Li et al., 2007). The significant
1211 increase in the AOD for XiangHe is likely due to the retention of highly variable fine mode aerosol events
1212 particularly at very high AOD, which were removed by the Version 2 cloud screening wavelengths utilizing large
1213 triplets less than 675nm (Eck et al., 2018). Additionally, some very high AOD events at XiangHe were previously
1214 removed by the Version 2 mid-visible low signal threshold but are now retained in Version 3, but often only for
1215 wavelengths longer than 675nm, so the statistics for these days are not accounted for in the 500nm data shown in
1216 Fig. 2525.

Formatted: Font:

Formatted: Font:

1217
1218 At the Mongu (15.25° S, 23.15° E) site (Fig. 26), the biomass burning smoke typically occurs during the dry season
1219 from April through November due to biomass fuel cooking and agricultural burning (Eck et al., 2003). Comparisons
1220 of multi-year monthly averages for the Mongu site shows small deviations for AOD up to ± 0.01 with slight
1221 increases in Version 3 AE during December through March due to enhanced cirrus cloud removal from the solar
1222 aureole check. Notably, the number of days for the Mongu multi-year monthly averages significantly decreased by
1223 10% to 25% in Version 3 due to improved cloud screening and sensor head temperature anomalies affecting
1224 instrument performance. In Cinzana, Mali (Fig. 27), the aerosol loading is dominated by background dust aerosol
1225 with episodic contributions to the aerosol loading from biomass burning smoke from November to March (Cavalieri
1226 et al., 2010). The AERONET IER-Cinzana site (13.28° N, 5.93° W) multi-year monthly averages show generally
1227 0.03 lower AOD for Version 3 than Version 2 and nearly the same AE for both versions. The number of days for
1228 each month is 7% to 25% lower in Version 3 when compared to Version 2 mainly due to improved cirrus cloud
1229 screening.

1230 5 Summary

1231
1232 The Aerosol Robotic Network (AERONET) has adopted a new automated quality assurance algorithm called
1233 Version 3. The significant impacts of the Version 3 algorithm are updated and improved cloud screening and
1234 quality control methods, which are powerful tools in quality assuring the Sun photometer AOD data. Comparisons
1235 between the quality assured data sets of Version 3 and Version 2 show excellent agreement. Deviations can be
1236 explained by known algorithm differences such as changes in the cloud screening triplet variability, cirrus cloud
1237 detection and removal, implementation of temperature characterization, updates to NO₂ climatology, modification of
1238 site coordinates and elevation, and identification of instrument anomalies such as aerosol optical depth (AOD)
1239 diurnal dependence, AOD spectral dependence, and instrument electrical and temperature stability.

1240
1241 Major highlights of this work include (not listed in priority):

- 1242 1. An automatic quality control algorithm significantly reduces the necessity of analysts to inspect millions of
1243 AERONET measurements. The AERONET Version 3 algorithm applied in near real-time provides high
1244 quality AOD for data assimilation applications. The Version 3 Level 2.0 data is provided within 30 days of
1245 the post-field calibration evaluation after the instrument deployment, improving the timeliness of quality
1246 assured data.
- 1247 2. Improvements to the total AERONET database cloud screening results in about 60% removal of clouds
1248 from the complete Sun photometer database and this value is similar to the coverage of clouds globally of
1249 about 68% (Rossow and Schiffer 1999). Autonomous Cimel Sun photometers can view gaps and nearby
1250 regions of the clouds and become inactive during rain periods due to wet sensor activation and AERONET
1251 sites are dominated by land locations which generally have lower cloud cover on average; therefore, these
1252 factors would reduce the difference between total AERONET cloud removal percentage and global satellite
1253 observations. Over 36% of the total data were removed by the 4-quadrant solar tracker sensitivity check
1254 due to less accuracy in tracking the Sun in cloudy conditions, while about 23% of the removal was due to
1255 the variability of clouds with respect to more homogeneous aerosol loading.
- 1256 3. Utilizing the shape of the solar aureole radiances with scattering angle, a cirrus detection algorithm was
1257 developed by leveraging MPLNET LIDAR cloud detection capabilities. The solar aureole cirrus algorithm
1258 eliminates ~5% of the Level 1.0 AOD data to reduce the bias of optically thin cirrus clouds in AERONET
1259 database.
- 1260 4. Spectral temperature correction has been implemented for all AERONET instruments using the sensor head
1261 temperature sensor reading. The temperature characterization shows significant AOD deviation ± 0.01
1262 variation between -25°C and $+50^{\circ}\text{C}$ for the Silicon 1020nm, since this wavelength is on the edge of the
1263 Silicon detector sensitivity range. Other wavelengths in the 440nm to 1640nm range have weak
1264 temperature dependence from -25°C and $+30^{\circ}\text{C}$ with a few wavelengths having greater temperature
1265 dependence at higher temperatures.
- 1266 5. New automated instrument anomaly screening provides a systematic and objective scheme to remove entire
1267 measurements or individual wavelengths from the AERONET AOD database. Importantly, obstructions to
1268 the instrument optics are now removed automatically using an AOD diurnal dependence algorithm based
1269 on the optical air mass. The AOD diurnal dependence technique employs several conditions that were
1270 developed to mitigate the removal of true diurnal dependence conditions while maximizing the removal of
1271 data significantly impacted by anomalies affecting the instrument optics.
- 1272 6. Bias and uncertainty estimates for near real-time AOD are computed by using the difference of the pre-
1273 field calibration AOD minus the interpolated calibration AOD. The near-real time AERONET data have
1274 an estimated bias up to $+0.02$ and one-sigma uncertainty up to 0.02 ; these values have slightly higher
1275 uncertainty for shorter wavelengths and slightly lower uncertainty for longer wavelengths.
- 1276 7. The AERONET Version 3 and Version 2 AOD quality controlled databases are analyzed to have a long-
1277 term monthly average difference of $+0.002$ with ± 0.02 standard deviation and greater agreement for time-
1278 matched observations with average difference of -0.002 with ± 0.004 standard deviation. The high

1279 statistical agreement in multi-year monthly averaged AOD validates the advanced automatic data quality
1280 control algorithms and suggests that migrating research to the Version 3 database will corroborate most
1281 Version 2 research results and likely lead to some more accurate results.

1282 8. Examination of long-term sites in various aerosol source regions indicates mainly subtle changes in AOD,
1283 AE and the number of days available; however, in some months, improved cloud screening, high aerosol
1284 loading retention, and improved instrument anomaly screening not attained by Version 2 explain larger
1285 deviations in these parameters.

1286
1287 AERONET Version 3 has evolved into a database with unparalleled presence in Sun photometry. Future algorithms
1288 could include improvements to the detection of cirrus clouds in polar environments, where the ice crystal size is
1289 approaching the size of large non-cloud aerosols, the determination of anomalies in high aerosol loading conditions,
1290 and the identification of true AOD diurnal dependence versus one generated by an instrument anomaly. Cimel
1291 radiometers will also measure the moon to derive lunar AOD (Berkoff et al., 2011; Barreto et al., 2013, 2016; Li et
1292 al., 2016). For example, current lunar measurement protocols do not include lunar aureole measurements analogous
1293 to the solar aureole measurements, hence the lack of these measurements potentially reduces the ability of the
1294 algorithm to remove cirrus clouds at night, and thus a variation of the quality control methodology may need to be
1295 developed. Other surface-based remote sensing networks such as MAN (Smirnov et al., 2009), SKYNET
1296 (Takamura and Nakajima 2004), GAW-PFR (Kazadzis et al., 2018), and PANDORA (Herman et al., 2009) may
1297 benefit by implementing applicable quality control methods established by AERONET.

1298
1299 *Data Availability.* Version 3 AOD data are available from the AERONET web site (<https://aeronet.gsfc.nasa.gov>)
1300 and the web site provides these data freely to the public. Data may be acquired by utilizing several download
1301 mechanisms including site-by-site download tools and web service options for near real-time data acquisition.

1302
1303 *Author contributions.* For five years, the AERONET staff (listed from DG to BH) worked individually and
1304 collaboratively drawing on their decades of project scientific, engineering and programming expertise to develop
1305 and assess the Version 3 AOD processing system presented herein. Traditional assignment of co-authorship is not
1306 possible. Aside from the first author, contributing AERONET staff is listed in reverse chronological order based on
1307 their start date with the project. JL, JC, and EW provided LIDAR data for development of the cirrus curvature
1308 methodology. SK and AL provided gaseous and water vapor absorption coefficients based on radiative transfer
1309 models.

1310
1311 *Competing interests:* The authors declare that they have no conflict of interest.

1312
1313 *Acknowledgements.* The AERONET and MPLNET projects at NASA GSFC are supported by the Earth Observing
1314 System Program Science Office Cal-Val, Radiation Science program at NASA headquarters, and various field
1315 campaigns. NCEP Reanalysis data are obtained routinely from the U.S. National Weather Service Climate

1316 Prediction Center. We would like to thank Edward Celarier for several discussions and providing the OMI NO₂
1317 monthly climatology. Fred Espenak and Chris O'Byrne (NASA GSFC) provided solar and lunar eclipse predictions
1318 and the Eclipse Explorer software.

1319
1320 We thank the MPLNET PIs for their effort in establishing and maintaining the sites: Arnon Karnieli
1321 (SEDE_BOKER); Sachi Tripathi (Kanpur); Greg Schuster (COVE); Margarita Yela Gonzalez (Santa Cruz
1322 Tenerife); and John Barnes (Trinidad Head).

1323
1324 The authors thank the AERONET calibration facilities in the USA (NASA GSFC, NOAA Mauna Loa Observatory,
1325 and NEON), France (PHOTONS), and Spain (RIMA and Izana). We thank the following AERONET PIs and their
1326 staff for maintaining the sites and contributing aerosol data: Norm O'Neill, Ihab Abboud and Vitali Fioletov
1327 (PEARL, Toronto, Bratts Lake); Itaru Sano (Osaka); Paulo Artaxo (Rio Branco); Neng-Huei Lin (Lulin); Pucai
1328 Wang and Xiangao Xia (XiangHe); Mikhail Panchenko (Ussurisyk); Arnon Karnieli (SEDE BOKER); Emilio
1329 Cuevas-Agullo (Santa Cruz Tenerife); Joseph Prospero (Ragged Point); Soo-Chin Liew and Santo Salinas Cortijo
1330 (Singapore); S. N. Tripathi (Kanpur); Francisco Reyes (Malaga); and Jean Rajot and Beatrice Marticorena (IER-
1331 Cinzana). A special acknowledgement is given to the AERONET principal investigators and their site staff around
1332 the world who participate in monitoring aerosols to expand our scientific understanding of the Earth.

1333 **References**

- 1334 [Alexandrov, M. D., Schmid, B., Turner, D. D., Cairns, B., Oinas, V., Lacis, A. A., Gutman, S. I., Westwater, E. R.,](#)
1335 [Smirnov, A., and Eilers, J.: Columnar water vapor from multifilter rotating shadowband radiometer data, J.](#)
1336 [Geophys. Res., 114, D02306, <https://doi.org/10.1029/2008JD010543>, 2009.](#)
- 1337 Andrews, E., Ogren, J. A., Kinne, S., and Samset, B.: Comparison of AOD, AAOD and column single scattering
1338 albedo from AERONET retrievals and in situ profiling measurements, *Atmos. Chem. Phys.*, 17, 6041-
1339 6072, <https://doi.org/10.5194/acp-17-6041-2017>.
- 1340 Ångström, A.: Apparent solar constant variations and their relation to variability of atmospheric transmission,
1341 *Tellus*, 22, 205-218, <https://doi.org/10.3402/tellusa.v22i2.10215>, 1970.
- 1342 [Arola, A. and Koskela T.: On the sources of bias in aerosol optical depth retrieval in the UV range. J. Geophys. Res.,](#)
1343 [109, D08209, <https://doi.org/10.1029/2003JD004375>, 2004.](#)
- 1344 [Barreto, A., Cuevas, E., Damiri, B., Guirado, C., Berkoff, T., Berjón, A. J., Hernández, Y., Almansa, F., and Gil,](#)
1345 [M.: A new method for nocturnal aerosol measurements with a lunar photometer prototype, Atmos. Meas.](#)
1346 [Tech., 6, 585-598, <https://doi.org/10.5194/amt-6-585-2013>, 2013.](#)
- 1347 [Barreto, Á., Cuevas, E., Granados-Muñoz, M.-J., Alados-Arboledas, L., Romero, P. M., Gröbner, J., Kouremeti, N.,](#)
1348 [Almansa, A. F., Stone, T., Toledano, C., Román, R., Sorokin, M., Holben, B., Canini, M., and Yela, M.:](#)
1349 [The new sun-sky-lunar Cimel CE318-T multiband photometer – a comprehensive performance evaluation,](#)
1350 [Atmos. Meas. Tech., 9, 631-654, <https://doi.org/10.5194/amt-9-631-2016>, 2016.](#)
- 1351 Berkoff, T.A., Sorokin, M., Stone, T., Eck, T.F., Hoff, R., Welton, E., and Holben, B.: Nocturnal Aerosol Optical
1352 Depth Measurements with a Small-Aperture Automated Photometer Using the Moon as a Light Source. *J.*
1353 *Atmos. Ocean. Tech.*, 28, 1297–1306, <https://doi.org/10.1175/JTECH-D-10-05036.1>, 2011.
- 1354 [Bock, O., Bosser, P., Bourcy, T., David, L., Goutail, F., Hoareau, C., Keckhut, P., Legain, D., Pazmino, A., Pelon,](#)
1355 [J., Pipis, K., Pujol, G., Sarkissian, A., Thom, C., Tournois, G., and Tzanos, D.: Accuracy assessment of](#)
1356 [water vapour measurements from in situ and remote sensing techniques during the DEMEVAP 2011](#)
1357 [campaign at OHP, Atmos. Meas. Tech., 6, 2777-2802, <https://doi.org/10.5194/amt-6-2777-2013>, 2013.](#)
- 1358 Bodhaine, B. A., Wood, N. B., Dutton, E. G., Slusser, J. R.: On Rayleigh Optical Depth Calculations, *J. Atmos.*
1359 *Ocean. Tech.*, 16, 1854-1861, [https://doi.org/10.1175/1520-0426\(1999\)016%3C1854:ORODC%3E2.0.CO;2](https://doi.org/10.1175/1520-0426(1999)016%3C1854:ORODC%3E2.0.CO;2), 1999.
- 1360
- 1361 Boersma, K. F., H. J. Eskes, and E. J. Brinksma: Error analysis for tropospheric NO₂ retrieval from space, *J.*
1362 *Geophys. Res.*, 109, D04311, <https://doi.org/10.1029/2003JD003962>, 2004.
- 1363 Boersma, K. F., Jacob, D. J., Eskes, H. J., Pinder, R. W., Wang, J., and van der A, R. J.: Intercomparison of
1364 SCIAMACHY and OMI tropospheric NO₂ columns: Observing the diurnal evolution of chemistry and
1365 emissions from space, *J. Geophys. Res.*, 113, D16S26, <https://doi.org/10.1029/2007JD008816>, 2008.
- 1366 [Bokoye, A. I., Royer, A., O'Neill, N. T., Cliche, P., Fedosejevs, G.,Teillet, P. M., and McArthur, L. J. B.:](#)
1367 [Characterization of atmospheric aerosols across Canada from a ground-based sunphotometer network:](#)
1368 [AEROCAN, Atmosphere-Ocean, 39:4, 429-456.: <https://doi.org/10.1080/07055900.2001.9649687>, 2001.](#)

Formatted: Default Paragraph Font

Formatted: Default Paragraph Font

1369 [Bokoye, A. I., Rover, A., O'Neill, N. T., Cliché, P., McArthur, L. J. B., Teillet, P. M., Fedosejevs, G., and Thériault,](#)
1370 [J.-M.: Multisensor analysis of integrated atmospheric water vapor over Canada and Alaska, *J. Geophys.*](#)
1371 [Res., 108, 4480, doi: 10.1029/2002JD002721, D15, 2003.](#)

1372 Bruegge, C. J., Conel, J. E., Green, R. O., Margolis, J. S., Holm, R. G., and Toon, G.: Water vapor column
1373 abundance retrievals during FIFE, *J. Geophys. Res.*, 97(D17), 18759–18768,
1374 <https://doi.org/10.1029/92JD01050>, 1992.

1375 Burrows, J. P., Dehn, A., Deters, B., Himmelmann, S., Richter, A., Voigt, S. and Orphal, J.: Atmospheric Remote-
1376 Sensing Reference Data from GOME: Part 1. Temperature-Dependent Absorption Cross-sections of NO₂
1377 in the 231-794 nm Range, *JQSRT*, 60, 1025–1031, [https://doi.org/10.1016/S0022-4073\(97\)00197-0](https://doi.org/10.1016/S0022-4073(97)00197-0), 1998.

1378 Burrows, J. P., Richter, A., Dehn, A., Deters, B., Himmelmann, S., Voigt, S. and Orphal J.: Atmospheric remote-
1379 sensing reference data from GOME – 2. Temperature-dependent absorption cross sections of O₃ in the 231-
1380 794 nm range, *J. Quant. Spectrosc. Ra.*, 61, 509–517, [https://doi.org/10.1016/S0022-4073\(98\)00037-5](https://doi.org/10.1016/S0022-4073(98)00037-5),
1381 1999.

1382 Cachorro, V. E., Romero, P. M., Toledano, C., Cuevas, E., and de Frutos, A. M.: The fictitious diurnal cycle of
1383 aerosol optical depth: A new approach for “in situ” calibration and correction of AOD data series,
1384 *Geophys. Res. Lett.*, 31, L12106, <https://doi.org/10.1029/2004GL019651>, 2004.

1385 Campbell, J.R., Hlavka, D. L., Welton, E. J., Flynn, C. J., Turner, D. D., Spinhirne, J. D., Scott, V.S., and Hwang,
1386 I.H.: Full-time, Eye-Safe Cloud and Aerosol Lidar Observation at Atmospheric Radiation Measurement
1387 Program Sites: Instrument and Data Processing, *J. Atmos. Ocean. Tech.*, 19, 431-442,
1388 [https://doi.org/10.1175/1520-0426\(2002\)019%3C0431:FTESCA%3E2.0.CO;2](https://doi.org/10.1175/1520-0426(2002)019%3C0431:FTESCA%3E2.0.CO;2), 2002.

1389 Campbell, J. R., Vaughan, M. A., Oo, M., Holz, R. E., Lewis, J. R., and Welton, E. J.: Distinguishing cirrus cloud
1390 presence in autonomous lidar measurements, *Atmos. Meas. Tech.*, 8, 435–449, [https://doi.org/10.5194/amt-](https://doi.org/10.5194/amt-8-435-2015)
1391 [8-435-2015](https://doi.org/10.5194/amt-8-435-2015), 2015.

1392 [Campanelli, M., Mascitelli, A., Sanò, P., Diémoz, H., Estellés, V., Federico, S., Iannarelli, A. M., Fratarcangeli, F.,](#)
1393 [Mazzoni, A., Realini, E., Crespi, M., Bock, O., Martínez-Lozano, J. A., and Dietrich, S.: Precipitable water](#)
1394 [vapour content from ESR/SKYNET sun–sky radiometers: validation against GNSS/GPS and AERONET](#)
1395 [over three different sites in Europe, *Atmos. Meas. Tech.*, 11, 81-94, https://doi.org/10.5194/amt-11-81-](#)
1396 [2018, 2018.](#)

1397 Cavalieri, O., Cairo, F., Fierli, F., Di Donfrancesco, G., Snels, M., Viterbini, M., Cardillo, F., Chatenet, B.,
1398 Formenti, P., Marticorena, B., and Rajot, J. L.: Variability of aerosol vertical distribution in the Sahel,
1399 *Atmos. Chem. Phys.*, 10, 12005–12023, <https://doi.org/10.5194/acp-10-12005-2010>, 2010.

1400 [Che, H., Zhang, X.-Y., Xia, X., Goloub, P., Holben, B., Zhao, H., Wang, Y., Zhang, X.-C., Wang, H., Blarel, L.,](#)
1401 [Damiri, B., Zhang, R., Deng, X., Ma, Y., Wang, T., Geng, F., Qi, B., Zhu, J., Yu, J., Chen, Q., and Shi, G.:](#)
1402 [Ground-based aerosol climatology of China: aerosol optical depths from the China Aerosol Remote](#)
1403 [Sensing Network \(CARSNET\) 2002–2013, *Atmos. Chem. Phys.*, 15, 7619-7652,](#)
1404 <https://doi.org/10.5194/acp-15-7619-2015>, 2015.

1405 Chew, B. N., Campbell, J. R., Reid, J. S., Giles, D. M., Welton, E. J., Salinas, S. V., and Liew, S. C.: Tropical cirrus
1406 cloud contamination in sun photometer data, *Atmos. Environ.*, 45, 6724–6731,
1407 <https://doi.org/10.1016/j.atmosenv.2011.08.017>, 2011.

1408 Clough, S. A., F. X. Kneizys, and R. W. Davies: Line shape and the water vapor continuum, *Atmos. Res.*, 23, 229–
1409 241, [https://doi.org/10.1016/0169-8095\(89\)90020-3](https://doi.org/10.1016/0169-8095(89)90020-3), 1989.

1410 Coddington, Lean, O., J., Pilewskie, P., Snow, M., and Lindholm, D.: A solar irradiance climate data record, *Bull.*
1411 *Amer. Meteor. Soc.*, <https://doi.org/10.1175/BAMS-D-14-00265.1>, 2016.

1412 DeVore, J.G., Stair, A.T., LePage, A., Rall, D., Atkinson, J., Villanucci, D., Rappaport, S.A., Joss, P.C., and
1413 McClatchey, R.A.: Retrieving Properties of Thin Clouds from Solar Aureole Measurements. *J. Atmos.*
1414 *Oceanic Technol.*, 26, 2531–2548, <https://doi.org/10.1175/2009JTECHA1289.1>, 2009.

1415 DeVore, J. G., Stair Jr., A. T., LePage, A. J., and Villanucci, D.: Using scattering calculations to compare MODIS
1416 retrievals of thin cirrus optical properties with SAM solar disk and aureole radiance measurements, *J.*
1417 *Geophys. Res.*, 117, D01204, <https://doi.org/10.1029/2011JD015858>, 2012.

1418 Dubovik, O. V, Lapyonok, T. V. and Oshchepkov, S. L.: Improved technique for data inversion: optical sizing of
1419 multicomponent aerosols, *Appl.Opt.*, 34, 8422–8436, <https://doi.org/10.1364/AO.34.008422>, 1995.

1420 Dubovik, O. and King, M. D.: A flexible inversion algorithm for retrieval of aerosol optical properties from Sun and
1421 sky radiance measurements, *J. Geophys. Res.*, 105, 20 673–20 696, <https://doi.org/10.1029/2000JD900282>,
1422 2000.

1423 Eck, T. F., Holben, B. N., Reid, J. S., Dubovik, O., Smirnov, A., O'Neill, N. T., Slutsker, I., and Kinne, S.:
1424 Wavelength dependence of the optical depth of biomass burning, urban, and desert dust aerosols, *J.*
1425 *Geophys. Res.*, 104(D24), 31333–31349, <https://doi.org/10.1029/1999JD900923>, 1999.

1426 Eck, T. F., Holben, B. N., Reid, J. S., Arola, A., Ferrare, R. A., Hostetler, C. A., Crumeyrolle, S. N., Berkoff, T. A.,
1427 Welton, E. J., Lolli, S., Lyapustin, A., Wang, Y., Schafer, J. S., Giles, D. M., Anderson, B. E., Thornhill, K.
1428 L., Minnis, P., Pickering, K. E., Loughner, C. P., Smirnov, A., and Sinyuk, A.: Observations of rapid
1429 aerosol optical depth enhancements in the vicinity of polluted cumulus clouds, *Atmos. Chem. Phys.*, 14,
1430 11633–11656, doi: 10.5194/acp-14-11633-2014, 2014.

1431 Eck, T. F., Holben, B. N., Reid, J. S., Xian, P., Giles, D. M., Sinyuk, A., Smirnov, A., Schafer, J. S., Slutsker, I.,
1432 Kim, J., Koo, J.-H., Choi, M., Kim, K. C., Sano, I., Arola, A., Sayer, A. M., Levy, R. C., Munchak, L. A.,
1433 O'Neill, N. T., Lyapustin, A., Hsu, N. C., Randles, C. A., Da Silva, A. M., Buchard, V., Govindaraju, R.
1434 C., Hyer E., Crawford, J. H., Wang, P., and Xia, X.: Observations of the interaction and transport of fine
1435 mode aerosols with cloud and/or fog in Northeast Asia from Aerosol Robotic Network and satellite remote
1436 sensing, *J. Geophys. Res. Atmos.*, 123, 5560–5587. <https://doi.org/10.1029/2018JD028313>, 2018.

1437 Eiden R.: Calculations and measurements of the spectral radiance of the solar aureole, *Tellus*, 20:3, 380–399, doi:
1438 10.3402/tellusa.v20i3.10017, 1968.

1439 Espenak, F., and Meeus, J.: Five Millennium Cannon of Solar Eclipses: –1999 to +3000 (2000 BCE to 3000 CE),
1440 NASA Technical Publication TP-2006-214141, NASA, Greenbelt, MD, 2006.

1441 Gamache, R. R., Roller, C., Lopes, E., Gordon, I. E., Rothman, L. S., Polyansky, O. L., Zobov, N. F., Kyuberis, A.
1442 A., Tennyson, J., Yurchenko, S. N., Csaszar, A. G., Furtenbacher, T., Huang, X., Schwenke, D. W., Lee, T.
1443 J., Drouin, B. J., Tashkun, S. A., Perevalov, V. I., Kochanov, R. V.: Total internal partition sums for 166
1444 isotopologues of 51 molecules important in planetary atmospheres: Application to HITRAN2016 and
1445 beyond, *J. Quant. Spectrosc. Ra.*, <https://doi.org/10.1016/j.jqsrt.2017.03.045>, 2017.

1446 Giles, D. M., Holben, B. N., Eck, T. F., Sinyuk, A., Smirnov, A., Slutsker, I., Dickerson, R. R., Thompson, A. M.,
1447 and Schafer, J. S.: An analysis of AERONET aerosol absorption properties and classifications
1448 representative of aerosol source regions, *J. Geophys. Res.*, 117, D17203,
1449 <https://doi.org/10.1029/2012JD018127>, 2012.

1450 [Goloub, P., Li, Z., Dubovik, O., Blarel, L., Podvin, T., Jankowiak, I., Lecoq, R., Deroo, C., Chatenet, B., Morel, J.](#)
1451 [P., Cuevas, E., and Ramos, R.: PHOTONS/AERONET sunphotometer network overview: description,](#)
1452 [activities, results, *Proc. SPIE*, 6936, 69360V, <https://doi.org/10.1117/12.783171>, 2008.](#)

1453 Haapanala, P., Räisänen, P., McFarquhar, G. M., Tiira, J., Macke, A., Kahnert, M., Nousiainen, T.: Disk and
1454 circumsolar radiances in the presence of ice clouds, *Atmos. Chem. Phys.*, 17(11), 6865–6882, doi:
1455 <https://dx.doi.org/10.5194/acp-17-6865-2017>, 2017.

1456 Halthore, R. N., Eck, T. F., Holben, B. N., and Markham, B. L.: Sun photometric measurements of atmospheric
1457 water vapor column abundance in the 940-nm band, *J. Geophys. Res.*, 102(D4), 4343–4352,
1458 <https://doi.org/10.1029/96JD03247>, 1997.

1459 Hamonou, Chazette, E., P., Balis, D., Dulac, F., Schneider, X., Galani, E., Ancellet, G., and Papayannis, A.:
1460 Characterization of the vertical structure of Saharan dust export to the Mediterranean basin, *J. Geophys.*
1461 *Res.*, 104(D18), 22257–22270, <https://doi.org/10.1029/1999JD900257>, 1999.

1462 Herman, J., Cede, A., Spinei, E., Mount, G., Tzortziou, M., and Abuhassan, N.: NO₂ column amounts from ground-
1463 based Pandora and MFDOAS spectrometers using the direct-sun DOAS technique: Intercomparisons and
1464 application to OMI validation, *J. Geophys. Res.*, 114, D13307, <https://doi.org/10.1029/2009JD011848>,
1465 2009.

1466 Holben, B. N., Vermote, E., Kaufman, Y. J., Tanre, D. and Kalb, V.: Aerosol retrieval over land from AVHRR data-
1467 application for atmospheric correction, *IEEE T. Geosci. Remote*, 30, 212–222,
1468 <https://doi.org/10.1109/36.134072>, 1992.

1469 Holben, B. N., Eck, T. F., Slutsker, I., Tanre, D., Buis, J. P., Setzer, A., Vermote, E., Reagan, J. A., Kaufman, Y.,
1470 Nakajima, T., Lavenue, F., Jankowiak, I., and Smirnov, A.: AERONET—A federated instrument network
1471 and data archive for aerosol characterization, *Remote Sens. Environ.*, 66, 1–16,
1472 [https://doi.org/10.1016/S0034-4257\(98\)00031-5](https://doi.org/10.1016/S0034-4257(98)00031-5), 1998.

1473 Holben, B. N., Tanre, D., Smirnov, A., Eck, T. F., Slutsker, I., Abuhassan, N., Newcomb, W. W., Schafer, J.,
1474 Chatenet, B., Lavenue, F., Kaufman, Y., Vande Castle, J., Setzer, A., Markham, B., Clark, D., Frouin, R.,
1475 Halthore, R., Karnieli, A., O'Neill, N. T., Pietras, C., Pinker, R. T., Voss, K. and Zibordi, G.: An emerging
1476 ground-based aerosol climatology: Aerosol optical depth from AERONET, *J. Geophys. Res.*, 106(D11),
1477 12,067–12,097, <https://doi.org/10.1029/2001JD900014>, 2001.

1478 Holben, B. N., Eck, T. F., Slutsker, I., Smirnov, A., Sinyuk, A., Schafer, J., Giles, D., and Dubovik, O.: Aeronet's
1479 Version 2.0 quality assurance criteria, Proc. SPIE, 6408, Conf. on Remote Sensing of the Atmosphere and
1480 Clouds, 64080Q, <https://doi.org/10.1117/12.706524>, 2006.

1481 Huang, J., Hsu, N., Tsay, S.-C., Jeong, M.-J., Holben, B. N., Berkoff, T. A., and Welton, E. J.: Susceptibility of
1482 aerosol optical thickness retrievals to thin cirrus contamination during the BASE-ASIA campaign, J.
1483 Geophys. Res., 116, D08214, <https://doi.org/10.1029/2010JD014910>, 2011.

1484 Ingold, T., Schmid, B., Mätzler, C., Demoulin, P., and Kämpfer, N.: Modeled and empirical approaches for
1485 retrieving columnar water vapor from solar transmittance measurements in the 0.72, 0.82 and 0.94-mm
1486 absorption bands, J. Geophys. Res., 105, 24,327–24,343, <https://doi.org/10.1029/2000JD900392>, 2000.

1487 Kahn, R. A., and Gaitley, B. J.: An analysis of global aerosol type as retrieved by MISR, J. Geophys. Res. Atmos.,
1488 120, 4248–4281, <https://doi.org/10.1002/2015JD023322>, 2015.

1489 Kasten, F.: A new table and approximation formula for relative optical air mass, Arch. Meteorol. Geophys.
1490 Bioklimatol. Ser. B, 14, 206–223, <https://doi.org/10.1007/BF02248840>, 1965.

1491 Kasten, F. and Young, A. T.: Revised optical air mass tables and approximation formula, Appl. Opt., 28, 4735–
1492 4738, <https://doi.org/10.1364/AO.28.004735>, 1989.

1493 Kalnay, E., Kanamitsu, M., Kistler, R., Collins, W., Deaven, D., Gandin, L., Iredell, M., Saha, S., White, G.,
1494 Woollen, J., Zhu, Y., Chelliah, M., Ebisuzaki, W., Higgins, W., Janowiak, J., Mo, K. C., Ropelewski, C.,
1495 Wang, J., Leetmaa, A., Reynolds, R., Jenne, R. and Joseph, D.: The NCEP/NCAR 40-Year Reanalysis
1496 Project, Bull. Amer. Meteor. Soc., 77, 437–471, [https://doi.org/10.1175/1520-0477\(1996\)077%3C0437:TNYRP%3E2.0.CO;2](https://doi.org/10.1175/1520-0477(1996)077%3C0437:TNYRP%3E2.0.CO;2), 1996.

1497 [Kaufman, Y. J., and Tanré, D.: Strategy for direct and indirect methods for correcting the aerosol effect on remote](#)
1498 [sensing: From AVHRR to EOS-MODIS, Rem. Sens. Environ., 55, 1, 65–79, \[https://doi.org/10.1016/0034-\]\(https://doi.org/10.1016/0034-4257\(95\)00193-X\)](#)
1499 [4257\(95\)00193-X, 1996.](#)

1500 Kaufman, Y. J., Remer, L. A., Tanre, D., Li, R.-R., Kleidman, R., Mattoo, S., Levy, R. C., Eck, T. F., Holben, B. N.,
1501 Ichoku, C., Martins, J. V., and Koren, I.: A Critical Examination of the Residual Cloud Contamination and
1502 Diurnal Sampling Effects on MODS Estimates of Aerosol Over Ocean, IEEE T. Geosci. Remote, 43,
1503 <https://doi.org/10.1109/TGRS.2005.858430>, 2005.

1504 [Kazadzis, S., Kouremeti, N., Nyeki, S., Gröbner, J., and Wehrli, C.: The World Optical Depth Research and](#)
1505 [Calibration Center \(WORCC\) quality assurance and quality control of GAW-PFR AOD measurements,](#)
1506 [Geosci. Instrum. Method. Data Syst., 7, 39-53, <https://doi.org/10.5194/gi-7-39-2018>, 2018.](#)

1507 Kinne, S., Akerman, T. P., Shiobara, M., Uchiyama, A., Heymsfield, A. J., Miloshevich, L., Wendell, J., Eloranta,
1508 E., Purgold, C., and Bergstrom, R. W.: Cirrus cloud radiative and microphysical properties from ground
1509 observations and in situ measurements during FIRE 1991 and their application to exhibit problems in cirrus
1510 solar radiative transfer modeling, J. Atmos. Sci., 54, 2320–2344, [https://doi.org/10.1175/1520-0469\(1997\)054%3C2320:CCRAMP%3E2.0.CO;2](https://doi.org/10.1175/1520-0469(1997)054%3C2320:CCRAMP%3E2.0.CO;2), 1997

1511 Kline, Morris: Calculus: An Intuitive and Physical Approach, Dover. 457–461, ISBN 978-0-486-40453-0, 1998.

1514 Komhyr, W. D., Grass, K. D., and Leonard, R. K.: Dobson Spectrophotometer 83: a standard for total ozone
1515 measurements, 1962-1987, *J. Geophys. Res.*, 94, 9847–9861, <https://doi.org/10.1029/JD094iD07p09847>,
1516 1989.

1517 Levy, R. C., Remer, L. A., Kleidman, R. G., Mattoo, S., Ichoku, C., Kahn, R., and Eck, T. F.: Global evaluation of
1518 the Collection 5 MODIS dark-target aerosol products over land, *Atmos. Chem. Phys.*, 10, 10399–10420,
1519 <https://doi.org/10.5194/acp-10-10399-2010>, 2010.

1520 Levy, R. C., Mattoo, S., Munchak, L. A., Remer, L. A., Sayer, A. M., Patadia, F., and Hsu, N. C.: The Collection 6
1521 MODIS aerosol products over land and ocean, *Atmos. Meas. Tech.*, 6, 2989–3034,
1522 <https://doi.org/10.5194/amt-6-2989-2013>, 2013.

1523 Lewis, J., Campbell, J., Welton, E. J., Stewart, S. A., and Haftings, P. C.: Overview of MPLNET Version 3 Cloud
1524 Detection, *J. Atmos. Ocean Tech.*, <https://doi.org/10.1175/JTECH-D-15-0190.1>, 2016.

1525 Li, Z., Zhao, X., Kahn, R., Mishchenko, M., Remer, L., Lee, K.-H., Wang, M., Laszlo, I., Nakajima, T., and Maring,
1526 H.: Uncertainties in satellite remote sensing of aerosols and impact on monitoring its long-term trend: a
1527 review and perspective, *Ann. Geophys.*, 27, 2755–2770, <https://doi.org/10.5194/angeo-27-2755-2009>,
1528 2009.

1529 Li, Z., Xia, X., Cribb, M., Mi, W., Holben, B., Wang, P., Chen, H., Tsay S.-C., Eck, T. F., Zhao, F., Dutton, E. G.
1530 and Dickerson, R. E.: Aerosol optical properties and their radiative effects in northern China, *J. Geophys.*
1531 *Res.*, 112, D22S01, <https://doi.org/10.1029/2006JD007382>, 2007.

1532 [Li, Z., Li, K., Li, D., Yang, J., Xu, H., Goloub, P., and Victori, S.: Simple transfer calibration method for a Cimel](#)
1533 [Sun–Moon photometer: calculating lunar calibration coefficients from Sun calibration constants, *Appl. Opt.*](#)
1534 [55, 7624–7630, <https://doi.org/10.1364/AO.55.007624>, 2016.](#)

1535 Lin, N.-H., S.-C. Tsay, H. B. Maring, M.-C. Yen, G.-R. Sheu, S.-H. Wang, et al.: An overview of regional
1536 experiments on biomass burning aerosols and related pollutants in Southeast Asia: From BASE-ASIA and
1537 the Dongsha Experiment to 7-SEAS, *Atmos. Environ.*, 78, 1–19,
1538 <https://doi.org/10.1016/j.atmosenv.2013.04.066>, 2013.

1539 Martins, J. V., Tanré, D., Remer, L., Kaufman, Y., Mattoo, S., and Levy, R.: MODIS Cloud screening for remote
1540 sensing of aerosols over oceans using spatial variability, *Geophys. Res. Lett.*, 29(12),
1541 <https://doi.org/10.1029/2001GL013252>, 2002.

1542 McPeters, R. D., Frith, S., and Labow, G. J.: OMI total column ozone: extending the long-term data record, *Atmos.*
1543 *Meas. Tech.*, 8, 4845–4850, <https://doi.org/10.5194/amt-8-4845-2015>, 2015.

1544 Michalsky, J.: The astronomical almanac's algorithm for approximate solar position (1950–2030), *Solar Energy*, 40,
1545 227–235, [https://doi.org/10.1016/0038-092X\(88\)90045-X](https://doi.org/10.1016/0038-092X(88)90045-X), 1988.

1546 Michalsky, J. J., J.C. Liljegren and Harrison, L. C.: A Comparison of Sun Photometer Derivations of Total Column
1547 Water Vapor and Ozone to Standard Measures of Same at the Southern Great Plains Atmospheric
1548 Radiation Measurement Site, *J. Geophys. Res.*, 100, 25995–26003, <https://doi.org/10.1029/95JD02706>,
1549 1995.

Formatted: Default Paragraph Font

1550 [Mitchell, R. M., Forgan, B. W., and Campbell, S. K.: The Climatology of Australian Aerosol, Atmos. Chem. Phys.,](#)
1551 [17, 5131-5154, https://doi.org/10.5194/acp-17-5131-2017, 2017.](#)

1552 Mlawer, E. J., V. H. Payne, J.-L. Moncet, J. S. Delamere, M. J. Alvarado and D. D. Tobin: Development and recent
1553 evaluation of the MT_CKD model of continuum absorption, *Phil. Trans. Roy. Soc. A*, 370, 1–37,
1554 [https://doi.org/10.1098/rsta.2011.0295, 2012.](#)

1555 Nakajima, T., Tonna, G., Rao, R., Boi, P., Kaufman, Y., and Holben, B.: Use of sky brightness measurements from
1556 ground for remote sensing of particulate polydispersions, *Appl. Opt.* 35, 2672–2686,
1557 [https://doi.org/10.1364/AO.35.002672, 1996.](#)

1558 Omar, A. H., Winker, D. M., Tackett, J. L., Giles, D. M., Kar, J., Liu, Z., Vaughan, M. A., Powell, K. A., and
1559 Trepte, C. R., CALIOP and AERONET aerosol optical depth comparisons: One size fits none, *J. Geophys.*
1560 *Res. Atmos.*, 118, 4748–4766, [https://doi.org/10.1002/jgrd.50330, 2013.](#)

1561 O'Neill, N. T., Eck, T. F., Holben, B. N., Smirnov, A., Dubovik, O., and Royer, A.: Bimodal size distribution
1562 influences on the variation of Angstrom derivatives in spectral and optical depth space, *J. Geophys. Res.*,
1563 106, 9787–9806, [https://doi.org/10.1029/2000JD900245, 2001.](#)

1564 O'Neill, N. T., Eck, T. F., Smirnov, A., Holben, B. N., and Thulasiraman, S.: Spectral discrimination of coarse and
1565 fine mode optical depth, *J. Geophys. Res.*, 108, D17, 4559–4573, [https://doi.org/10.1029/2002JD002975,](#)
1566 2003.

1567 O'Neill, N. T., Eck, T. F., Reid, J. S., Smirnov, A., and Pancrati, O.: Coarse mode optical information retrievable
1568 using ultraviolet to short-wave infrared Sun photometry: Application to United Arab Emirates Unified
1569 Aerosol Experiment data, *J. Geophys. Res.*, 113, D05212, [https://doi.org/10.1029/2007JD009052, 2008.](#)

1570 [Prasad, A. K. and Singh R. P.: Validation of MODIS Terra, AIRS, NCEP/DOE AMIP-II Reanalysis-2, and](#)
1571 [AERONET Sun photometer derived integrated precipitable water vapor using ground-based GPS receivers](#)
1572 [over India. *J. Geophys. Res.*, 114, D05107, doi: 10.1029/2008JD011230, 2009.](#)

1573 [Pérez-Ramírez, D., Whiteman, D. N., Smirnov, A., Lyamani, H., Holben, B. N., Pinker, R., Andrade, M., and](#)
1574 [Alados-Arboledas, L.: Evaluation of AERONET precipitable water vapor versus microwave radiometry,](#)
1575 [GPS, and radiosondes at ARM sites, *J. Geophys. Res. Atmos.*, 119, 9596–9613,](#)
1576 [https://doi.org/10.1002/2014JD021730, 2014.](#)

1577 Redemann, J., Masonis, S. J., Schmid, B., Anderson, T. L., Russell, P. B., Livingston, J. M., Dubovik, O., and
1578 Clarke, A. D.: Clear-column closure studies of aerosols and water vapor aboard the NCAR C-130 during
1579 ACE-Asia, 2001, *J. Geophys. Res.*, 108(D23), 8655, [https://doi.org/10.1029/2003JD003442, 2003.](#)

1580 Remer, L. A., Kaufman, Y. J., Tanré, D., Mattoo, S., Chu, D. A., Martins, J. V., Li, R., Ichoku, C., Levy, R. C.,
1581 Kleidman, R. G., Eck, T. F., Vermote, E., and Holben, B. N.: The MODIS Aerosol Algorithm, Products,
1582 and Validation. *J. Atmos. Sci.*, 62, 947–973, [https://doi.org/10.1175/JAS3385.1, 2005.](#)

1583 Rossow, W. B. and Schiffer, R. A.: Advances in Understanding Clouds from ISCCP. *Bull. Amer. Meteor. Soc.*, 80,
1584 2261–2288, [https://doi.org/10.1175/1520-0477\(1999\)080<2261:AIUCFI>2.0.CO;2, 1999.](#)

1585 Russell, P. B., Livingston, J. M., Dutton, E. G., Pueschel, R. F., Reagen, J. A., DeFoor, T. E., Box, M. A., Allen, D.,
1586 Pilewskie, P., Herman, B. M., Kinne, S. A. and Hoffman, D. J.: Pinatubo and pre-Pinatubo optical-depth

1587 spectra: Mauna Loa measurements, comparisons, inferred particle size distributions, radiative effects, and
1588 relationship to lidar data, *J. Geophys. Res.*, 98(D12), 22969–22985, <https://doi.org/10.1029/93JD02308>,
1589 1993.

1590 [Sakerin S.M., Kabanov D.M., Panchenko M.V., Pol'kin V.V., Holben B.N., Smirnov A.V., Beresnev S.A., Gorda](#)
1591 [S.Yu., Kornienko G.I., Nikolashkin S.V., Poddubnyi V.A., Tashchilin M.A.: Monitoring of atmospheric](#)
1592 [aerosol in the Asian part of Russia in 2004 within the framework of AEROSIBNET program, *Atmospheric*](#)
1593 [and oceanic optics](#), 18, 11, 871–878, 2005.

1594 [Sapucci, L.F., Machado, L.A., Monico, J.F., and Plana-Fattori, A.: Intercomparison of Integrated Water Vapor](#)
1595 [Estimates from Multisensors in the Amazonian Region. *J. Atmos. Oceanic Technol.*, 24, 1880–1894,](#)
1596 <https://doi.org/10.1175/JTECH2090.1>, 2007.

1597 Sassen, K., and Campbell, J. R.: A midlatitude cirrus cloud climatology from the Facility for Atmospheric Remote
1598 Sensing. Part I: Macrophysical and synoptic properties, *J. Atmos. Sci.*, 58, 481–496,
1599 [https://doi.org/10.1175/1520-0469\(2001\)058%3C0481:AMCCCF%3E2.0.CO;2](https://doi.org/10.1175/1520-0469(2001)058%3C0481:AMCCCF%3E2.0.CO;2), 2001.

1600 Sayer, A. M., Hsu, N. C., Bettenhausen, C., and Jeong, M.-J.: Validation and uncertainty estimates for MODIS
1601 Collection 6 “Deep Blue” aerosol data, *J. Geophys. Res. Atmos.*, 118, 7864–7872,
1602 <https://doi.org/10.1002/jgrd.50600>, 2013.

1603 Schmid, B., Thome, K.J., Demoulin, P., Peter, R., Matzler, C., and Sekler, J.: Comparison of modeled and empirical
1604 approaches for retrieving columnar water vapor from solar transmittance measurements in the 0.94 micron
1605 region, *J. Geophys. Res.*, 101, 9345–9358, <https://doi.org/10.1029/96JD00337>, 1996.

1606 Schmid, B., Michalsky, J. J., Slater, D. W., Barnard, J. C., Halthore, R. N., Liljegren, J. C., Holben, B. N., Eck, T. F.,
1607 Livingston, J. M., Russell, P. B., Ingold, T., and Slutsker, I.: Comparison of Columnar Water-Vapor
1608 Measurements from Solar Transmittance Methods, *Appl. Opt.* 40, 1886–1896,
1609 <https://doi.org/10.1364/AO.40.001886>, 2001.

1610 Shaw, G. E., Reagan, J. A., and Herman, B. M.: Investigations of atmospheric extinction using solar radiation
1611 measurements made with multiple wavelength radiometer, *J. Appl. Meteorol.*, 12, 374–380,
1612 [https://doi.org/10.1175/1520-0450\(1973\)012%3C0374:IOAEUD%3E2.0.CO;2](https://doi.org/10.1175/1520-0450(1973)012%3C0374:IOAEUD%3E2.0.CO;2), 1973.

1613 Shaw, G.E., Sun Photometry, *Bull. Am. Meteor. Soc.*, 64, 4-10, [https://doi.org/10.1175/1520-0477\(1983\)064%3C0004:SP%3E2.0.CO;2](https://doi.org/10.1175/1520-0477(1983)064%3C0004:SP%3E2.0.CO;2), 1983.

1615 Sinyuk, A., Holben, B. N., Smirnov, A., Eck, T. F., Slutsker, I., Schafer, J. S., Giles, D. M., and Sorokin, M.:
1616 Assessment of error in aerosol optical depth measured by AERONET due to aerosol forward scattering,
1617 *Geophys. Res. Lett.*, 39, L23806, <https://doi.org/10.1029/2012GL053894>, 2012.

1618 Smirnov, A., Holben, B. N., Eck, T. F., Dubovik, O., and Slutsker, I.: Cloud screening and quality control
1619 algorithms for the AERONET database, *Rem. Sens. Env.*, 73, 337-349, [https://doi.org/10.1016/S0034-4257\(00\)00109-7](https://doi.org/10.1016/S0034-4257(00)00109-7), 2000.

1621 Smirnov, A, Holben, B.N., Lyapustin A., Slutsker, I. and Eck, T.F.: AERONET processing algorithms refinement,
1622 AERONET 2004 Workshop, El Arenosillo, Spain, May 10–14, 2004.

Formatted: Default Paragraph Font, Font: Times New Roman

1623 Smirnov, A., Holben, B. N., Slutsker, I., Giles, D. M., McClain, C. R., et al.: Maritime Aerosol Network as a
1624 component of Aerosol Robotic Network, *J. Geophys. Res.*, 114, D06204,
1625 <https://doi.org/10.1029/2008JD011257>, 2009.

1626 Takamura, T, T. Nakajima and SKYNET community group: Overview of SKYNET and its Activities, Proceedings
1627 of AERONET workshop, El Arenosillo., *Optica Pura y Aplicada*, 37, 3303–3308, 2004.

1628 [Toledano, C., Cachorro, V. E., Berjon, A., de Frutos, A. M., Fuertes, D., Gonzalez, R., Torres, B., Rodrigo, R.,](#)
1629 [Bennouna, Y., Martin, L., and Guirado, C.: RIMA-AERONET network: long-term monitoring of aerosol](#)
1630 [properties. *Opt. Pura Apl.*, 44, 629–633, 2011.](#)

1631 [Toledano, C., González, R., Fuertes, D., Cuevas, E., Eck, T. F., Kazadzis, S., Kouremeti, N., Gröbner, J., Goloub,](#)
1632 [P., Blarel, L., Román, R., Barreto, Á., Holben, B. N., and Cachorro, V. E.: Assessment of Sun photometer](#)
1633 [Langley calibration at the high-elevation sites Mauna Loa and Izaña, *Atmos. Chem. Phys. Discuss.*,](#)
1634 <https://doi.org/10.5194/acp-2018-430>, in review, 2018.

1635 Tzortziou, M., Herman, J. R., Cede, A., and Abuhassan, N.: High precision, absolute total column ozone
1636 measurements from the Pandora spectrometer system: Comparisons with data from a Brewer double
1637 monochromator and Aura OMI, *J. Geophys. Res.*, 117, D16303, <https://doi.org/10.1029/2012JD017814>,
1638 2012.

1639 USNO: Approximate Solar Coordinates derived from The Astronomical Almanac, pg. C5:
1640 <http://aa.usno.navy.mil/faq/docs/SunApprox.php>.

1641 [Van Malderen, R., Brenot, H., Pottiaux, E., Beirle, S., Hermans, C., De Mazière, M., Wagner, T., De Backer, H.,](#)
1642 [and Bruyninx, C.: A multi-site intercomparison of integrated water vapour observations for climate change](#)
1643 [analysis. *Atmos. Meas. Tech.*, 7, 2487-2512, <https://doi.org/10.5194/amt-7-2487-2014>, 2014.](#)

1644 Wang S.-H., Tsay, S.-C., Lin, N.-H., Chang, S.-C., C. L., Welton, E. J., Holben, B. N., Hsu, N. C., Lau, W. K. M.,
1645 Lolli, S., Kuo, C.-C., Chia, H.-P., Chiu, C.-Y., Lin, C.-C., Bell, S. W., Ji, Q., Hansell, R. A., Sheu, G.-R.,
1646 Chi, K.-H., and Peng, C.-M.: Origin, transport, and vertical distribution of atmospheric pollutants over the
1647 northern South China Sea during the 7-SEAS/Dongsha Experiment, *Atmospheric Environment*, 78 , 124–
1648 133, <https://doi.org/10.1016/j.atmosenv.2012.11.013>, 2013.

1649 Welton, E. J., Voss, K. J., Gordon, H. R., Maring, H., Smirnov, A., Holben, B., Schmid, B., Livingston, J. M.,
1650 Russell, P. B., Durkee, P. A., Formenti, P., and Andreae, M. O.: Ground-based Lidar Measurements of
1651 Aerosols During ACE-2: Instrument Description, Results, and Comparisons with other Ground-based and
1652 Airborne Measurements, *Tellus B*, 52, 635–650, <https://doi.org/10.1034/j.1600-0889.2000.00025.x>, 2000.

1653 Welton, E.J., and Campbell, J.R.: Micro-pulse Lidar Signals: Uncertainty Analysis, *J. Atmos. Oceanic Technol.*, 19,
1654 2089–2094, [https://doi.org/10.1175/1520-0426\(2002\)019%3C2089:MLSUA%3E2.0.CO;2](https://doi.org/10.1175/1520-0426(2002)019%3C2089:MLSUA%3E2.0.CO;2), 2002.

1655 Zibordi, G., Holben, B., Melin, F., D'Alimonte, D., Berthon, J.-F., Slutsker, I., and Giles, D.: AERONET-OC: an
1656 overview, *Can. J. Remote Sens.*, 36, 5, <https://doi.org/10.5589/m10-073>, 2010.

1657

Commented [GDM(SAAI1): Verify all pending publications are updated if necessary

Formatted: Default Paragraph Font

1658 **Table 1.** Nominal AERONET wavelengths for ion assisted deposition filters used for aerosol remote sensing and spectral
 1659 corrections or components for each channel.

Nominal Central Wavelengths (nm)	Filter Bandpass (nm)	Spectral Corrections/ Components
340	2	Rayleigh, NO ₂ , O ₃
380	2	Rayleigh, NO ₂
440	10	Rayleigh, NO ₂
500	10	Rayleigh, NO ₂ , O ₃
675	10	Rayleigh, O ₃
870	10	Rayleigh
935	10	Rayleigh, Aerosol
1020	10	Rayleigh, H ₂ O
1640	25	Rayleigh, H ₂ O, CO ₂ , CH ₄

1660

1661

1662 **Table 2.** Summary of Cloud Screening Related Quality Control Changes from Version 2 to Version 3.

Algorithm/Parameter	Version 2	Version 3
Very High AOD Restoration	N/A	$\tau_{870} > 0.5$; $\alpha_{675-1020} > 1.2$ or $\alpha_{870-1020} > 1.3$, restore if eliminated by cloud screening
Optical Air Mass Range	Maximum of 5.0	Maximum of 7.0
Number of Potential Measurements	$N_{\text{remain}} < 3$, reject all measurements in the day	After all checks applied, reject all measurements in the day if $N_{\text{remain}} < \text{MAX}\{3 \text{ or } 10\% \text{ of } N\}$
Triplet Criterion	All wavelengths checked; AOD Triplet Variability $> \text{MAX}\{0.02 \text{ or } 0.03 * \tau_{\text{aerosol}}\}$	Check only wavelengths 675, 870, and 1020nm; AOD Triplet Variability $> \text{MAX}\{0.01 \text{ or } 0.015 * \tau_{\text{aerosol}}\}$ for 675nm, 870nm, and 1020nm wavelengths simultaneously
Ångstrom Exponent (AE) Limitation	N/A	If $\text{AE}_{440-870\text{nm}} < -1.0$ or $\text{AE}_{440-870\text{nm}} > 3.0$, then eliminate triplet measurement.
Smoothness Check	$D < 16$	For AOD _{500nm} (or 440nm) $\Delta\tau_{\text{aerosol}} > 0.01$ per minute, then remove larger τ_{aerosol} in pair. Repeat condition for each pair until points are not removed.
Solar Aureole radiance Curvature Check (Sect. 3.2.2)	N/A	Using 1020nm solar aureole radiances, compute the curvature (k) between 3.2° and 6.0° scattering angle (φ) at the smallest scattering angle. If $k < 2.0E-5 \varphi$ and if slope of curvature (M) is greater than 4.3 (empirically determined), then radiances are cloud contaminated. For sky scan measurements, all τ_{aerosol} measurements are removed within 30 minutes of the sky measurement. For Model T, special aureole scan measurements will remove all τ_{aerosol} within a two minute period superseding any sky scan aureole measurements.
Standalone Measurements	N/A	If no data exists within 1 hour of a measurement, then reject it unless $\text{AE}_{440-870\text{nm}} > 1.0$.
AOD Stability Check	Same as Version 3	Daily averaged AOD 500nm (or 440nm) has σ less than 0.015, then do not perform 3- σ check.
3- σ Check	Same as Version 3	AOD 500nm and $\text{AE}_{440-870\text{nm}}$ should be within the $\text{MEAN} \pm 3\sigma$; otherwise, the points are rejected.

1663

1664

1665 **Table 3.** AERONET and MPLNET sites and date ranges used for assessing cirrus and non-cirrus cloud presence

Site	Latitude	Longitude	Elevation (meters)	Date Range
GSFC	38.9925° N	76.8398° W	87	May 2001–Jan 2013
COVE	36.9000° N	75.7100° W	37	May 2004–Jan 2008
Kanpur	26.5128° N	80.2316° E	123	May 2009–Jan 2013
SEDE_BOKER	30.8550° N	34.7822° E	480	Nov 2007–Apr 2013
Santa_Cruz_Tenerife	28.4725° N	16.2473° W	52	Nov 2005–Jan 2013
Singapore	1.2977° N	103.7804° E	30	Aug 2009–Jan 2013
Ragged_Point	13.1650° N	59.4320° W	40	Jun 2008–Jan 2013
Trinidad_Head	41.0539° N	124.1510° W	105	May 2005–Feb 2013

1666

1667

1668 **Table 4.** Thresholds used to determine the independent and dependent AOD diurnal dependence. Satisfying both the slope and
 1669 correlation coefficient (*R*) conditions would constitute the possible removal of all measurements for a day.

Day Removal Type	AOD Diurnal Shape	Analyzed Period	Slope Threshold	R Threshold
Independent	Concave	AM, PM, Day	>0.25	>0.974
Dependent	Concave	AM, PM	>0.04	>0.94
Dependent	Concave	Day	>0.1	>0.94
Dependent	Convex	AM, PM, Day	<-0.02	<-0.94
Dependent – $\tau_{avg} < 0.1$	Convex	AM, PM, Day	<-0.1	<-0.94
Independent – 2 or more Silicon wavelengths (440, 675, 870, 1020nm) or 1640nm InGaAs	Concave	AM, PM, Day	>0.1 Day or AM & PM > 0.02	>0.94

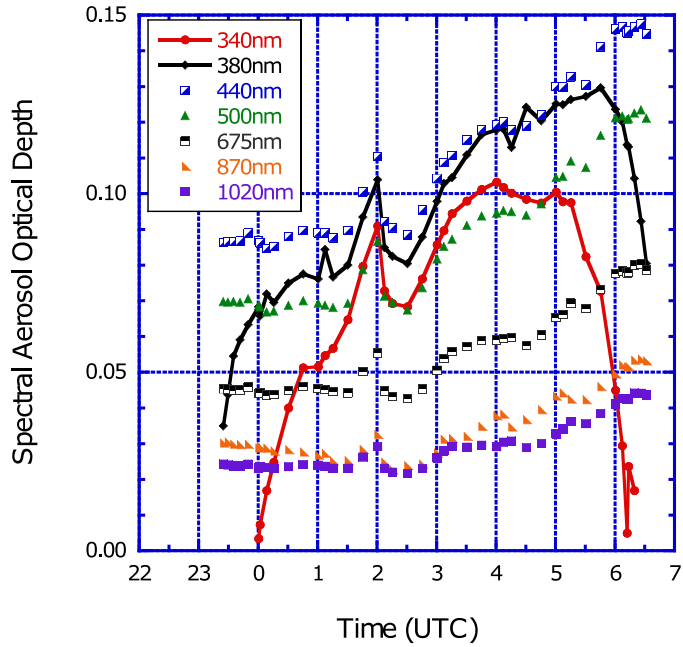
1670

1671

1672 **Table 5.** Statistics corresponding to Fig. 21 and Fig. 22 for AOD interpolated to 500nm, Ångstrom exponent 440–870nm,
 1673 precipitable water (cm), and the number of days. Version 3 Level 2.0 and Version 2 Level 2.0 data are compared for the same
 1674 multi-year monthly averages when sites have a total of more than 1000 days for all months and more than 30 days in each month.
 1675 Data represented as “Matched” indicates the further condition that the exact observations were matched in Version 2 and Version
 1676 3 Level 2.0 multi-year monthly average data sets. Note that PW values for the “Matched” data set are approximately the same as
 1677 the unmatched data set.

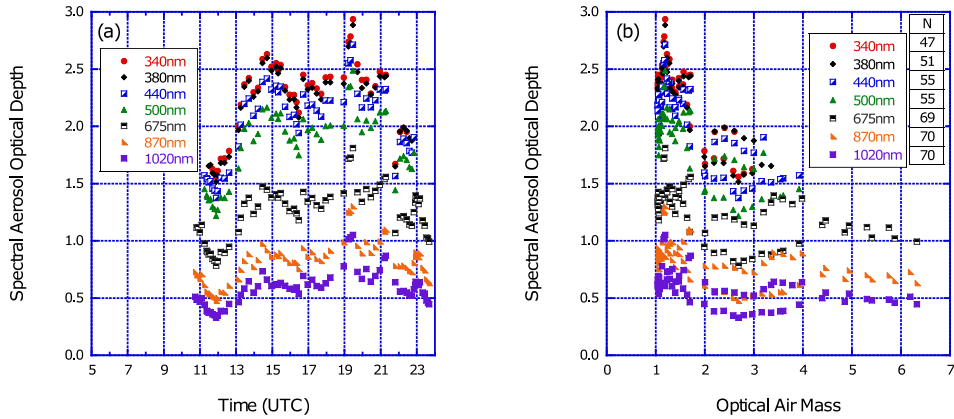
Parameter	AOD _{500nm}	AE _{440-870nm}	PW (cm)	Days	AOD _{500nm}	AE _{440-870nm}
	(V3–V2)	(V3–V2)	(V3–V2)	(V3–V2)	(V3–V2)	(V3–V2)
	Unmatched	Unmatched	Unmatched	Unmatched	Matched	Matched
Average	0.002	–0.01	–0.02	–0.4	–0.002	–0.03
Standard Deviation	0.022	0.10	0.06	24.8	0.004	0.10
Maximum	0.247	0.29	0.34	150	0.015	0.35
Minimum	–0.166	–1.54	–0.45	–130	–0.029	–1.63
Number of Months	2953	2953	2953	2953	2514	2514

1678
 1679



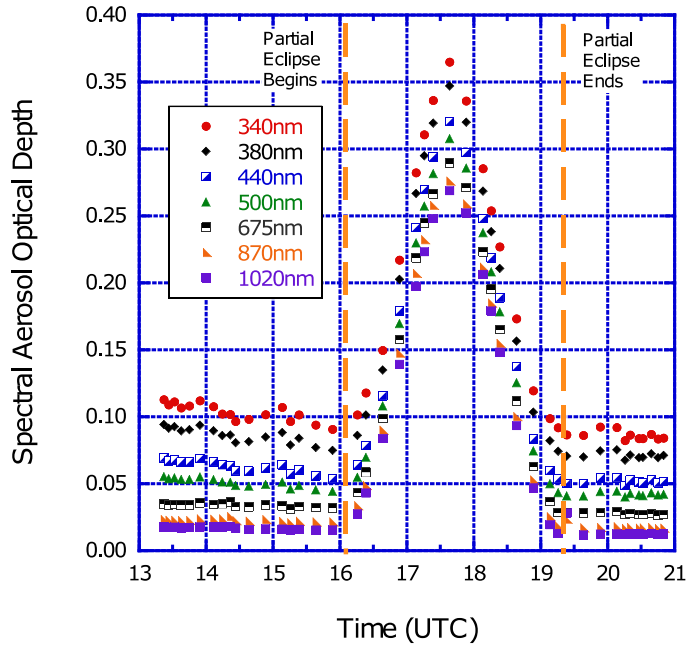
1680
 1681 **Figure 1.** Aerosol optical depth (AOD) data from AERONET Ussuriysk site (43.70° N, 132.16° E) on 30 November 2005 shows
 1682 electronic instability. For the Cimel Model 4 instruments, the electronic sensitivity of the UV AOD data (340nm and 380nm) can
 1683 be high due to a bad amplifier. The resulting AOD data for the UV channels are out of spectral dependence the entire day with
 1684 a maximum error for large optical air mass due to large dark current values. The UV channels (identified by line plots) are
 1685 removed by the quality control while preserving other wavelengths that are not affected by this condition.

1686



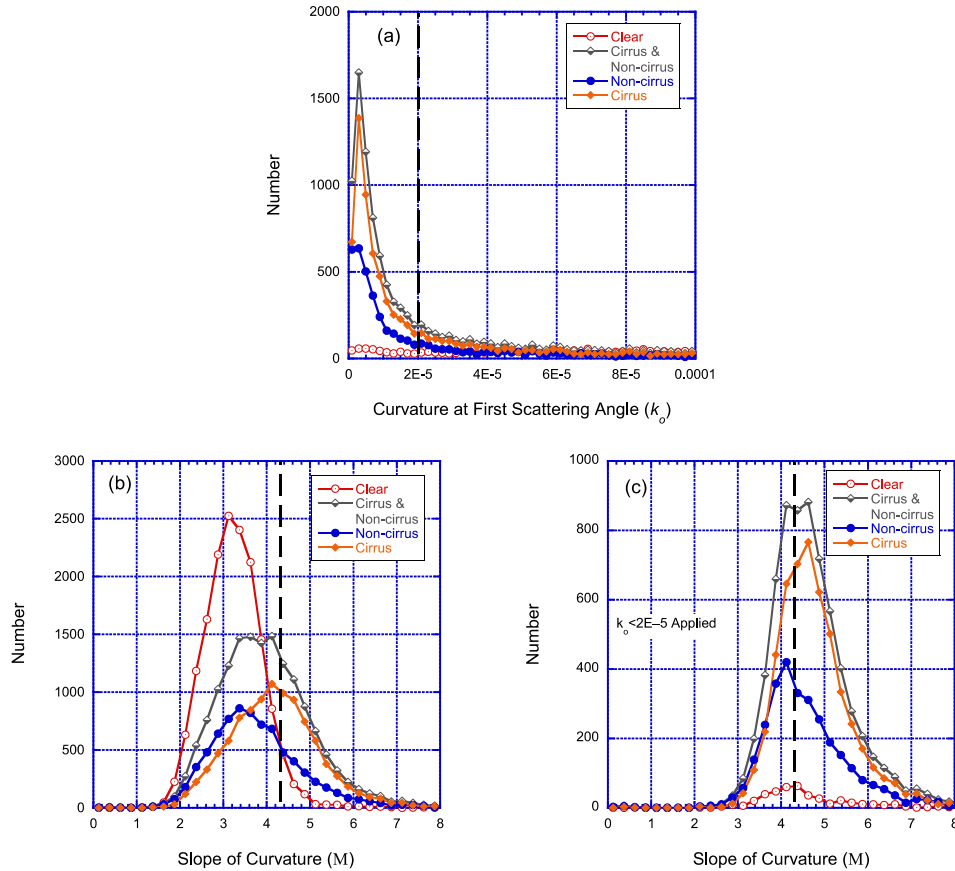
1687
 1688 **Figure 2.** Spectral dependent low digital number removal at NASA Goddard Space Flight Center (GSFC; 38.99°N, 76.84°W).
 1689 (a) Level 1.0 AOD data from GSFC on 8 July 2002 are plotted for the Quebec forest fire smoke event. Significantly fewer Level
 1690 1.0 AOD data are available for the shorter wavelengths near local sunrise (~11 UTC) and sunset (~23:30 UTC). (b) The
 1691 distribution of the AOD measurements with respect to optical air mass clearly shows the removal of short wavelengths for large
 1692 air mass in this fine mode aerosol event. The high aerosol loading due to smoke and haze results in significant extinction at UV
 1693 and visible wavelengths, which corresponds to low digital counts. The low digital count quality control removes AOD
 1694 measurements impacted by diffuse radiation scattered into the instrument field of view (Sinyuk et al., 2012).

1695



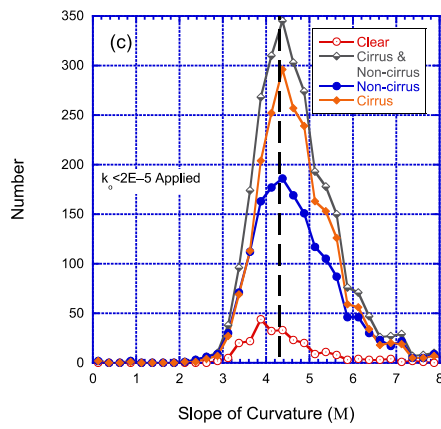
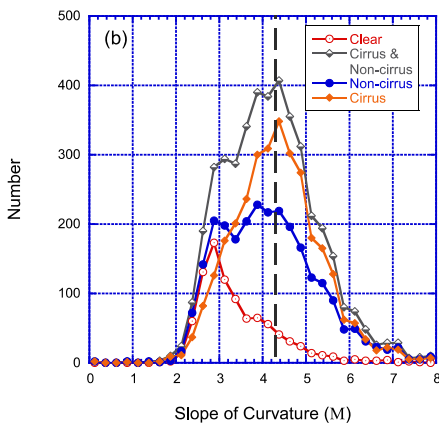
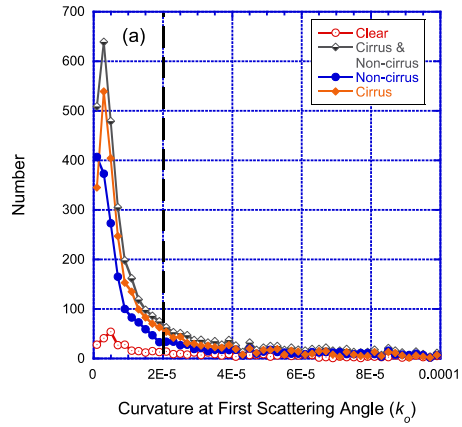
1696
 1697 **Figure 3.** Eclipse circumstance at the NASA Goddard Space Flight Center (GSFC; 38.99° N, 76.84° W) on 25 December 2000
 1698 between 16:04:13 UTC and 19:16:25 UTC. The maximum AOD during the eclipse occurs at the maximum obscuration of 0.42,
 1699 which results in a change of ~ 0.28 for AOD 500nm compared to data before and after the solar eclipse. Utilizing the NASA
 1700 Solar Eclipse database, the AOD measurements are removed between the partial eclipse first contact and partial eclipse last
 1701 contact as denoted by the vertical dashed lines.

1702
 1703

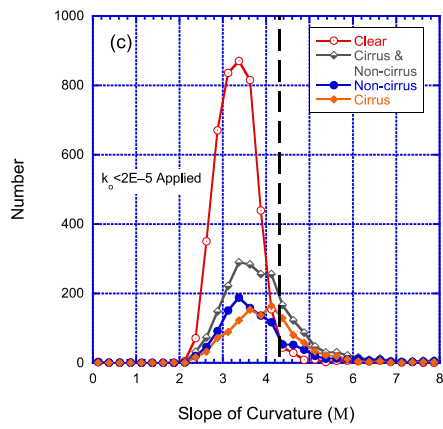
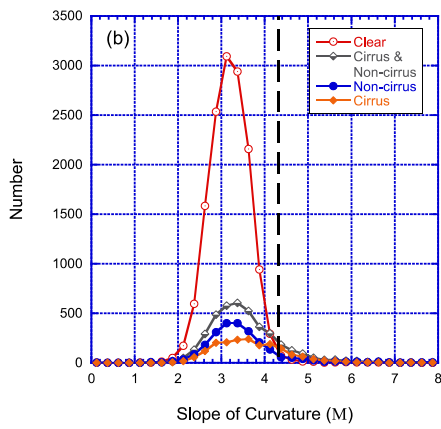
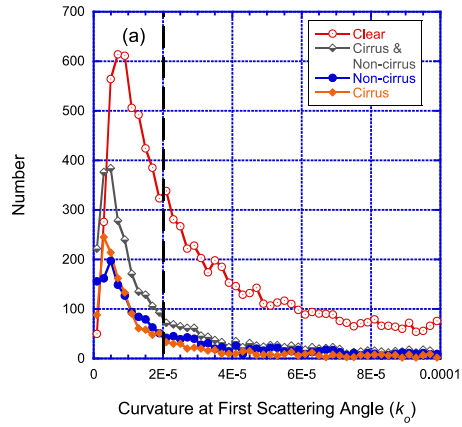


1704
 1705 **Figure 4.** NASA Goddard Space Flight Center (GSFC; 38.99° N, 76.84° W) AERONET data coincident with MPLNET LIDAR
 1706 derived sky condition categories (Clear, both Cirrus and Non-cirrus clouds, Non-cirrus clouds, and Cirrus clouds) from 2001–
 1707 2013. The AERONET solar aureole 1020nm radiances are used to calculate the curvature at the first scattering angle (k_0) and the
 1708 slope of curvature (M) between 3.2° and 6.0° scattering angles. (a) The number distribution of k_0 is shown and the dashed
 1709 vertical line at k_0 equals $2E-5$ indicates the threshold where values less than $2E-5$ are considered possibly cirrus cloud
 1710 contaminated (the x-axis is truncated at $1E-4$ for viewing purposes). (b) The number distribution of M is shown and M greater
 1711 than 4.3 are considered to be possibly cirrus cloud contaminated (the dashed vertical line indicates the threshold of 4.3).
 1712 Similar to panel (b) except that the k_0 threshold ($k_0 < 2E-5$) is applied first and, as a result, data greater than 4.3 in this panel are
 1713 considered to be cirrus cloud contaminated.

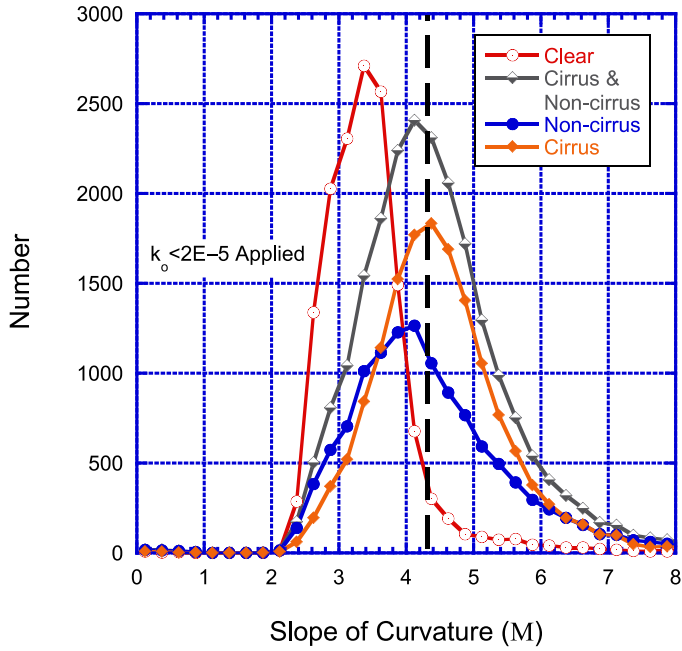
1714



1715
 1716 **Figure 5.** Similar to Fig. 4, except for Singapore (1.29° N, 103.78° E) from 2009–2013.
 1717



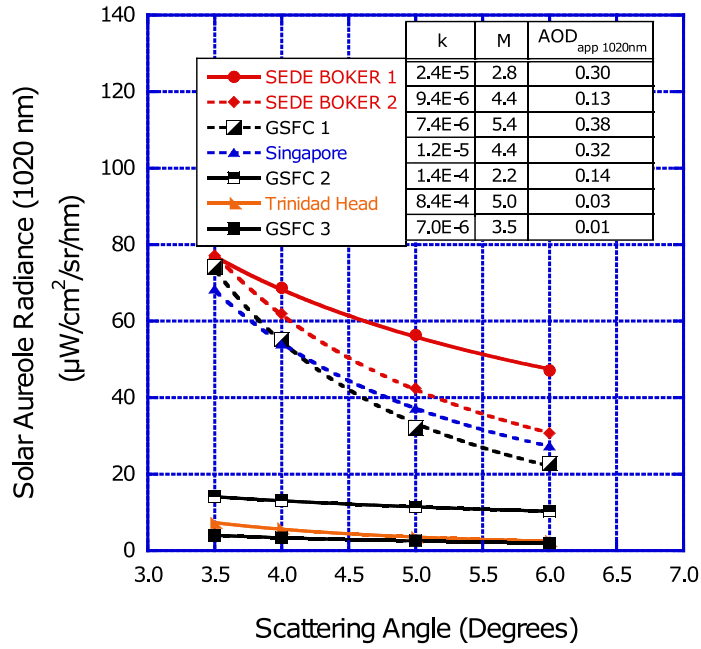
1718
 1719 **Figure 6.** Similar to Fig. 4, except for SEDE BOKER (30.85° N, 34.78° E) from 2007–2013.
 1720



1721
1722
1723

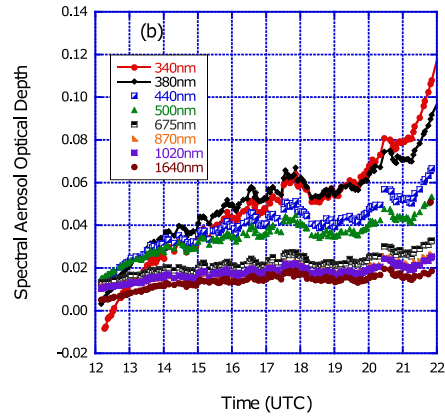
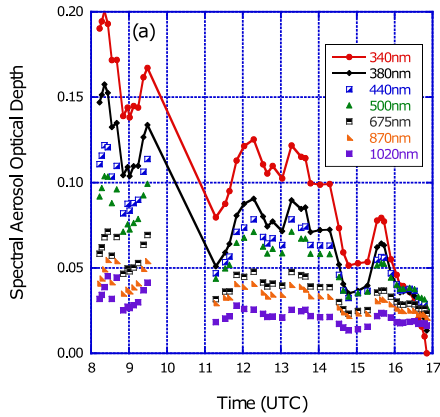
Figure 7. Similar to Fig. 4c including all analyzed sites in [Table 3](#) [Table 3](#).

Formatted: Font: Not Bold



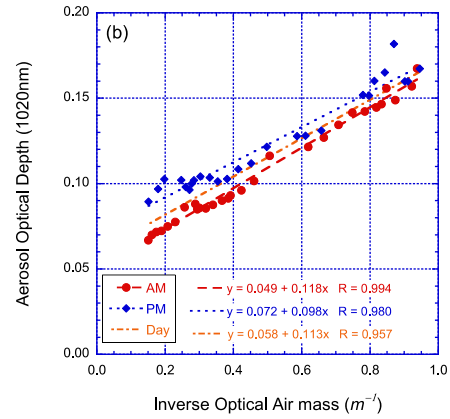
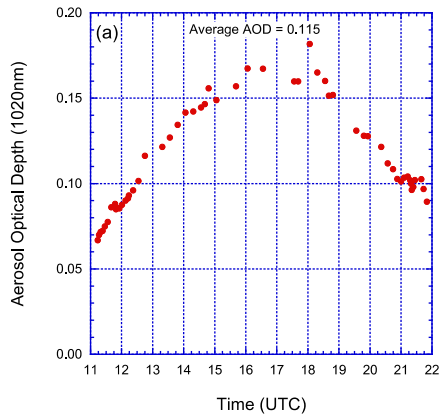
1724
 1725 **Figure 8.** The solar aureole 1020nm radiance versus the scattering angle in degrees for selected sites. Data plots with the dashed
 1726 lines (i.e., SEDE BOKER 2, GSFC 1, and Singapore) all qualify for the removal of data due to optically thin homogeneous cloud
 1727 contamination.

1728



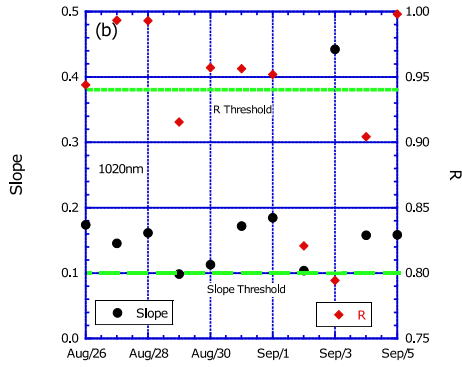
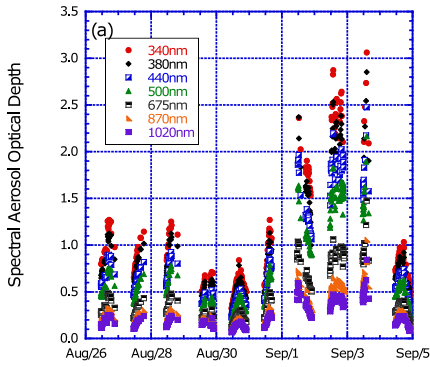
1729
 1730 **Figure 9.** Time shifted aerosol optical depth (AOD) data examples at Malaga (36.72° N, 4.48° W) and Toronto (43.79° N,
 1731 79.47° W). Note the line plot is used to emphasize the 340nm and 380nm AOD impact for the time shift. **(a)** The Level 1.5
 1732 AOD cloud screened only data measured at the Malaga site on 30 January 2014. These data show the time shifted AOD
 1733 especially at short wavelengths represent the instrument clock is too fast. **(b)** The Level 1.5 AOD cloud screened only data
 1734 measured at the Toronto site on 24 September 2013. The time shifted aerosol optical depth especially at short wavelengths
 1735 represent when the instrument clock was too slow. Panel (a) also shows the algorithm can be used with data gaps and lower
 1736 temporal resolution measurement interval compared to panel (b).

1737



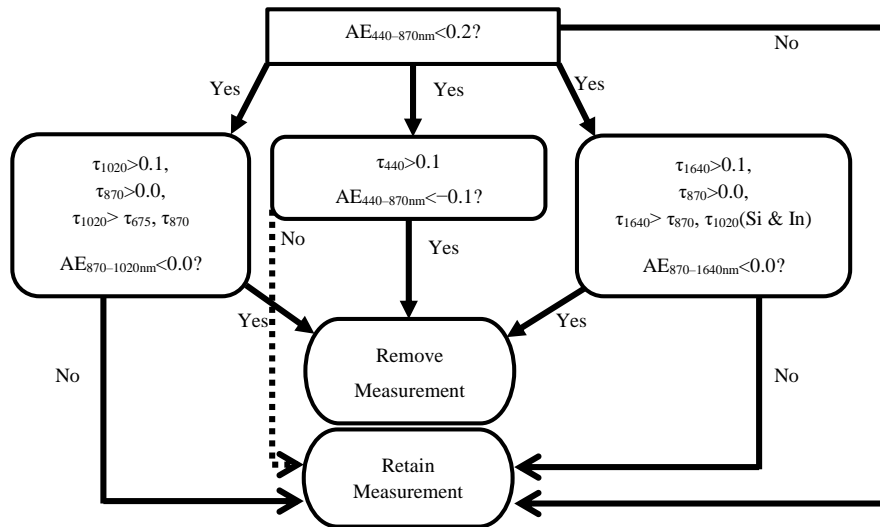
1738
 1739 **Figure 10.** AERONET data collected at Rio Branco (9.96 °S, 67.87° W) on 30 August 2011. The AOD 1020nm Level 1.5 with
 1740 only the cloud screening algorithm applied to the data. (a) The AOD diurnal dependence presents a concave shape during
 1741 the solar day. (b) The AOD 1020nm and the inverse optical air mass show a highly correlated linear fit and the slope is significant
 1742 for the full day (day) and morning (AM), and afternoon (PM). Data separation for AM and PM is defined by the local solar
 1743 noon, which is 16:31:28 UTC at Rio Branco.

1744



1745
 1746 **Figure 11.** AERONET data collected at Rio Branco (9.96° S, 67.87° W) from 15 August to 30 September 2011. (a) The time
 1747 series of Level 1.5 spectral AOD (cloud screened only) data is plotted from 26 August to 5 September 2011 and shows repeated
 1748 diurnal dependence for varying magnitudes of AOD. (b) The robust linear fit slope and correlation coefficient (R) is calculated
 1749 from the AOD 1020nm versus the inverse of the optical air mass (m^{-1}). For the full day evaluation, the green dashed line
 1750 indicates the threshold for the slope parameter at 0.1 and the solid green line indicates the threshold for the correlation coefficient
 1751 ($R = 0.94$). Both the slope and R must exceed these thresholds for at least three days scanning from the current day to the last
 1752 occurrence within the 20-day period to remove the spectral AOD, and in this circumstance, all of the data are removed for the
 1753 period for Levels 1.5 and 2.0.

1754



1755
 1756 **Figure 12.** Flowchart of the reverse spectral dependence algorithm used to remove cloud contamination artifacts and instrument
 1757 anomalies. The 1640nm wavelength is available on some Cimel Model 5 instruments and all Model T instruments.
 1758

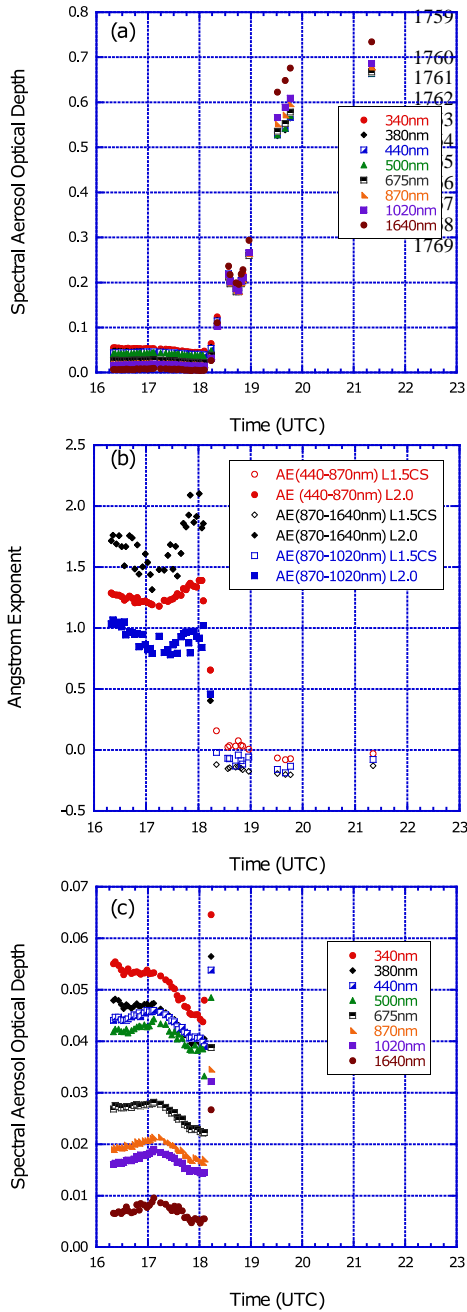
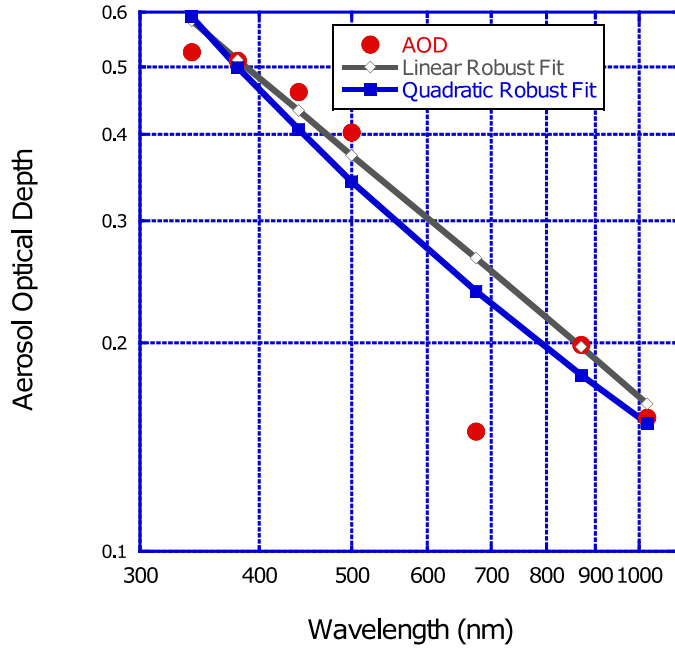


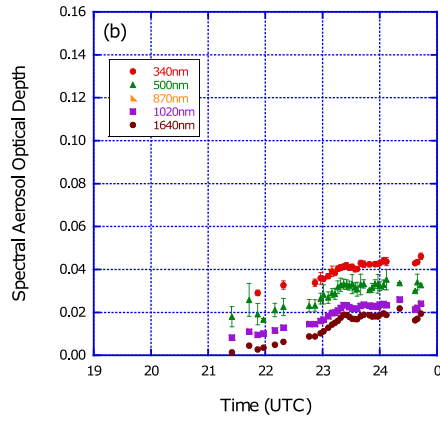
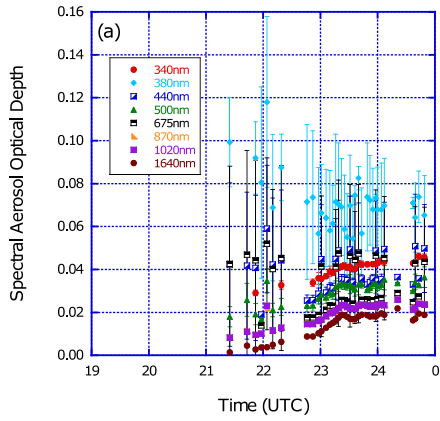
Figure 13. Data from Bratts Lake (50.20° N, 104.71° W) on 7 January 2007. **(a)** The Level 1.5 data with only the cloud screening (CS) algorithm applied shows cloud contaminated data remain after 18:10 UTC. **(b)** For the same period as (a), the Ångström exponent values decreased significantly to a level where coarse mode aerosol particles are not expected. **(c)** The final Level 1.5 and Level 2.0 data series after the reverse spectral dependence quality control or additional cloud screening method has been applied to the standalone Level 1.5 CS data.

1770



1771 **Figure 14.** AERONET data from the Osaka (34.65° N, 135.59° E) site on 16 October 2006 at 22:02:11 UTC. The plot shows
1772 AOD versus the wavelength with lines identifying the linear and quadratic robust regression fits on logarithmic scale used by the
1773 AOD spectral dependence algorithm. The 675nm channel is clearly anomalous with fits differing by 0.12 for linear and 0.09 for
1774 quadratic. In addition, the AOD 340nm appears anomalous with deviations of 0.06 from linear fit and 0.07 from quadratic fit.
1775 While both wavelengths exceed their respective AOD thresholds (0.023 for 675nm and 0.051 for 340nm), the algorithm
1776 determines the maximum deviation for linear and quadratic fits and removes the AOD 675nm measurement. A subsequent scan
1777 by the algorithm determined that the remaining AOD measurements from 340nm to 1020nm were within the established fit
1778 deviation thresholds.

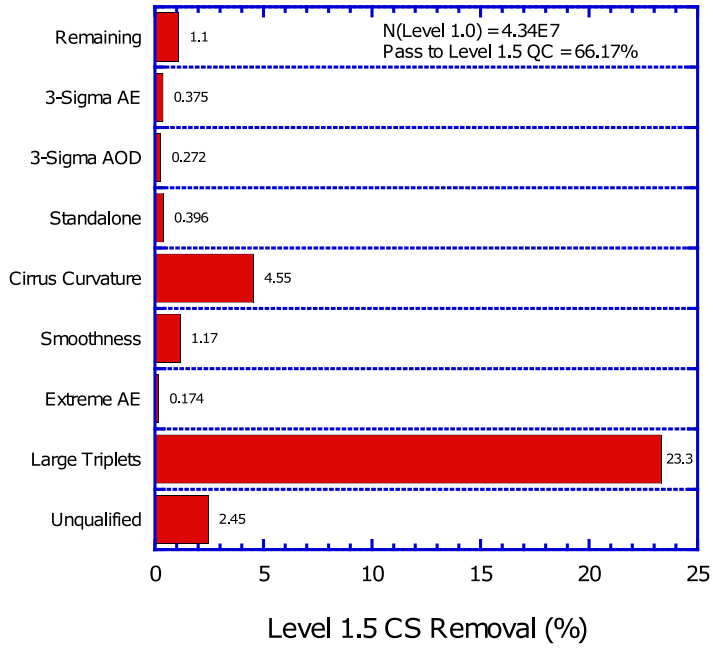
1779



1780
 1781 **Figure 15.** Spectral AOD exhibiting large triplet variability at PEARL (80.05° N, 86.42° W) on 25 August 2013. (a) Version 3
 1782 Level 1.5 cloud screened only data is plotted with large triplet variability and these data were not removed by the cloud
 1783 screening. The error bars represent the triplet variability (AOD Max – AOD Min) divided by 2 so the full range represents the
 1784 AOD triplet variability. The large triplet variability occurs mainly at shorter wavelengths than 675nm. (b) Data affected by large
 1785 triplet variability (i.e., AOD 380nm, AOD 440nm, and AOD 675nm) are removed by using the Level 1.5 large triplet variability
 1786 quality controls.

1787

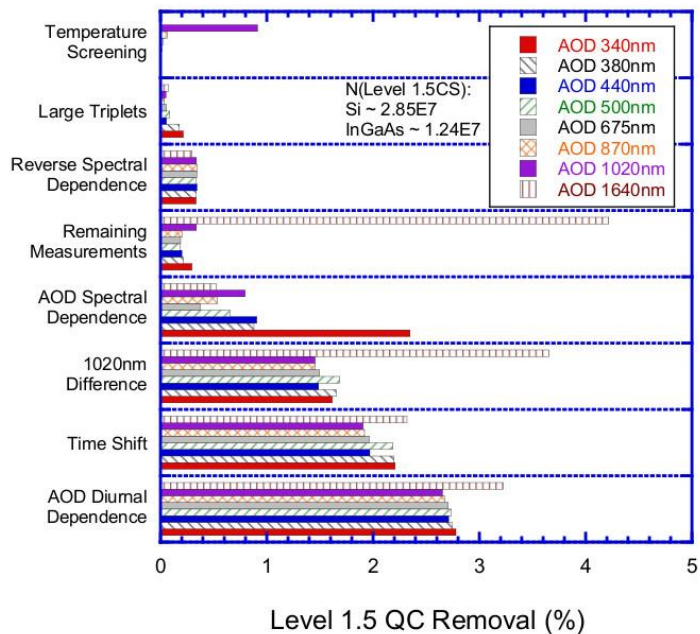
1788



1789

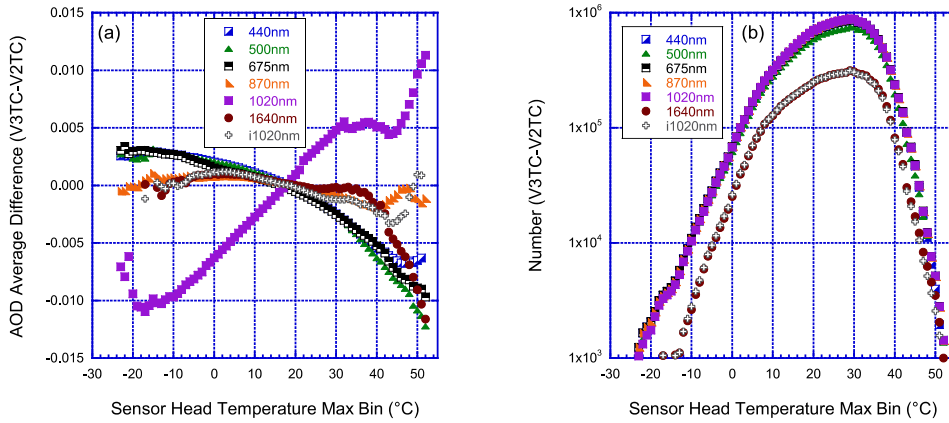
1790 **Figure 16.** The Level 1.0 AOD measurement removal by the Level 1.5 cloud screening algorithm from 1993 to 2018. The plot
1791 shows the impact of the major cloud screening steps in the Level 1.5 cloud screening algorithm and removal of these data applies
1792 to all wavelengths. The triplet criterion removes more than 23% of the Level 1.0 data. Nearly 5% of the Level 1.0 data are
1793 removed due to cirrus cloud contamination. The “Remaining” category indicates the check performed after each cloud screening
1794 step to determine if enough measurements are available and do not meet the high AOD retention criteria. The “Unqualified”
1795 category indicates data that are negative-not triplets or lack sufficient channels to participate in the cloud screening algorithm.

1796



1797
1798 **Figure 17.** Level 1.5 quality control algorithm wavelength dependent impacts for each major step for the period analyzed from
1799 1993–2018. The most significant removal for most channels is due to AOD diurnal dependence, time shift, and difference
1800 between AOD 1020nm on the Silicon and InGaAs detectors (resulting from collimator inconsistency). The AOD 340nm has
1801 significant removal of AOD spectral dependence. The 1640nm InGaAs channel has significant removal by “Remaining
1802 Measurements” since this wavelength cannot be checked for quality when the Silicon channels are not available. Temperature
1803 screening mostly applies to the 1020nm Silicon wavelength due to its strong temperature dependence near the edge of the signal
1804 sensitivity of the Silicon photodiode detector.

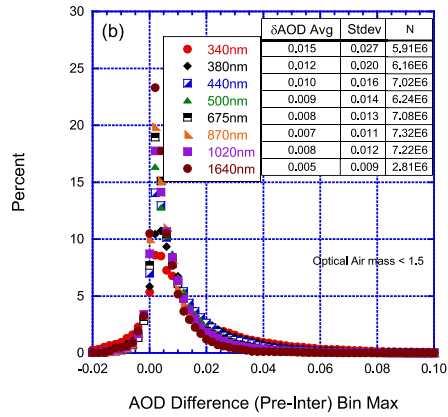
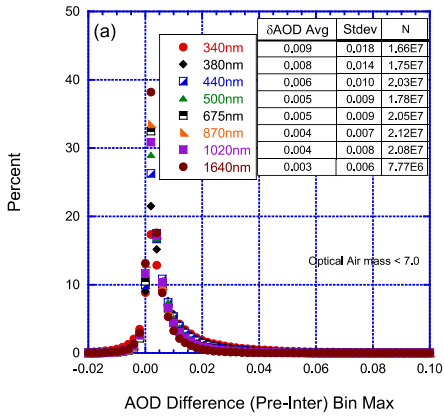
1805



1806

1807 **Figure 18.** Difference in AOD response between Version 3 and Version 2 temperature correction applied to Version 3 AOD data
 1808 based on the sensor head temperature from 1993–2018. The Version 2 temperature correction assumes temperature ranges for
 1809 1020nm and no temperature correction for all other wavelengths, while Version 3 temperature correction characterizes the
 1810 temperature response for each filter or set of default filters for each instrument for wavelengths $\geq 400\text{nm}$. (a) The AOD average
 1811 difference plotted for each 1°C temperature bin from -25°C to $+55^\circ\text{C}$. The AOD 1020nm exhibits an opposite trend compared to
 1812 the other wavelengths varying from -0.01 at low temperatures and up to $+0.01$ at high temperatures. Other wavelengths have
 1813 slight differences at cold temperatures but apparent dependencies at high temperatures greater than 40°C possibly due to
 1814 extrapolation of the temperature coefficients to higher temperatures. (b) The number of measurements plotted for each 1°C
 1815 temperature bin with a minimum of 1000 observations.

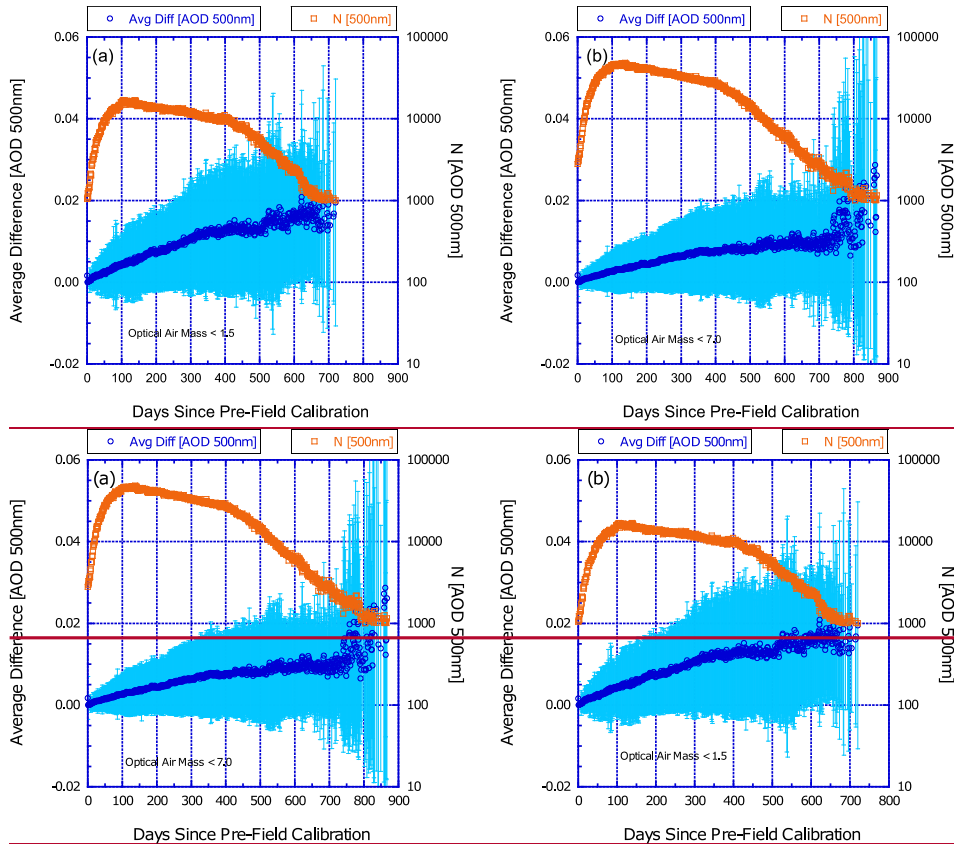
1816



1817

1818 **Figure 19.** Using data qualified as Version 3, Level 2.0, aerosol optical depth (AOD) average difference comparing
 1819 measurements only with the pre-field calibration applied versus instruments with both the pre-field and post-field calibrations
 1820 applied from 1993–2018. Calibration sites are excluded from the analysis. The histogram of AOD differences is provided for the
 1821 optical air mass $1.0 \leq m < 7.0$ range in panel (a) and $1.0 \leq m < 1.5$ range in panel (b). The average difference is largest for the UV
 1822 wavelengths and smallest for the longer wavelengths.

1823

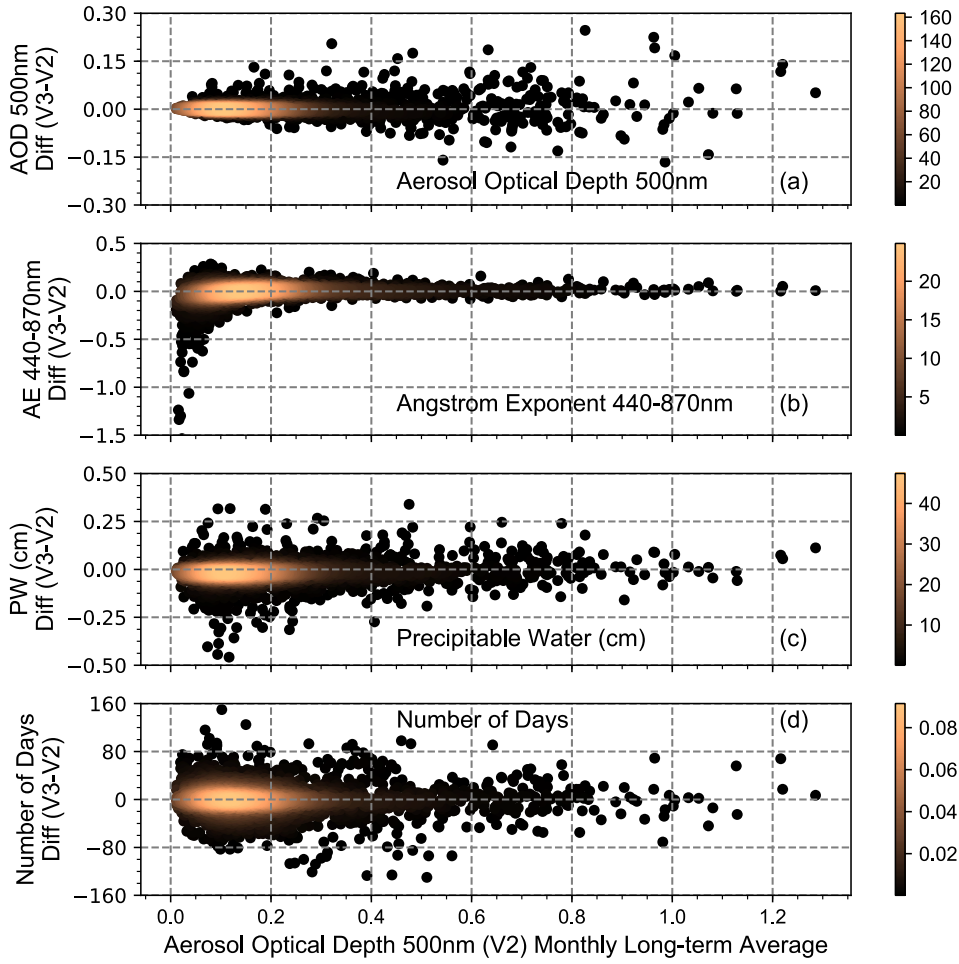


824

825

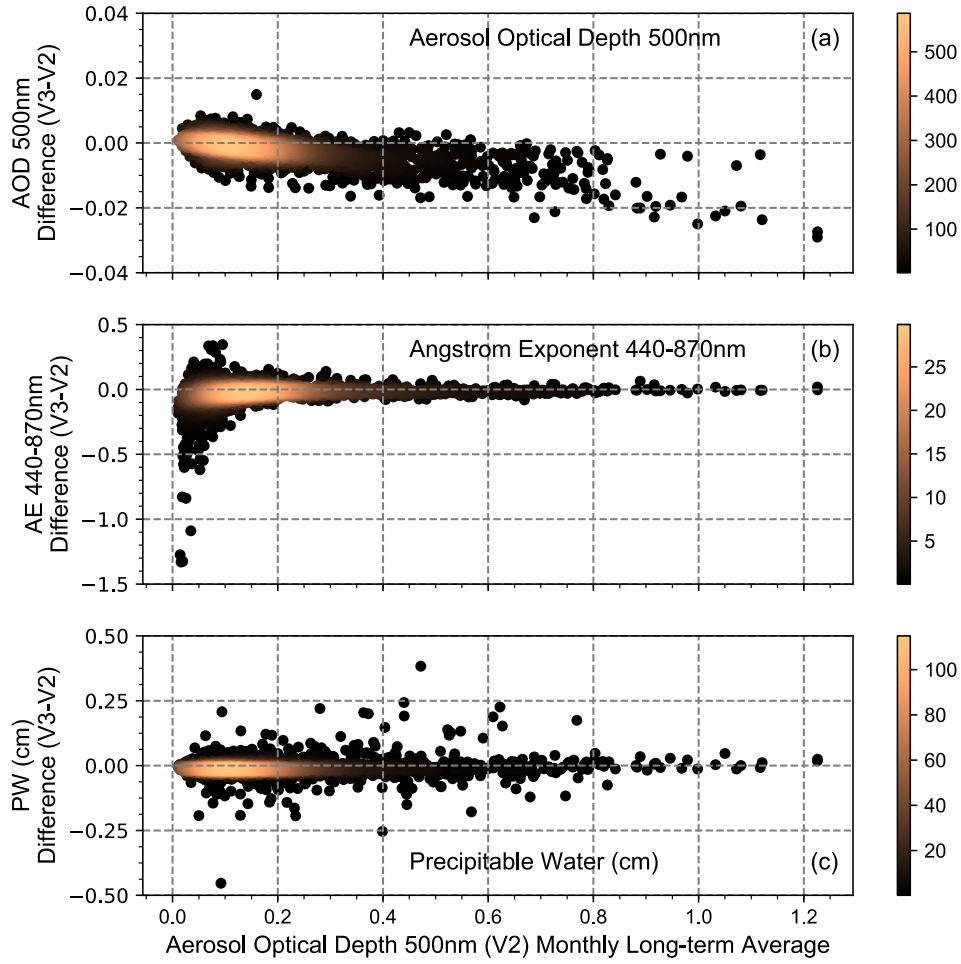
1826 **Figure 20.** Using data qualified as Version 3 Level 2.0 aerosol optical depth (AOD) 500nm average difference comparing
 1827 measurements only with the pre-field calibration applied versus instruments with both the pre-field and post-field calibrations
 1828 applied from 1993–2018. The AOD average differences are provided for the optical air mass $1.0 \leq m < 7.0$ range in panel (a) and
 1829 $1.0 \leq m < 1.5$ range in panel (b). Vertical bars represent the standard deviation for each day bin. The secondary y-axis in
 1830 logarithmic scale represents the number of measurements of AOD 500nm for each day bin.

1831



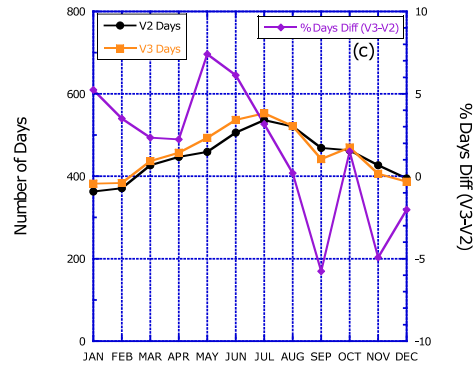
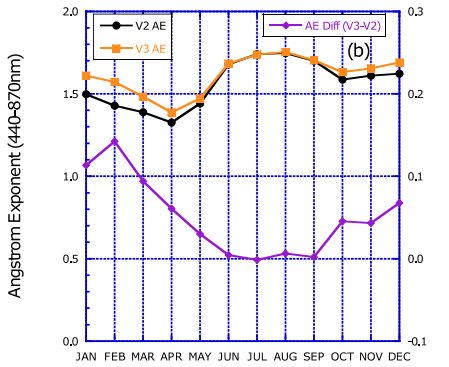
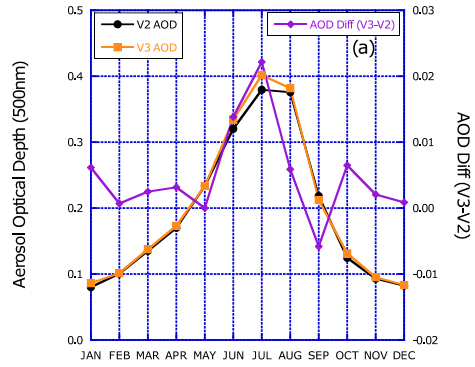
1832
 1833 **Figure 21.** Comparison of Version 3 and Version 2 Level 2.0 multi-year monthly average data sets. (a) The aerosol optical depth
 1834 (AOD) interpolated to 500nm to include data from instruments without 500nm. (b) The Ångström exponent (AE) is calculated
 1835 utilizing the inclusive ordinary least squares regression fit from 440–870nm. (c) The precipitable water in cm is derived from the
 1836 935nm water vapor channel. (d) The difference in the number of days is determined for each monthly long-term average.

1837



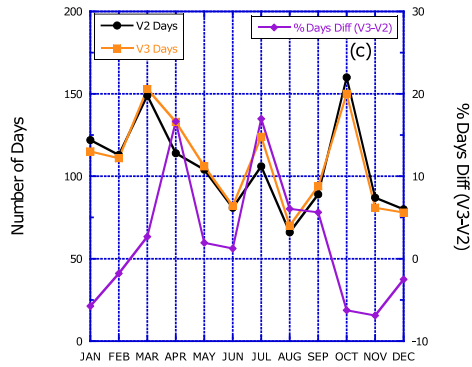
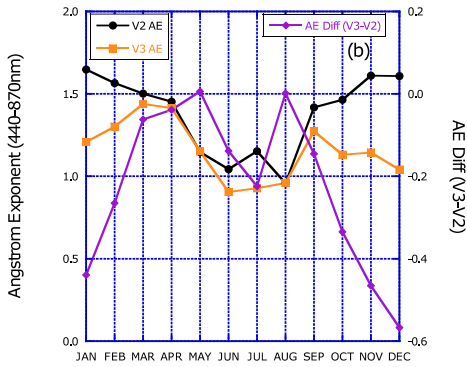
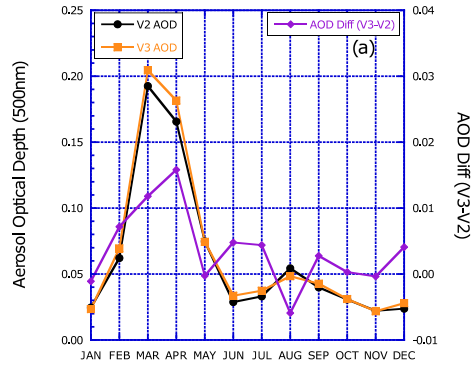
1838
 1839 **Figure 22.** Comparison of Version 3 and Version 2 Level 2.0 multi-year monthly average data sets for time matched
 1840 instantaneous observations in both data sets. The panels are similar to those in Fig. 21.

1841



1842
 1843 **Figure 23.** Long-term multi-year (1993–2016) monthly average comparisons of the Version 3 and Version 2 Level 2.0 data sets
 1844 at the NASA Goddard Space Flight Center (GSFC), Maryland, USA. The panel (a) provides the AOD interpolated to 500nm for
 1845 each version on the primary y-axis and differences on the secondary y-axis. The panels (b) and (c) are plotted similarly for the
 1846 AE_{440-870nm} and the number of days in the multi-year monthly average, respectively.

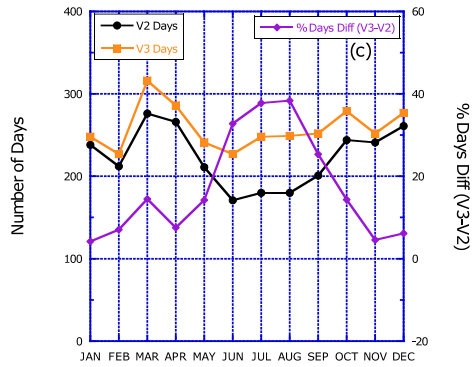
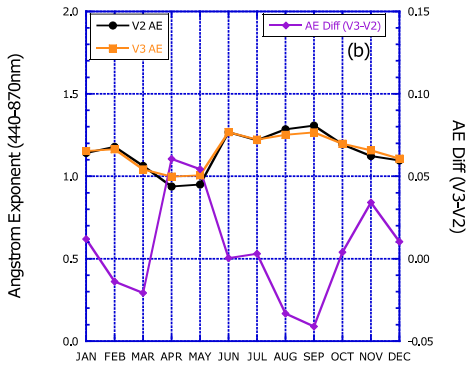
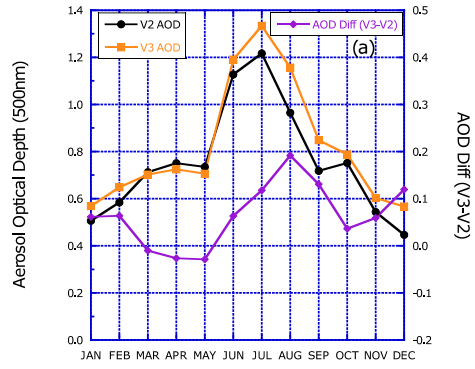
1847



1848

1849 **Figure 24.** Similar to Fig. 23 except for Lulin, Taiwan (23.47° N, 120.87° E) from 2006–2017.

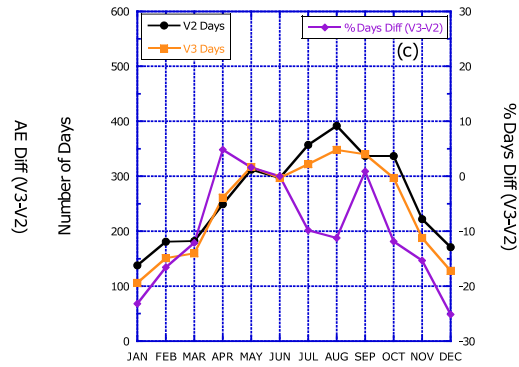
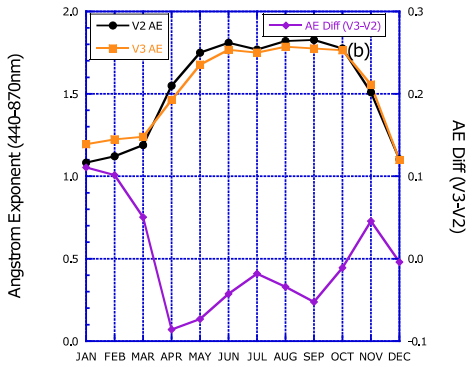
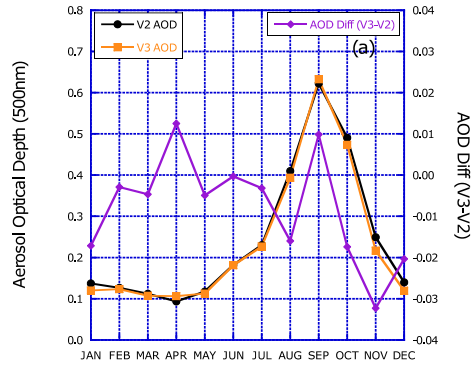
1850



1851

1852 **Figure 25.** Similar to Fig. 23 except for XiangHe, China (39.75° N, 116.96° E) from 2001–2017, except 2009.

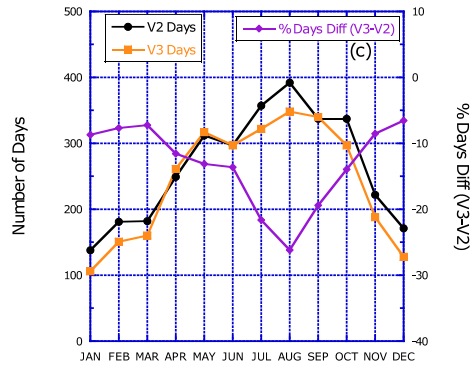
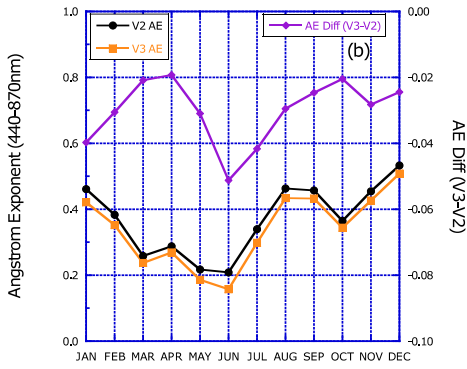
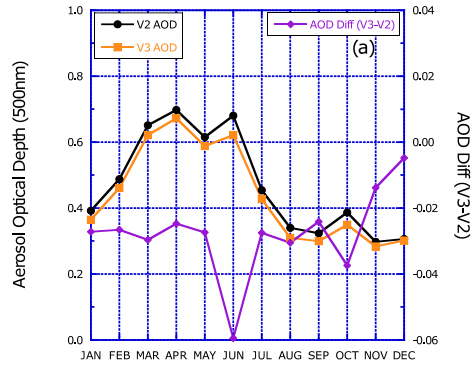
1853



1854

1855 **Figure 26.** Similar to Fig. 23 except for Mongu, Zambia (15.25° S, 23.15° E) from 1997–2010.

1856



1857

1858 **Figure 27.** Similar to Fig. 23, except for IER-Cinzana, Mali (13.28° N, 5.93° W) from 2004-2017.